# Modeling of the Effect of Run-out Table Cooling on the Microstructure of a Thick Walled X70 Skelp

by

Antoine Van Der Laan

A thesis submitted in partial fulfillment of the requirements for the degree of

Master of Science

in

Materials Engineering

Department of Chemical and Materials Engineering

University of Alberta

# Abstract

This thesis presents work performed to model and measure the effect of run-out table cooling on a thick walled X70 steel. During run-out table cooling, the steel undergoes several phase transformations that will affect its microstructure, and thus, its mechanical properties. To predict the steel microstructure at the end of the run-out table, three different models were developed.

The thermal model based on a previous finite element thermal analysis, predicts the temperature history of a thick walled X70 skelp through the run-out table. The validation of the model was done by measuring the coiling interrupt temperature at the surface of the skelp at the end of the run-out table.

To model the phase transformation during run-out table cooling, the microstructure of different steels was predicted for constant cooling rate transformation. This metallurgical model proposed a new approach to process dilation curves in order to predict the evolution of the fraction of austenite transformed during continuous cooling. With this technique, the transformation of austenite into ferrite and bainite was considered simultaneous and not sequential, as it is commonly done in the literature, and improved CCT diagrams were built. The model gave a good approximation of the volume fractions, but the results needs to be confirmed through a thorough microstructure analysis.

The thermal and metallurgical model were then combined in order to predict the evolution of the volume fractions during run-out table cooling. This thermo-metallurgical model was validated by a microstructure analysis of an X70 pipe sample produced in the run-out table. The model was able to accurately predict the microstructure at the centerline and quarter of the skelp, but cannot be used at the surface due to too high cooling rates. The model was also extended to other steels and run-out table configurations, which showed promising results.

# Acknowledgements

I would like to acknowledge and thank first Dr. Hani Henein for taking me as a graduate student in his group and trusting me with this project. Thank you for your invaluable guidance, support and knowledge that helped me throughout these two years. Dr. J.Barry Wiskel, thank you for your advice and for always encouraging me to go further in my work. It was a great honor and pleasure to work with both of you as supervisors.

I also want to thank the group members of the Advanced Materials and Processing Laboratory (AMPL) for their support and help during this project. Special thanks to Corentin, Jonas, Billy, Kartik, Justin and Patrick for their help during the writing process. Thanks to Dr. Laurie Collins of Evraz NA Inc. for his counsel and for providing me with experimental data.

I would like to extend my thanks to Evraz NA Inc., Enbridge, Trans-Canada Pipeline, UT Quality and Alliance Pipelines for their financial sponsorship of this work along with the Natural Sciences and Engineering Research Council (NSERC) of Canada.

Last but not least, I would like to thank my friends and family for their support and patience. I never would have made it as far as I have without all of them.

# Table of Contents

**List of Symbols and Abbreviations** ..... **vii**

**List of Tables** ..... **ix**

**List of Figures** ..... **x**

**Chapter 1: Introduction** ..... **1**

Objectives ..... 1

Thesis outline ..... 1

**Chapter 2: Literature Review** ..... **3**

2.1. Microalloyed steels ..... 3

2.2. Thermomechanical controlled processing ..... 3

2.2.1. Hot rolling process ..... 3

2.2.2. Configuration of the run-out table ..... 5

2.3. Modelling of ROT cooling ..... 6

2.3.1. Heat Transfer Equation ..... 6

2.3.2. Heat transfer modelling ..... 6

2.4. Characterization of phase transformation during continuous cooling ..... 8

2.4.1. Phase diagram ..... 8

2.4.2. Structure identification on CCT Diagrams ..... 9

2.4.3. Model of the phase transformation for continuous cooling ..... 10

2.4.4. Experimental characterization of the phase transformation ..... 12

2.5. Characterization of phase transformation during ROT cooling ..... 13

**Chapter 3: Thermal Model** ..... **15**

3.1. ROT configuration ..... 15

3.2. Simplifying assumptions ..... 16

3.3. Boundary conditions ..... 17

3.4. Material properties ..... 20

3.5. Results of the thermal model ..... 21
3.6. Experimental validation of the model ..... 24
**Chapter 4: Metallurgical Model ..... 26**
4.1. Steel composition ..... 26
4.2. Dilation curve analysis ..... 27
4.2.1. Description of the dilation curves ..... 27
4.2.2. Application of lever rule ..... 28
4.3. Prediction of the fraction of austenite transformed ..... 30
4.3.1. Curve fitting with the Avrami equation ..... 30
4.3.2. Modified form of the Avrami equation ..... 32
4.3.3. Analytical solution of the problem ..... 34
4.3.4. Optimization of the Avrami parameters by statistical bootstrap method ..... 36
4.3.5. Results of curve fitting ..... 37
4.4. Determination of the volume fractions ..... 39
4.4.1. Derivation of the modified curve ..... 39
4.4.2. Results of the predicted volume fractions ..... 44
4.5. Experimental validation of the model ..... 45
4.5.1. Volume fraction measurements ..... 45
4.5.2. Analysis of the micrographs ..... 45
4.5.3. Digitalization of the micrographs ..... 46
4.6. CCT diagrams ..... 49
4.6. Other steels ..... 52
4.6.1. Evraz X70-B ..... 52
4.6.2. Canmet - X80 steel ..... 63
4.7. Metallurgical model summation ..... 69
**Chapter 5: Thermo-metallurgical Model ..... 70**
5.1. Application of the Scheil's additivity rule to ROT cooling ..... 70

5.1.1. ROT cooling rate ..... 71
5.1.2. Application of the Scheil's additivity rule to the estimated cooling rate ..... 75
5.1.3. Application to X70-A steel without strain ..... 79
5.1.4. Application to X70-A steel with strain ..... 81
5.2. Experimental validation of the microstructure model prediction ..... 83
5.3. Other steels ..... 85
5.3.1. Evraz steel – X70-B ..... 85
5.3.2. Canmet – X80 steel ..... 89
5.3. Application of the model ..... 92
5.3.1. Comparison of the model results at two different positions ..... 92
5.3.2. Application of the model on three different steel compositions ..... 94
5.3.3. Application of the model on different ROT configurations ..... 95
5.4. Thermo-metallurgical model summation ..... 100
**Chapter 6: Conclusions & Future Work ..... 101**
6.1. Conclusions ..... 101
6.2. Future work ..... 102
**References ..... 103**
**Appendix ..... 106**
Appendix A: Heat transfer equations ..... 106
Appendix B: Description of the run-out table ..... 108
Appendix C: Steel compositions ..... 110
Appendix D: Thermal history of the Gleeble X70-A samples ..... 111
Appendix E: Modification of the Avrami equation ..... 112
Appendix F: Analytical solution of the Avrami parameters ..... 114
Appendix G: Comparison between the Avrami parameters for the three steels studied ..... 117
Appendix H: Derivation of the modified curves ..... 120
Appendix I: Intermediary results of the metallurgical model for the X70-B and X80 steels ..... 122

# List of Symbols and Abbreviations

ROT: run-out table

TMCP: thermomechanical controlled processing

FRT: finish rolling temperature

CIT: coiling interrupt temperature

TTT: time-temperature transformation

CCT: continuous cooling transformation

FE: finite element

FEA: finite element analysis

b: constant in the isothermal form of the Avrami equation

c: specific heat [J/(K.kg)]

CR: cooling rate [°C/s]

f: fraction of austenite transformed

$f^{-1}$: modified form of the fraction of austenite transformed

h: heat transfer coefficient [W/($m^2$.K)]

n: parameter in the Avrami equation

Q: activation energy (Avrami parameter) [J]

$Q_V$ : latent heat of transformation [J]

R: ideal gas constant [J/(mol.K)]

s: slope of the modified form of the Avrami equation

t: time [s]

T: temperature [K or °C]

$T_0$: temperature at which continuous cooling starts [°C]

$T_{start}$: starting temperature of austenite transformation [°C]

$T_1$(start): starting temperature of the formation of structure 1 [°C]

$T_2$(start): starting temperature of the formation of structure 2 [°C]

$T_1$(stop): finishing temperature of the formation of structure 1 [°C]

$T_2$(stop): finishing temperature of the formation of structure 2 [°C]

$\alpha$: weight parameter associated with the slope of the modified form of the Avrami equation

$\beta$: weight parameter associated with the slope of the modified form of the Avrami equation

$\varepsilon$: emissivity factor

$\Phi$: heat flux [$W/m^2$]

$\lambda$: thermal conductivity [W/(m.K)]

$\rho$: density [$kg/m^3$}

$\sigma$: Stefan-Boltzman constant [$W/(m^2.K^4)$]

$\tau$: characteristic time [s]

$\tau_0$: time constant in the Avrami equation [s]

# List of Tables

Table 2- 1: Modified forms of the Avrami equation. ..... 11

Table 3- 1: Composition of the X70 steel used in the run-out table. ..... 20
Table 3- 2: Specific heat capacity of X70 steel [25]. ..... 20
Table 3- 3: Thermal conductivity of X70 steel [25]. ..... 20
Table 3- 4: Latent heat of transformation [25]. ..... 21

Table 4- 1: Comparison between the X70 steel used in the ROT and the X70 used in the Gleeble machine ..... 26
Table 4- 2: Values of the Avrami parameters for three curve fitting tests. ..... 31
Table 4- 3: Comparison of the steel composition between two X70 steels. ..... 52
Table 4- 4: Comparison of the steel composition between the X80 steel from Canmet and the X70 steel used in the Evraz ROT. ..... 63

Table 5- 1: Starting transformation temperature for different cooling rates. ..... 75
Table 5- 2: Comparison between the volume fractions obtained without and with strain considerations at the centerline and quarter of the skelp for the X70-A steel. ..... 82
Table 5- 3: Comparison of the volume fractions between the centerline and quarter of the skelp for three steels. ..... 93
Table 5- 4: Volume fractions measured at the end of the ROT at three different positions. ..... 94

Table C- 1: Composition of the steel used in the ROT ..... 110
Table C- 2: Composition of the X70 steel used to obtain the dilation curves ..... 110

# List of Figures

Figure 2- 1: Schematic of a hot rolling process [8]. 4
Figure 2- 2: Schematic diagram of TMCP and microstructures changes at each stage [32]. 4
Figure 2- 3: Schematic of ROT [6]. 5
Figure 2- 4: Comparison between measured and predicted temperature at the surface [25]. 7
Figure 2- 5: Fe-C phase diagram for a carbon content between 0 and 7wt% [11]. 8
Figure 2- 6: Experimentally developed CCT diagram for an X70 steel (Evraz). 10
Figure 2- 7:(a) Thermal dilation curve of an X70 steel. (b) Illustration of the lever rule [16]. 13

Figure 3- 1: General layout of the run-out table. 15
Figure 3- 2: Schematic of the configuration of one water bank. 16
Figure 3- 3: Schematic of laminar cooling/skelp interaction transverse to skelp motion [10]. 17
Figure 3- 4: Schematic of the laminar cooling region. 18
Figure 3- 5: Heat transfer coefficient for the X70 steel [24]. 19
Figure 3- 6: Mesh of the FEA region. 19
Figure 3- 7: Colored map of the final temperature of all nodes of the FEA region. 21
Figure 3- 8: Thermal history of the three control nodes in the middle of the FEA region. 22
Figure 3- 9: Thermal history of nodes the three control nodes under the jet impact. 23
Figure 3- 10: Thermal history of the three control nodes on the right side of the FEA region. 23
Figure 3- 11: Comparison between the experimental CIT and the CIT predicted by the model at the surface (node A) for two different ROT configurations. 25

Figure 4- 1: Dilation curves obtained for different cooling rates. 27
Figure 4- 2: Illustration of the lever rule applied to the 10°C/s dilation curve. 28
Figure 4- 3: Positioning of the two tangents on the four dilation curves. 29
Figure 4- 4: Evolution of the fraction of austenite transformed for 1, 3, 5 and 10°C/s. 30
Figure 4- 5: Curve fitting results with three different set of Avrami parameters. 31
Figure 4- 6: Modified form of the fraction transformed of austenite for 1, 3, 5 and 10°C/s. 33
Figure 4- 7: CCT Diagram of the X70 steel used in the ROT (Evraz). 33
Figure 4- 8: Distribution of the Avrami parameters obtained with the bootstrap method for 1°C/s. 36
Figure 4- 9: Modified form of the fraction of austenite transformed for 1°C/s. 37

Figure 4- 10: Avrami parameters found for the two branches of the modified curve depending on the cooling rate..... 38
Figure 4- 11: Curve fitting of the fraction transformed data for 1, 3, 5, and 10°C/s. ..... 39
Figure 4- 12: Curve fitting of the modified form of the fraction transformed. ..... 40
Figure 4- 13: Slopes of the modified curves for different cooling rates. ..... 41
Figure 4- 14: Evolution of the parameters α with temperature for different cooling rates. ..... 42
Figure 4- 15: Modified curve obtained for the formation of structure 1 and structure 2. ..... 43
Figure 4- 16: Evolution of the experimental and predicted fraction transformed and of the volume fraction of structures 1 and 2 with temperature for different cooling rates. ..... 44
Figure 4- 17: Micrographs of the dilation samples for different cooling rates. ..... 46
Figure 4- 18: Distribution of the gray level for the four micrographs. ..... 47
Figure 4- 19: Processed micrographs for each cooling rates. ..... 48
Figure 4- 20: Comparison between the experimental and predicted volume fraction at the end of four different continuous cooling. ..... 48
Figure 4- 21: Identification of the transformation temperatures on the fraction transformed curve for 1°C/s..... 50
Figure 4- 22: Identification of the transformation temperatures on the slopes curve for 1°C/s. ..... 50
Figure 4- 23: Comparison between the predicted and Evraz CCT diagram. ..... 51
Figure 4- 24: Dilation curves for the Evraz X70-B steel. ..... 53
Figure 4- 25: Evolution of the fraction transformed of austenite for different cooling rates (Evraz X70-B steel). ..... 54
Figure 4- 26: Evolution of the volume fraction with the temperature for different cooling rates (Evraz X70-B steel). ..... 55
Figure 4- 27: Modified curve and curve fitting associated for 1 and 3°C/s (Evraz X70-B steel). ..... 57
Figure 4- 28: Evolution of the fraction transformed for the "three structures" approach for 1 and 3°C/s (Evraz X70-B steel). ..... 57
Figure 4- 29: Comparison between the Evraz and computed CCT diagram considering the formation of only two structures for the Evraz X70-B steel. ..... 59
Figure 4- 30: Comparison between the Evraz CCT diagram and the computed one using the "three structures approach" for the Evraz X70-B steel. ..... 60
Figure 4- 31: Micrographs of the dilation samples at different cooling rates (Evraz X70-B steel). ..... 61
Figure 4- 32: Comparison between the experimental and predicted volume fractions for the different cooling rates (Evraz X70-B steel). ..... 62

Figure 4- 33: Comparison between the experimental and predicted volume fractions obtained with the "three structures" approach for the different cooling rates (Evraz X70-B steel). ..... 63
Figure 4- 34: Dilation curves of the X80 samples for several cooling rates. ..... 64
Figure 4- 35: Fraction transformed for different cooling rates (X80 steel). ..... 65
Figure 4- 36: Fraction of austenite transformed for different cooling rates (X80 steel). ..... 66
Figure 4- 37: Predicted CCT diagram for the X80 steel ..... 67
Figure 4- 38: Comparison between the experimental and predicted volume fractions for the different cooling rates (X80 steel). ..... 68

Figure 5- 1: Position of the control nodes on the FEA region. ..... 70
Figure 5- 2: Thermal history of the control nodes. ..... 71
Figure 5- 3: Cooling rate of ROT cooling at the three control nodes A (surface), B (quarter) and C (centerline). ..... 72
Figure 5- 4: Thermal history of the surface node A and at a location 1.5mm below A. ..... 73
Figure 5- 5: Evolution of the cooling rates with temperature for nodes C (centerline) and B (quarter). ..... 74
Figure 5- 6: Estimation of the cooling rates for the centerline and the quarter node. ..... 74
Figure 5- 7: Evolution of the cooling rate estimation at the centerline with temperature. ..... 76
Figure 5- 8: The thermal history of the centerline is divided into regions of constant cooling rate. ..... 76
Figure 5- 9: Fraction transformed of each cooling rate used for the Scheil's additivity rule. ..... 77
Figure 5- 10: Evolution of the theoretical fraction transformed with temperature during the run-out table cooling. ..... 78
Figure 5- 11: Evolution of the theoretical fraction transformed with time during the run-out table cooling. ..... 78
Figure 5- 12: Evolution of the computed volume fraction of austenite, ferrite and bainite during the run-out table cooling. ..... 79
Figure 5- 13: CCT diagram predicted by the model. ..... 80
Figure 5- 14: Scheil's additivity rule applied with the shifted transformation temperatures. ..... 82
Figure 5- 15: Location of the samples. (a) Schematic of the pipe. (b) Schematic of the quarter of the pipe B. (c) Schematic of part of the pipe where the samples are taken. ..... 83
Figure 5- 16: Micrographs of an X70 pipe samples at three different locations, mechanically polished and etched with LePera etchant. ..... 84
Figure 5- 17: Comparison between the experimental and predicted volume fractions at different locations. ..... 85

Figure 5- 18: Cooling rate of ROT cooling at the centerline and quarter node (left) and their approximations for the Evraz X70-B steel (right)..... 86
Figure 5- 19: Evolution of the volume fractions during ROT cooling for the Evraz X70-B steel at the centerline and quarter..... 87
Figure 5- 20: CCT diagram predicted by the model using the "three structures approach" for the Evraz X70-B steel..... 88
Figure 5- 21: Comparison between the experimental and predicted volume fractions at different locations for the Evraz X70-B steel..... 89
Figure 5- 22: Cooling rate of ROT cooling at the centerline and quarter node (left) and their approximations for the X80 steel (right)..... 90
Figure 5- 23: Evolution of the volume fractions during ROT cooling for the X80 steel at the centerline and quarter..... 91
Figure 5- 24: Volume fraction predicted for ROT cooling at the centerline and quarter of the X80 skelp.92
Figure 5- 25: CCT diagram predicted by the model for the Evraz X70-A steel..... 93
Figure 5- 26: Volume fractions at the centerline measured experimentally and predicted for three different steels for ROT cooling..... 94
Figure 5- 27: Temperature profiles at the centerline for three different ROT configurations with the Evraz X70 steel..... 95
Figure 5- 28: Volume fractions at the end of the ROT for the Evraz X70-A steel and for three different ROT configurations..... 96
Figure 5- 29: Volume fractions at the end of the ROT for the Evraz X70-B steel and for three different ROT configurations..... 97
Figure 5- 30: Evolution of the volume fractions at the centerline for an early and late cooling configuration for the Evraz X70-B steel..... 97
Figure 5- 31: Temperature profile at the centerline for three different ROT configurations..... 98
Figure 5- 32: Volume fractions at the end of the ROT for the Evraz X70-A steel and for three different ROT configurations..... 99
Figure 5- 33: Volume fractions at the end of the ROT for the X80 steel and for three different ROT configurations..... 99

Figure B- 1: Layout of the run-out table..... 108

Figure D- 1: Thermal history of the dilation samples for different cooling rates..... 111

Figure E- 1: Linear regression of the Avrami equation plotted with $lnT0 - TCR$ for different cooling rates ..... 112
Figure E- 2: Linear regression of the Avrami equation plotted with $1RT$ for different cooling rates ..... 113

Figure G- 1: Parameter n found for branch 1 of the linearized curve for the three steels. ..... 117
Figure G- 2: Parameter n found for branch 2 of the linearized curve for the three steels. ..... 118
Figure G- 3: Parameter $\tau_0$ found for branch 1 of the linearized curve for the three steels. ..... 118
Figure G- 4: Parameter $\tau 0$ found for branch 2 of the linearized curve for the three steels. ..... 119

Figure H- 1: Slopes of the linearized curve and the two branches for 10°C/s. ..... 120
Figure H- 2: Modified slopes of the linearized curves for different cooling rates. ..... 121

Figure I- 1: Slopes of the linearized curves for the X70-B steel. ..... 122
Figure I- 2: Evolution of the parameter α with temperature for the X70-B steel ..... 123
Figure I- 3: Slopes of the linearized curves for the X80 steel. ..... 124
Figure I- 4: Evolution of the parameter α with temperature for the X80 steel ..... 125

# Chapter 1: Introduction

Microalloyed steels produced using thermomechanical controlled processing are used extensively for pipeline material in the oil/gas industry. The mechanical properties of the steel are important, since pipelines are usually subjected to harsh conditions, such as high pressures and temperatures. The mechanical properties of the steel are directly linked to its microstructure. The microstructure is a product of all stages in the thermomechanical controlled process including homogenizing, hot rolling and laminar cooling. During this later process the steel undergoes several phase transformations that will affect its microstructure. Predicting the evolution of the microstructure of the steel during laminar cooling will therefore help achieving better mechanical properties in the finished product.

## Objectives

The objective of this thesis is to model and measure the effect of run-out table cooling on the microstructure of a thick walled X70 steel. To achieve these objectives, the following model components were developed: a finite element thermal model, a multi-phase transformation model for continuous cooling based on the Avrami equation and the combination of these two models with the Scheil additivity rule [5] to account for the phase transformation during run-out table cooling. The specific objectives developed in this thesis for each model are:

- Thermal model: predict the thermal history of the skelp during run-out table cooling.
- Metallurgical model: since run-out cooling can be approximated by a succession of continuous cooling, the objective is therefore to model the evolution of multiple phase transformations during continuous cooling.
- Thermo-metallurgical model: Combine the thermal and metallurgical models to predict the evolution of the volume fractions during run-out table cooling.

## Thesis outline

The microstructure of the steel is strongly influenced by the thermal history of the skelp in the run-out table. A thorough understanding is needed to determine the effect of the run-out table cooling on the microstructure. A finite element thermal model of the run-out table is applied in this work to the cooling of a thick walled X70 steel.

During run-out table cooling, the skelp undergoes a phase transformation from austenite to ferrite and/or bainite and/or pearlite. In the literature, this phase transformation of austenite has been dealt with the Avrami equation. The Avrami equation is only valid for a single phase transformation and for either isothermal or constant cooling rate transformation, however, actual ROT cooling is characterized by variable cooling rate. The phase transformation during continuous cooling will be initially investigated and then, a new approach will be developed, in order to consider the formation of multiple structures simultaneously under conditions of variable cooling rate.

The Avrami equation predicts the microstructure of a steel for continuous cooling. To generalize it to non-continuous cooling, the Scheil additivity rule [5] will be applied. The thermal and metallurgical model will therefore be combined to predict the evolution of the microstructure for three different steels as well as for both standard run-out table conditions and for idealized/modified run-out table conditions to assess the effect of cooling rate modifications on the phase transformation. Additionally, to validate the model, the microstructure of a pipe sample will be characterized and compared to the predicted results.

# Chapter 2: Literature Review

The objective of this thesis is to determine the effect of run-out table (ROT) cooling on the steel microstructure. The thermomechanical controlled processing (TMCP), and especially ROT cooling, determine the microstructure of the finished product, as such they will be described in this section. To predict the steel microstructure at the end of the ROT, a thermal model and a phase transformation model are needed. A review of thermal model of ROT cooling will be presented. This will be followed by a review of different methods used to characterize phase transformations. A method combining both the thermal and phase transformation models, in order to predict the evolution of the microstructure during ROT cooling, will then be presented.

## 2.1. Microalloyed steels

Many steels used in the fabrication of pipelines and other finished products, such as steel plates or rails are microalloyed steel. Microalloyed steels represent approximately 10% of the global steel production [1]. These steels contain less than 0.25wt% of carbon and are usually alloyed with chemical elements such as niobium (Nb), titanium (Ti) or vanadium (V) [1]. The level of addition is typically under 0.10% hence the name of microalloyed. The role of these additions is to increase the mechanical properties of the steel. It results in cheaper and more effective finished products, which justifies the use of microalloyed steels in the pipeline industry.

## 2.2. Thermomechanical controlled processing

In this section, thermomechanical controlled processing and more specifically, the run-out table will be presented.

### 2.2.1. Hot rolling process

The steel microstructure and thus, the mechanical properties depend on thermomechanical controlled processing (TMCP). As described in many studies [2-8], the material undergoes different steps during the process, as shown in Figure 2-1. The steel is first casted into a strip, which goes then through a reheat furnace, where it reaches approximately 1200°C. The strip is then flattened out through the rolling mills, in order to obtain the thickness prescribed (i.e. usually 1 to 20 mm). Finally, the steel is cooled down to a temperature of approximately 550°C in the run-out table (ROT), right before being coiled by an up or down coiler.

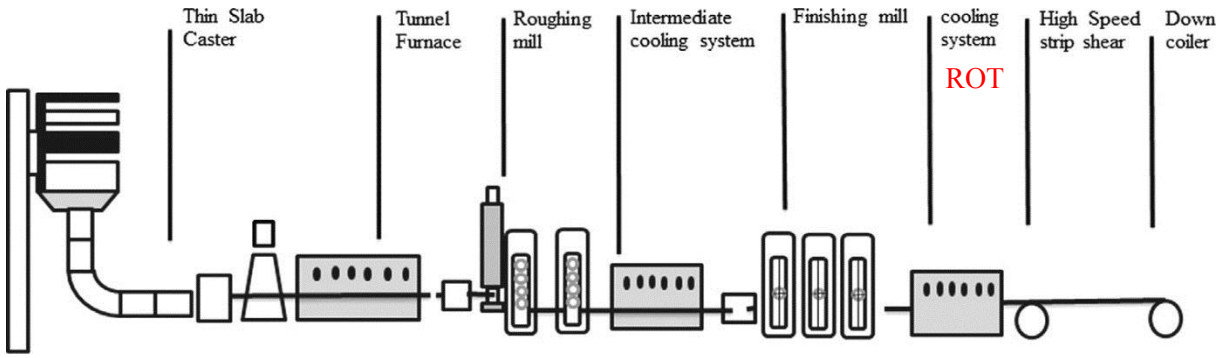


*Figure 2- 1: Schematic of a hot rolling process [8].*

TMCP, coupled with the addition of with microalloying elements, determine the shape, mechanical properties and metallurgy of the skelp, as presented in Figure 2-2. The skelp is first reheated to only have austenite in the steel. The skelp is then rolled, which leads to recrystallized and pancaked austenite grains. Following the hot rolling process, laminar cooling of the steel is a crucial step, since the phase transformations occurring during this step will determine the steel microstructure. Specifically, the austenite from hot rolling is transformed into a number of structures including; ferrite, bainite, pearlite and martensite [3]. This thesis will therefore be focused on the steel microstructure produced during ROT cooling.

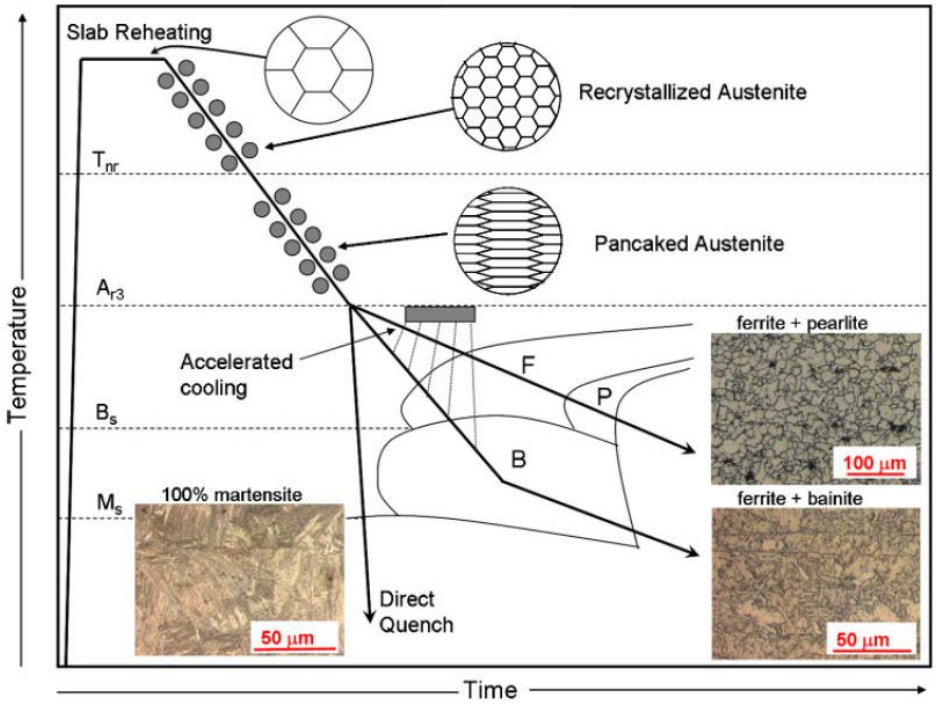


*Figure 2- 2: Schematic diagram of TMCP and microstructures changes at each stage [32].*

### 2.2.2. Configuration of the run-out table

The purpose of the ROT is to cool down the steel skelp from a finish rolling temperature (FRT) of approximately 800°C to a pre-determined coiling interrupt temperature (CIT). A general layout of the ROT is presented in Figure 2-3.

The ROT consists in the succession of water banks that usually discharge water onto the skelp through three systems: the water sprays, the laminar flow streams and the water curtain, as described by Xu [4]. The water sprays system uses sprays to apply water onto the surface of the steel in order to cool it down to the coiling interrupt temperature (CIT). The water curtain system is even more efficient, because the steel is cooled down by a planar jet that covers the entire width of the strip. However, this study will only focus on the laminar flow streams system used in the Evraz ROT.

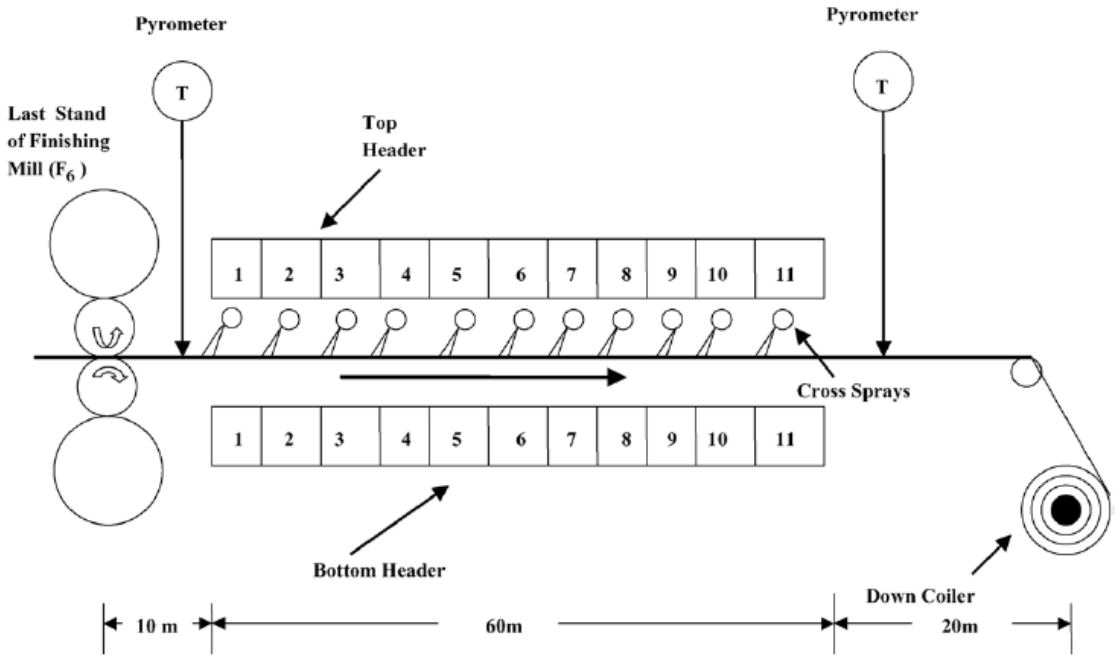


*Figure 2- 3: Schematic of ROT [6].*

ROT cooling on the upper surface can be divided in three different sections. The first section, located right after the finishing rolling mills, consist of a radiative cooling zone. It is followed by a water cooling section, comprising of several water banks and side sprays positioned after each water bank. For each water bank the laminar flow system is composed of rows of pipes that discharge water onto the strip. The direct impact of the water and the water remaining on the skelp provide the majority of cooling. The water film that forms at the surface can be removed by the side sprays that follow every water bank.

Finally, the third portion of the ROT is another radiative cooling section, located between the last water bank and the coiler. The interaction between water and the surface is complex, due to the different cooling mechanisms that intervene during this process [5].

## 2.3. Modelling of ROT cooling

In this section, the heat transfer equation used to model ROT cooling and a review of finite element analysis used to solve this equation will be presented.

### 2.3.1. Heat Transfer Equation

The objective of the thermal model is to predict the temperature profile of the steel skelp. The theory behind the heat transfer is well established and has been used in several studies [6-8]. The 3D heat transfer equation is based on the conservation of energy and expressed as follow (the details of the heat transfer analysis are presented in Appendix A):

$$\nabla.(\lambda \nabla T) + \mathrm{Q}_V - c\rho \frac{\partial T}{\partial t} = 0 \tag{2.1}$$

To solve the heat transfer equation, boundary conditions are needed. As mentioned previously, three different phenomena can occur at the surface of the skelp [5]: direct impact water, film boiling, and radiation. The two convection equations and the radiation equation are expressed as follow:

$$\begin{cases} \phi_{impact} = -\lambda \nabla \mathrm{T} = h_{impact}(T - T_{water}) \\ \phi_{film} = -\lambda \nabla \mathrm{T} = h_{film}(T - T_{vapor}) \\ \phi_{air} = -\lambda \nabla \mathrm{T} = \sigma \varepsilon (T^4 - T_\infty{}^4) \end{cases} \tag{2.2}$$

Where $\phi_{impact}$ and $\phi_{film}$ and $\phi_{air}$ are the heat fluxes through the surface; $\mathrm{T_{water}}$, $\mathrm{T_{vapor}}$ and $T_\infty$ are the temperature of the liquid water, vapor and the surrounding respectively; $\mathrm{h_{water}}$ and $\mathrm{h_{vapor}}$ are the heat transfer coefficients of water and vapor; and σ and the ε are the Stefan-Boltzman constant and the emissivity factor.

### 2.3.2. Heat transfer modelling

In the literature, the heat transfer equation during ROT cooling is usually solved using a finite element (FE) analysis. Suebsomran et al. [7-8] solved the thermal analysis numerically by applying a backward difference formula to discretization of partial differentiation equation [7]. However, in this work, to reduce the computation time, the problem has been simplified by only considering one type of convection at the surface and no radiative cooling. The variables parameters of the ROT have then been

fitted to match the experimental measurements at the surface. A consequence of the model simplification is that a slight modification of one of these parameters, could result in an important difference between the model prediction and the experimental measurements. Thus, this approach does not accurately represent the heat transfer mechanisms during ROT cooling, and the model is therefore only valid for a specific ROT configuration.

A more accurate method has been used by Wiskel et al. [10] to model ROT cooling of a microalloyed steel. The heat transfer problem has been solved using a finite element (FE) thermal analysis. In this FE analysis, the three boundary conditions in Equation 2.2 were implemented in the model and the calculations were done using the software package ABAQUS/CAE™ by Dassault systèmes. This method results in a more accurate prediction of the temperature history of the skelp during ROT cooling. The surface temperature predicted are in a good agreement with the values measured, as presented in Figure 2-4.

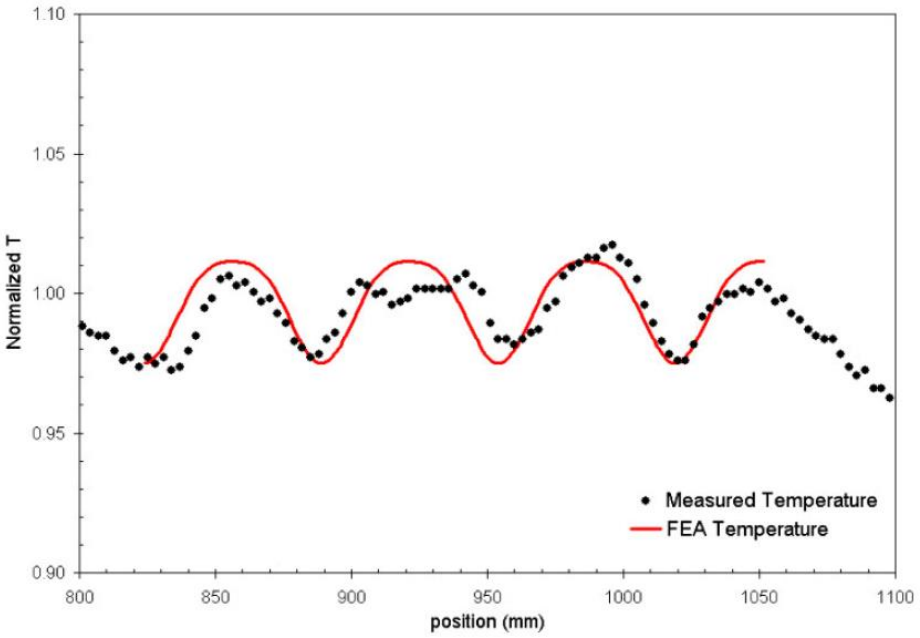


*Figure 2- 4: Comparison between measured and predicted temperature at the surface [25].*

The benefit of the method used by Wiskel et al. [10], is that it accurately represent the heat transfer mechanism in the ROT, and thus, this model will also be used in this thesis. Additionally, infrared images at the surface of the skelp as revealed cold spots that may be due to the formation of oxides. However, these oxides are not evenly spread at the surface of the skelp, and they only influence the cooling right below the surface. Thus, for the scope of this thesis, the influence of oxides will not be considered.

## 2.4. Characterization of phase transformation during continuous cooling

In this section the steel microstructure will be described using, phase diagrams and continuous cooling transformation (CCT) diagrams. To characterize the evolution of phase transformation during continuous cooling, metallurgical models based on different forms of the Avrami equation will be discussed and a technique to experimentally determine this evolution will be presented.

### 2.4.1. Phase diagram

As mentioned previously the steel skelp undergoes several phase transformations during ROT cooling. In order to characterize the phase transformations, an iron-carbon phase diagram can be used. A phase diagram represents the temperature ranges, where the different phases are thermodynamically stable, for different compositions [11]. Thus, phase diagrams are only based on thermodynamic and do not consider kinetic transformations.

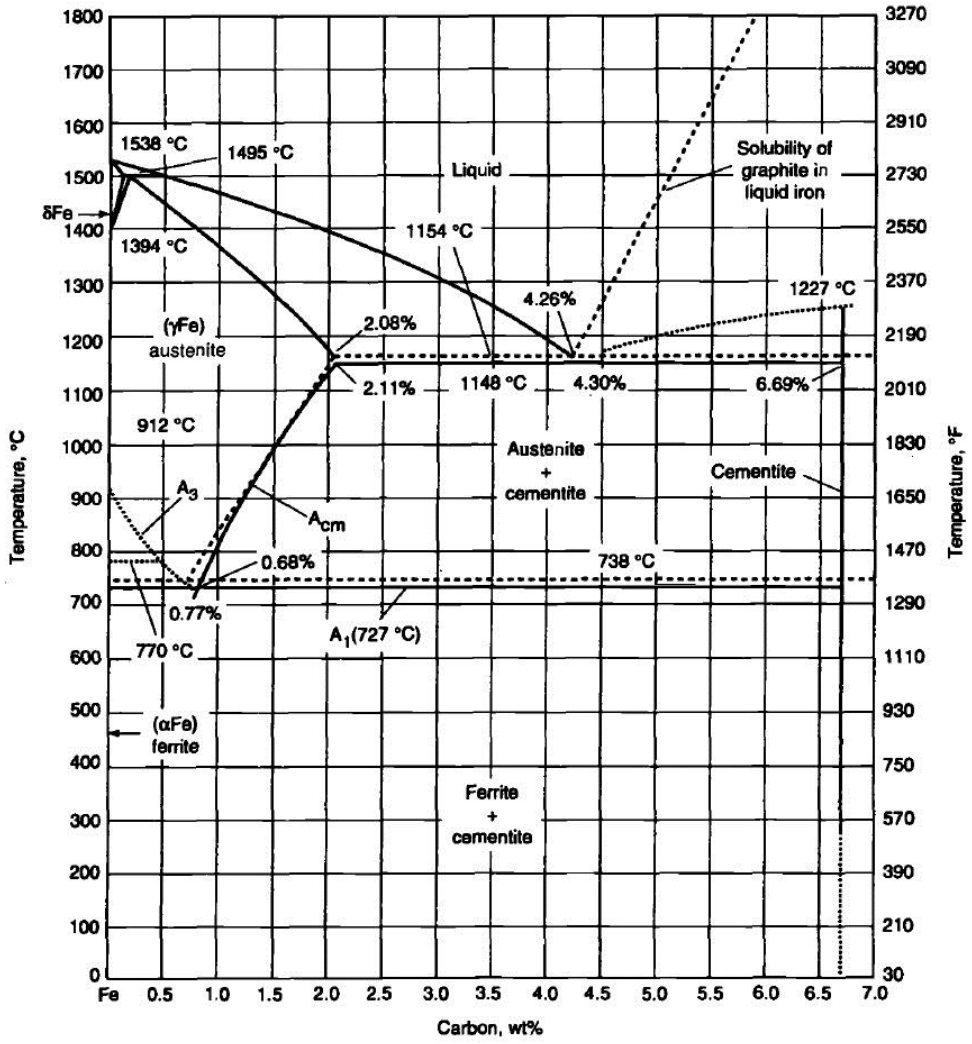


*Figure 2- 5: Fe-C phase diagram for a carbon content between 0 and 7wt% [11].*

One of the steels that will be used in this study has a carbon content of 0.049wt%. After the finishing rolling mills, the steel comes out at a temperature of about 800°C. The coiling temperature is usually between 600 and 500°C. Looking at the phase diagram in Figure 2-5 it appears that during this transformation, the austenite will transform into both ferrite and cementite. However, it has been shown in the literature [12] that the steel microstructure at the end of the ROT shows some other structures like bainite or pearlite. The presence of these structures shows that a thermodynamic approach is not sufficient to describe the phase transformations and the evolution of the microstructure in the steel.

### 2.4.2. Structure identification on CCT Diagrams

One way to consider kinetic transformations is to look at isothermal transformation or time-temperature-transformation (TTT) diagrams. TTT diagrams are used to characterize isothermal transformation because it is a simple way to describe phase transformations [13]. However, ROT cooling is not fast enough to be approximated by an isothermal transformation.

A more appropriate way to describe the transformation kinetics in the ROT is to use constant cooling transformation (CCT) diagrams. CCT diagrams represent the evolution of the transformation of a parent structure into one or multiple structures with time and for a given constant cooling rate [14]. CCT diagrams are divided into structure domains that delimit the temperature range of the formation of the different structures. For example, in Figure 2-6, for the transformation at 10°C/s, when the curve crosses the first line at approximately 660°C, it means that the austenite starts forming into ferrite and when it crosses the second line at approximately 450°C, the transformation is complete.

Most CCT diagrams in the literature [13-14] consider the transformation of austenite into ferrite, bainite, pearlite or martensite sequentially, which means that the new structures are assumed to form one after the other. It can be seen on the CCT diagram in Figure 2-6 because all the structure domains are clearly separated from each other. It means that the formation of each structure is assumed to happen one after the other.

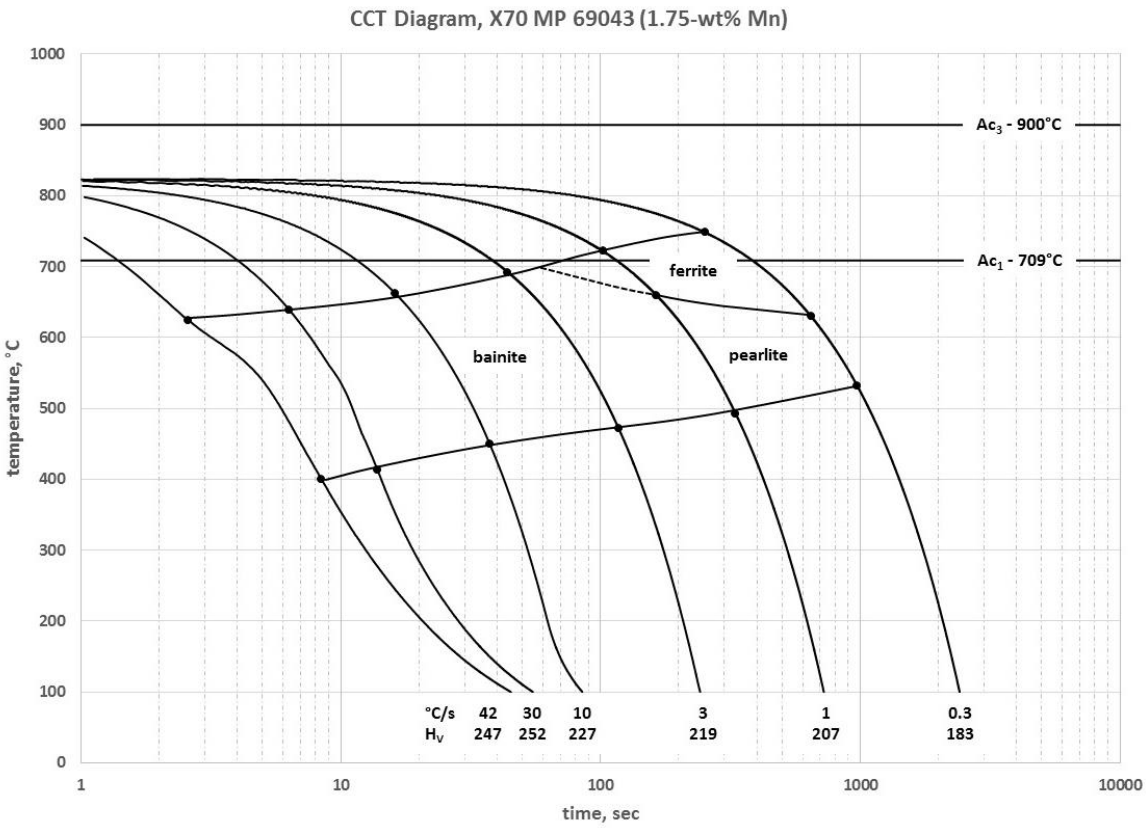


*Figure 2- 6: Experimentally developed CCT diagram for an X70 steel (Evraz).*

### 2.4.3. Model of the phase transformation for continuous cooling

In this section, a model for the decomposition of austenite will be presented. The kinetics for isothermal phase transformations is commonly used and has been developed by Johnson, Mehl, Avrami, Kolmogorov (JMAK) in 1939 [17-18]. This experimental model gives the evolution of the volume fraction f of the new structure that forms over time for an isothermal transformation:

$$f = 1 - \exp(-bt^n) \tag{2.3}$$

Where b and n are two parameters that depends on the material and are often empirically measured. In the literature, the value of n is usually between 0 and 4 [19-31]. This value depends on the transformation mechanism and the type of nucleation site. The parameter b is also a constant that depends on the material, and which is usually determined empirically [19-20].

The Avrami equation is relatively simple and has been modified in several studies, to more accurately predict the evolution of the fraction of austenite transformed. Six different versions of the Avrami equation are presented in Table 2-1.

*Table 2- 1: Modified forms of the Avrami equation.*

| Reference | Modified form of the Avrami equation | No. |
|---|---|---|
| [17] | $f = 1 - exp(-bt^n)$ | (2.4) |
| [20] | $f = 1 - exp(-bt^n)$ <br> $b = -\frac{\ln(1 - X_s)}{t_s^n}$ | (2.5) |
| [21] | $f = 1 - exp(-bt^n)$ <br> $b = P(1)exp\left(-\left(\frac{T - P(2)}{P(3)}\right)^{P(4)}\right)$ | (2.6) |
| [31] | $f = 1 - exp(-bt^n)$ <br> $ln(b) = 1.80 + 0.03(T_{Ae_3} - T) - 1.9(1 - A\varepsilon)ln(d_\gamma)$ | (2.7) |
| [33] | $f = A\left(1 - exp\left(\left(\frac{1}{d_\gamma^m}\int_{T_s}^{T}\frac{exp\left(\left(b_1(T_{Ae_3} - T') + b_1\right)/n\right)}{CR}dT'\right)^n\right)\right)$ | (2.8) |
| [22] | $f = 1 - \exp\left(-\left(\frac{t}{\tau}\right)^n\right)$ <br> $\tau = \tau_0 exp\left(-\frac{Q}{RT}\right)$ | (2.9) |

Equations 2.4, 2.5 and 2.6 have all three been developed for isothermal transformations. For Equation 2.4 and 2.5 the parameters b and n are determined experimentally on TTT diagrams. The form of Equation 2.6 is more complex and depend also on the carbon and manganese content, the prior austenite grain and $A_{e3}$ temperature.

The issue with these three equations is that it has only been developed for an isothermal transformation. ROT cooling could have been approximated by an isothermal reaction if the cooling rate was high enough. However, the cooling rate of the ROT is approximately 20°C/s which is not enough to make this assumption. Thus, continuous cooling is more appropriate to approximate ROT cooling.

The Avrami equation has been generalized to continuous cooling reactions in several works. Equations 2.7, 2.8 and 2.9 were developed for continuous cooling. Both equations 2.7 and 2.8 depends on the prior austenite grain size, $A_{e3}$ temperature and retained strain. Additionally, these two expressions were developed for a particular steel and have therefore coefficients that are specific to the material (i.e.

the coefficients in the expression of ln(b) in 2.7, and the coefficients $b_1$ and $b_2$ in 2.8). Thus, for each steel, the coefficients must be determined experimentally.

The form the Avrami equation used in this thesis is the one used by Venkatraman et al. [22], and is expressed in Equation 2.9. This specific form of the Avrami equation has been chosen, due to the physical meaning of the parameters introduced, which can be determined experimentally. The parameter $\tau$ is the characteristic time and can be expressed using two constants: the time $\tau_0$ and the activation energy Q as shown in Equation 2.9. Thus, this continuous cooling form of the Avrami equation depend on a triplet of parameters (n, Q, $\tau_0$) that needs to be experimentally determined. As described by Venkatraman et al., the method used to determine these parameters is to fit the Equation 2.9 to experimental data.

### 2.4.4. Experimental characterization of the phase transformation

As presented by Kop et al. [15] or Liu et al. [16], a common technique to obtain the evolution of the fraction of austenite transformed is to use the lever rule on the dilation curves.

Dilation curves are obtained from a Gleeble or a dilatometer test. For both methods, the steel samples are first austenitized at a temperature above the A3 temperature, which is the temperature below which ferrite starts to form. Thus, the only structure present in the steel is austenite. The samples are then cooled down at a constant cooling rate, and dilation curves are obtained measuring the evolution of their dilation, as shown in Figure 2-7(a). On a dilation curve, one or several rebound can be observed, which corresponds to a volume increase of the dilation sample and characterize a phase transformation.

The lever rule then calculates the ratio between transformed and untransformed austenite from the dilation curves. The two branches before and after the rebound, shown Figure 2-7(b), correspond then to untransformed and transformed austenite respectively. The fraction of austenite transformed is calculated at every temperature during the transformation, as the ratio between the distance from the austenite branch to the dilation curve, and the distance between the two tangents.

The experimental evolution of the fraction of austenite transformed is commonly used to validate the phase transformation model [5-20], or to determine the parameters of the Avrami equation using curve fitting algorithms [22].

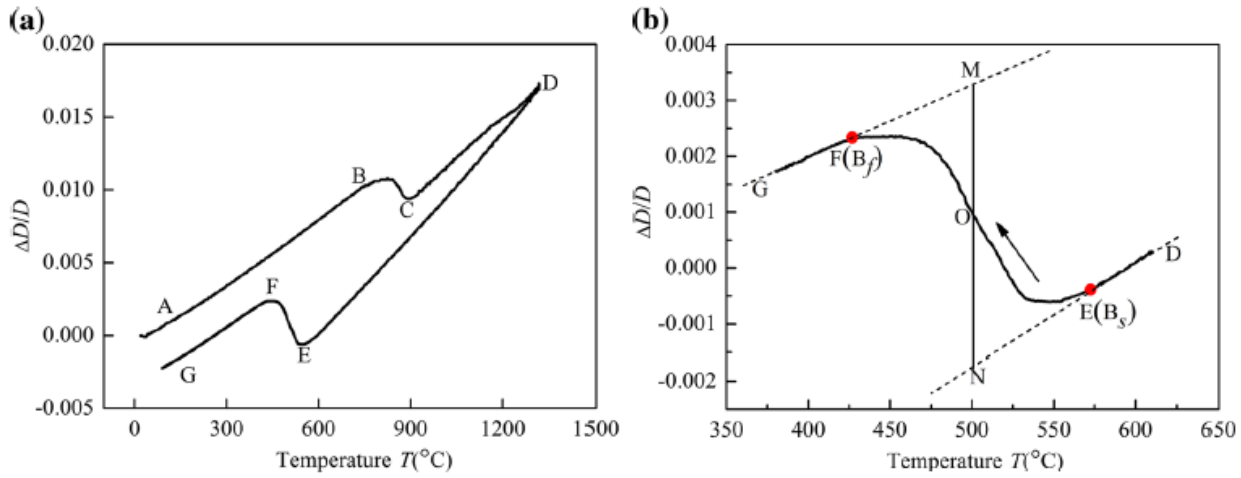


*Figure 2- 7:(a) Thermal dilation curve of an X70 steel. (b) Illustration of the lever rule [16].*

## 2.5. Characterization of phase transformation during ROT cooling

To model the evolution of the phase transformation during ROT cooling, the Scheil additivity rule is commonly used [5-20-31]. The Scheil additivity rule consists in applying an additivity principle on the derivative form of the Avrami equation. This technique has been mostly developed for the isothermal form of the Avrami equation [5-20]. For non-isothermal transformation, such as ROT cooling, the temperature profile is divided in small isothermal transformations, to which is applied the specific Avrami equation. This principle is summed up in Equation 2.10 for the basic form of the Avrami equation 2.4 [5]:

$$\begin{cases} f_{i+1} = 1 - \exp(-b_i(t_i^* + \Delta t_i)^n) \\ t_i^* = \left(-\frac{1}{b_i} ln\left(\frac{1-f}{f_i}\right)\right)^{1/n} \end{cases} \quad (2.10)$$

However, as mentioned previously, approximating ROT cooling with isothermal reactions is not really accurate. A more relevant technique is to use continuous cooling, as presented by Pandi [31]. The same principle is used, except for the fact that ROT cooling is now divided in a succession of continuous cooling transformation.

However, as mentioned previously, the modified Avrami Equation 2.7, is too complicated to implement for ROT cooling since due to the number of unknown parameters and coefficients. Thus, Scheil additivity rule will be applied in a manner similar to Pandi [31] (i.e. with continuous cooling) but with the form of the Avrami equation introduced by Venkatraman et al. [22] Equation 2.9. The form of

Equation 2.10 can then be extended to Equation 2.9, in order to characterize the phase transformation, as follow:

$$\begin{cases} f_{i+1} = 1 - \exp\left(-\left(\dfrac{t_i^* + \Delta t_{i+1}}{\tau_{i+1}}\right)^n\right) \\ t_i^* = \left(\dfrac{ln(1-f_i)}{\tau_{i+1}}\right)^{1/n} \end{cases} \tag{2.11}$$

Equation 2.10 will therefore be applied to ROT cooling in order to predict the evolution of the phase transformation.

# Chapter 3: Thermal Model

A finite element (FE) thermal analysis of the run-out table was used to determine the temperature profile of the skelp during laminar cooling. The basic model was developed in previous work by Wiskel et al. [10] and was modified to the analysis of a thick skelp X70 steel (i.e. 17.3mm). A brief description of the run-out table (ROT) configuration, the FE thermal model, the thermal and physical properties and the boundary conditions will be presented. The thermal profile will be analyzed and then validated by a comparison between the predicted and measured ROT temperature.

## 3.1. ROT configuration

To model heat transfer in the ROT, the configuration to implement during the calculation need to be described. The ROT studied in this thesis is based on the one used by EVRAZ as they provided experimental data that was used for experimental validation of the developed model.

The ROT is positioned between the finish rolling mills and the coiler as presented in Figure 3-1. A full layout of the run-out table is presented in Appendix B. To cool down the steel strip the ROT has the capability to use six water banks. Each water bank consists of the series of six lines of 40 evenly spaced nozzles (in the Y direction), as shown in Figure 3-2, that deliver a laminar stream of water onto the surface of the steel strip. All the water banks are immediately followed by side sprays to remove any water remaining on the top surface of the skelp.

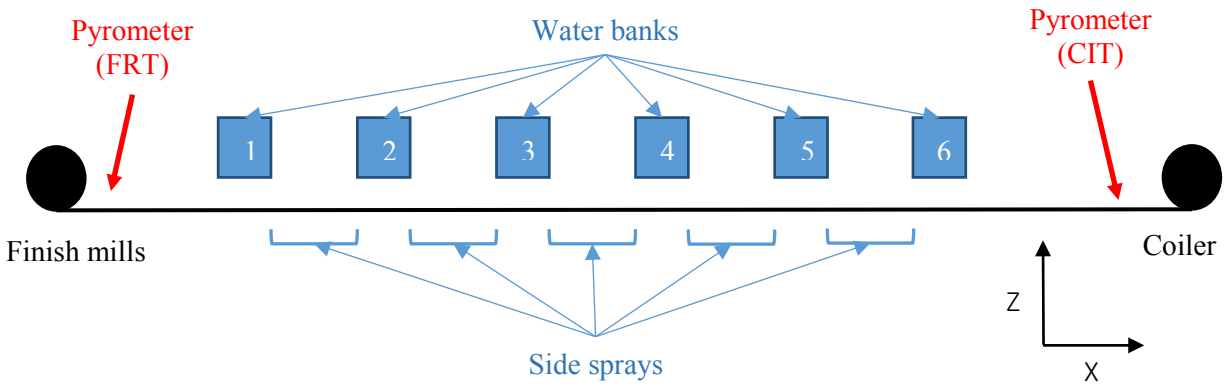


*Figure 3- 1: General layout of the run-out table.*

To control the steel temperature, pyrometers are positioned between the finish rolling mill and the first water bank, as well as between the end of the ROT and the coiler. Those pyrometers measure the

finish rolling temperature (FRT) and the coiling interrupt temperature (CIT), as shown in Figure 3-1. The FRT measured by the pyrometer will be the initial condition for the temperature of the skelp. It is assumed that the temperature of the whole strip is uniform and equal to the FRT measured by the first pyrometer. According to plant measurements done by Evraz, the FRT is equal to 788°C. Another variable is the initial velocity of the strip, which was assumed to be 2.35m/s for the simulations conducted.

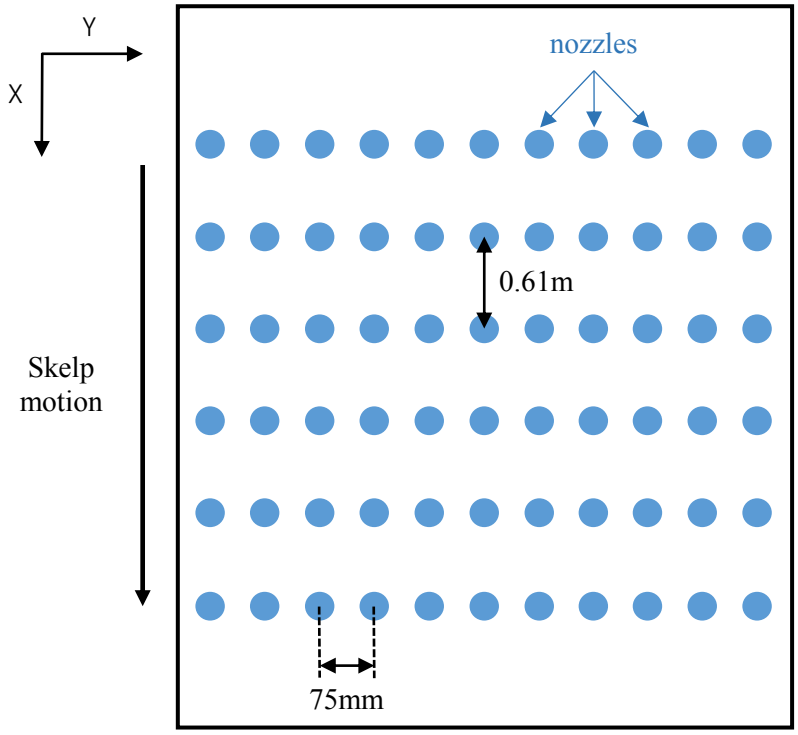


*Figure 3- 2: Schematic of the configuration of one water bank.*

With the configuration of the ROT defined it is now possible to look at simplifying the cooling experienced by the skelp.

## 3.2. Simplifying assumptions

Based on the geometry of the system, the ROT configuration and the heat transfer mechanisms, the following assumptions were made in the original model:

1) Symmetry with the centerline: the top and bottom cooling are assumed identical.
2) Heat flow in the transverse direction: the longitudinal heat flow is not considered.
3) Symmetry of the nozzles: the 40 nozzles are evenly spaced and considered identical

With these assumptions applied, the ROT model can be simplified to a single two-dimensional rectangle, as shown in Figure 3-3, greatly reducing the required calculation time. Figure 3-3 only shows two out of the 40 nozzles (in the Y direction) that are comprised in each of the six lines of each water bank. This 2D rectangular region can be further separated into two regions: one directly under the impact of the water jet which will be called the "impact zone" and the one next to it which is the "film boiling zone" or "film zone".

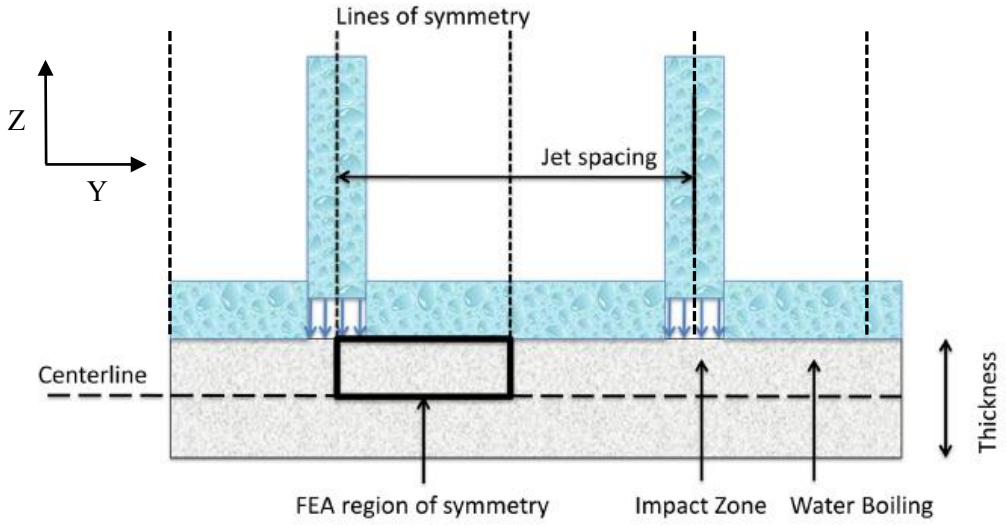


*Figure 3- 3: Schematic of laminar cooling/skelp interaction transverse to skelp motion [10].*

The FE thermal analysis is then applied to the 2D rectangular region (shown in Figure 3-4) to solve the 2D heat transfer equation, expressed as follow:

$$\left( \frac{\partial}{\partial y}\left(\lambda \frac{\partial T}{\partial y}\right) + \frac{\partial}{\partial z}\left(\lambda \frac{\partial T}{\partial z}\right)\right) + \mathrm{Q} - c\rho \frac{\partial T}{\partial t} = 0 \qquad (3.12)$$

Where λ, ρ and c are the thermal conductivity, the density and the specific heat of the material respectively. Q is the latent heat of transformation for austenite to ferrite.

## 3.3. Boundary conditions

With the FEA region set, boundary conditions now need to be defined. Since the bottom and the sides of the part are delineated by planes of symmetry, the resultant heat transfer is considered equal to zero at these positions. So all the heat is conducted through the part and lost at the surface.

At the surface of the steel, the heat transfer mechanisms are complex and have been simplified for the thermal model. Due to the important difference of temperature between the hot steel and the cold water, a vapor film is created at the surface. Nevertheless, at each nozzle the liquid water flow is sufficient to penetrate this vapor cloud and reach the surface of the skelp. This region where liquid water is directly in contact with the steel is restricted to a certain area. The schematic of this region is presented Figure 3-4. In this zone the heat transfer between the skelp and the surrounding is governed by a mechanism of convection between the steel and the liquid vapor. Outside the jet impact region, the water is boiling at the surface which creates a dense vapor film. There, the heat transfer is governed by the water boiling curve, between the steel and the vapor. Finally, after each water bank side sprays blow water across the surface of the strip in order to remove the remaining water. The heat loss in these areas (i.e. no water) is governed by thermal radiation equation.

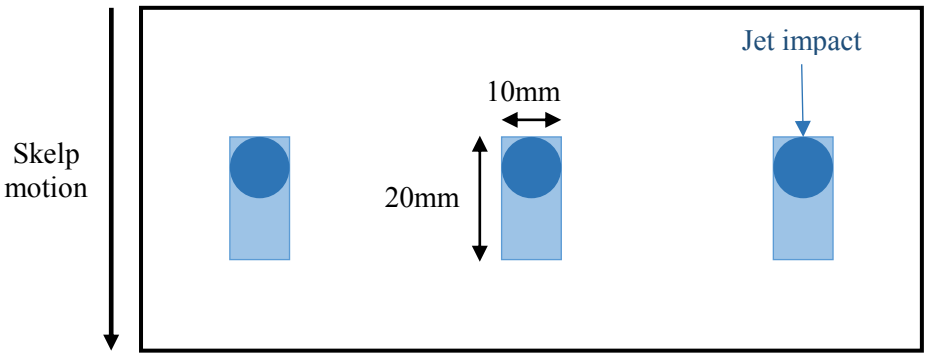


*Figure 3- 4: Schematic of the laminar cooling region.*

The boundary conditions require some heat transfer coefficients (HTC). For the water convection, the HTC depends on the temperature of both the steel and the water:

$$h_{w1} = \frac{10.5e6}{T_s - T_{water}} \; W/(m^2.K) \tag{3.13}$$

Where $T_s$ is the surface temperature and $T_{water}$ the water temperature (assumed to be 25°C). The heat transfer coefficient in the film zone is based on the water boiling curve of Wendelstorf et al. [24] and has been adapted in order to match the steel grade used in this thesis. The evolution of the heat transfer coefficient with the temperature is assumed to be as what is shown in Figure 3-5. And lastly the effective radiation heat transfer is considered constant during the transformation and equal to $h_\infty = 150\, W/(m^2.K)$.

With the boundary conditions set, the studied part must be meshed in order to apply the FEA. The mesh is a decisive step as it determines both the accuracy and computation time of the model. Therefore the mesh has to be finer in regions where the heat transfer is higher. Through each water bank the film boiling zone is only subjected to convection within the vapor, whereas the impact zone alternates between convection with liquid water and vapor. Therefore, the mesh has to be finer under the impact and at the surface due to important heat exchange in those areas. The mesh used in the FE simulation is shown Figure 3-6.

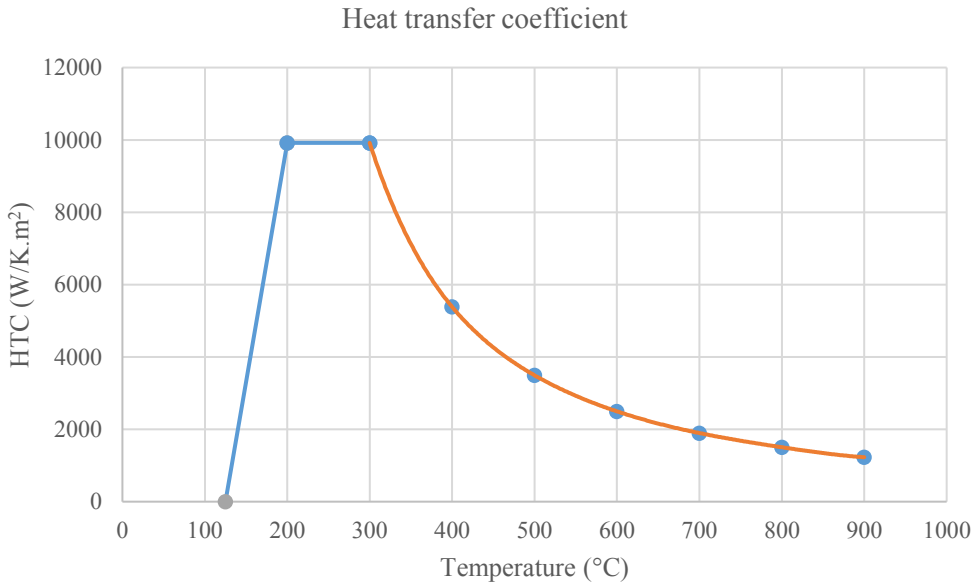


*Figure 3- 5: Heat transfer coefficient for the X70 steel [24].*

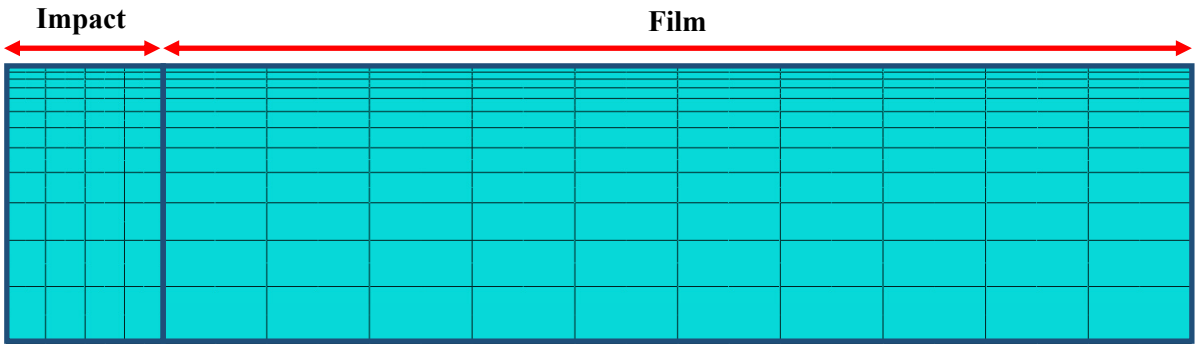


*Figure 3- 6: Mesh of the FEA region.*

## 3.4. Material properties

A part of the chemical composition of the steel used for the FEA is presented Table 3-1 (the full composition is presented in Appendix C). This steel is a microalloyed X70 steel. Even if the steel composition is not needed for the finite element model it affects all the material properties. The density of the steel is 7900kg/m$^2$ and is assumed constant during the whole run-out table cooling.

*Table 3- 1: Composition of the X70 steel used in the run-out table.*

| **Identification: X70 - ROT - 17.3mm** | | | | | |
|---|---|---|---|---|---|
| **C** | **Mn** | **Cr** | **Mo** | **Nb** | **Si** |
| 0.043 | 1.67 | 0.09 | 0.192 | 0.067 | 0.26 |

The thermal conductivity is needed and depends on the temperature as shown Table 3-2. Since the process involves variations of temperature and phase transformations, the specific heat capacity of the steel and the latent heat of transformation are required. Both material properties are temperature dependent (Table 3-3 and Table 3-4). The latent heat of transformation of austenite was thermodynamically estimated by Wiskel et al. [25], considering the austenite transformation occurs over a temperature range from 700 to 550°C. This value could be more accurately determined using a differential scanning calorimeter (DSC).

*Table 3- 2: Thermal conductivity of X70 steel [25].*

| **Temperature (°C)** | **Thermal Conductivity (W/(m.K))** |
|---|---|
| 0 | 59.5 |
| 100 | 57.8 |
| 200 | 53.2 |
| 300 | 49.4 |
| 400 | 45.6 |
| 500 | 41 |
| 600 | 36.9 |
| 700 | 33.1 |

*Table 3- 3: Specific heat capacity of X70 steel [25].*

| **Temperature (°C)** | **Specific Heat Capacity (J/(kg.K))** |
|---|---|
| 50 | 481 |
| 150 | 519 |
| 250 | 536 |
| 300 | 553 |
| 350 | 547 |
| 400 | 595 |
| 500 | 662 |
| 600 | 754 |
| 700 | 867 |

*Table 3- 2: Latent heat of transformation [25].*

| Latent Heat (J/kg) | $T_{Stop}$ (°C) | $T_{Start}$ (°C) |
|---|---|---|
| 18,000 | 550 | 700 |

## 3.5. Results of the thermal model

The simulation of ROT cooling was undertaken using the software package ABAQUS/CAE™ 6.13 of Dassault Systèmes. The simulation begins at the first pyrometer (at a temperature of 788°C) and ends at the second pyrometer. Figure 3-7 shows a map of the distribution of the temperature at the end of the cooling. The temperature varies from 559.6°C at the coldest point to 595.3°C at the hottest. The coldest temperature can be found at the AL position, located at the surface directly under the jet impact, as shown in Figure 3-7. This is the spot where the cooling is the highest because of the direct contact with the liquid water. Conversely, the hottest temperature is located at the centerline and right in between two water jet (at the node CR).

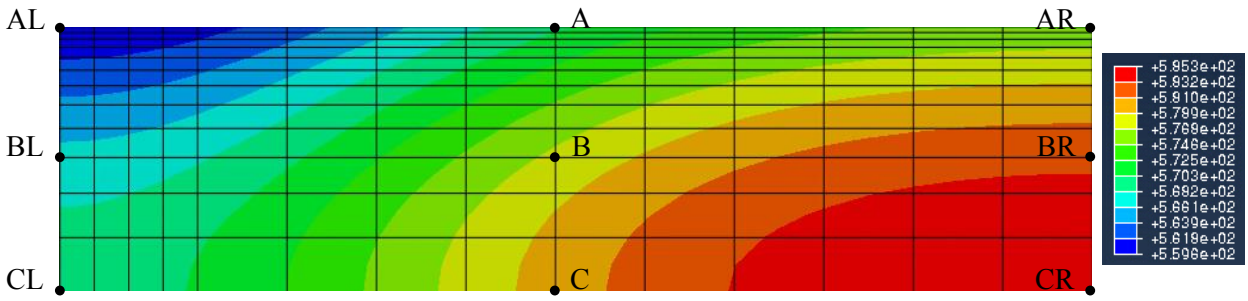


*Figure 3- 7: Colored map of the final temperature of all nodes of the FEA region.*

After the simulation we also have access to the thermal history of every node of the FEA region. We can differentiate three types of nodes: node A located at the surface, node C at the centerline and node B in-between the two. The temperature-time profile for these three nodes (A, B and C) in the middle of the part is presented Figure 3-8. The node at the centerline shows that the cooling rate at this position is fairly constant with a value of approximately 15°C/s. The temperature decreases but it is not really affected by the thermal variations at the surface. The surface node shows an overall cooling rate similar to the one at the centerline but the temperature is less stable during the cooling. Each water bank induces a cooling rate of about 50°C/s for the skelp and is followed by a reheating period. This reheating period after each water

bank is due to the fact that the radiative cooling at the surface is less important than the heat conduction from the nodes below the surface. The surface nodes are cooled by the water which introduce a temperature gradient to the ones below. When the side sprays remove the water from the surface, the radiation cooling cannot compensate the reduction of the temperature gradient that warms the surface nodes. This behavior can also be seen for nodes located a few millimeters under the surface. For those between the surface and the centerline (B nodes) the temperature does not go up but it is leveled out after each water bank.

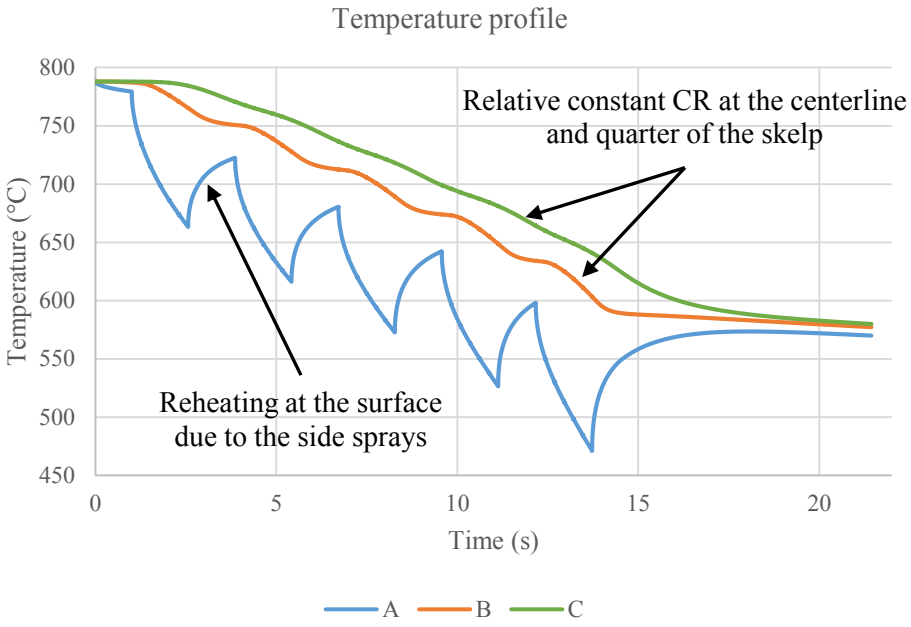


*Figure 3- 8: Thermal history of the three control nodes in the middle of the FEA region.*

Figure 3-9 shows the thermal history of nodes located under the impact of a water jet. The behavior of the nodes BL and CL are similar to the nodes B and C. The main difference is for the node AL. Since this node is located right under the water jet, the thermal history shows the influence of each nozzle. The liquid water, having a more important heat transfer coefficient than the vapor, drops the temperature of the node which then becomes reheated by the nodes located underneath the region between each nozzle.

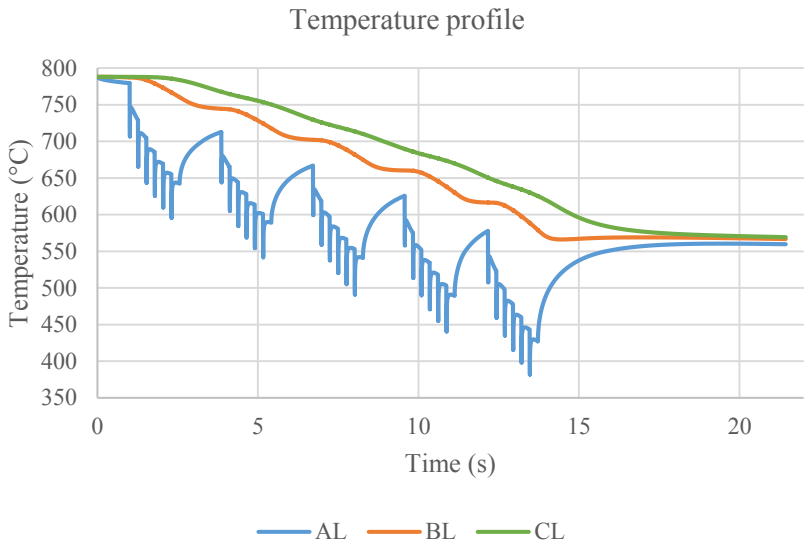


*Figure 3- 9: Thermal history of nodes the three control nodes under the jet impact.*

The temperature-time profile of nodes AR, BR and CR at the very right side of the part is shown in Figure 3-10. Those nodes have the exact same behavior as the first ones. The only difference is that at the end of the run-out table their temperature is slightly hotter (about 5°C).

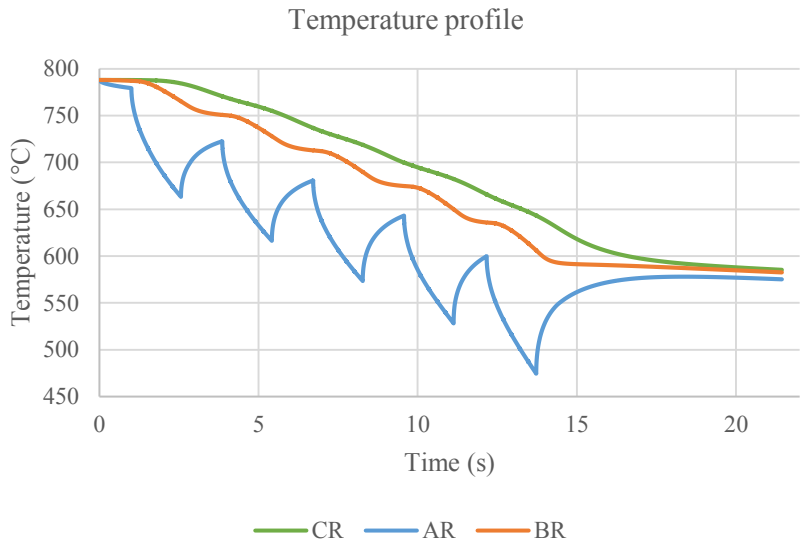


*Figure 3- 10: Thermal history of the three control nodes on the right side of the FEA region.*

Comparing the nodes A, B and C at the different locations shows that there is not a real difference between the nodes at the same depth except for the node AL. This node shows the impact of every nozzle

of each water bank, but this will not be needed for the rest of the study. Therefore we will focus on the nodes A, B and C in the middle of the part. And these nodes will be called the “control nodes”.

The ABAQUS simulation has also been run with a finer mesh that comprises approximately twice as many nodes (i.e. 587 and 1085 nodes) that the mesh used previously. It appears that the results are identical for the two meshes, which indicates that the analysis has reached a convergence point. The aspect ratio (i.e. the ratio between its largest and smallest dimension) of the elements close to the centerline and the surface is equal to 1.8 and 18 respectively. The aspect ratio at the surface seems high, but a simulation with an aspect ratio of 4.5 was done and gave identical results.

## 3.6. Experimental validation of the model

With the ABAQUS simulation we have access to the predicted temperature of every node during the run-out table cooling. The thermal model needs to be validated experimentally but since it deals with an actual industrial process this validation is difficult and limited.

The fact that the strip is moving during its cooling makes it difficult to have access to the temperature inside the skelp. It is impossible to have some thermocouple inside the steel to record the variations of temperature. The only temperature measurements we have access to are those at the surface. However, there is also a technical difficulty. The presence of the industrial setup and the fact that the ROT creates a vapor film on the top of the steel make the measurement of the surface temperature difficult. Thus, the only temperature that is measurable is the finish rolling temperature and the coiling temperature. Those were the two temperatures given by Evraz and were measured using a scanning pyrometer to give the mean temperature at the surface at both stages of the ROT process.

For a given finish rolling temperature (788°C) the coiling temperature has been measured for different runs and configurations. The strip has been cooled down by both five and four water banks and each time the coiling temperature was measured at various times during the process. Figure 3-11 shows the comparison between the experimental and modelled (i.e. at the node A) coiling interrupt temperature. The results of the model and those from measured experiments are in solid agreement for both five and four water bank setups. So it appears that the model is stable concerning the ROT configuration which is a good sign on the reliability of the model.

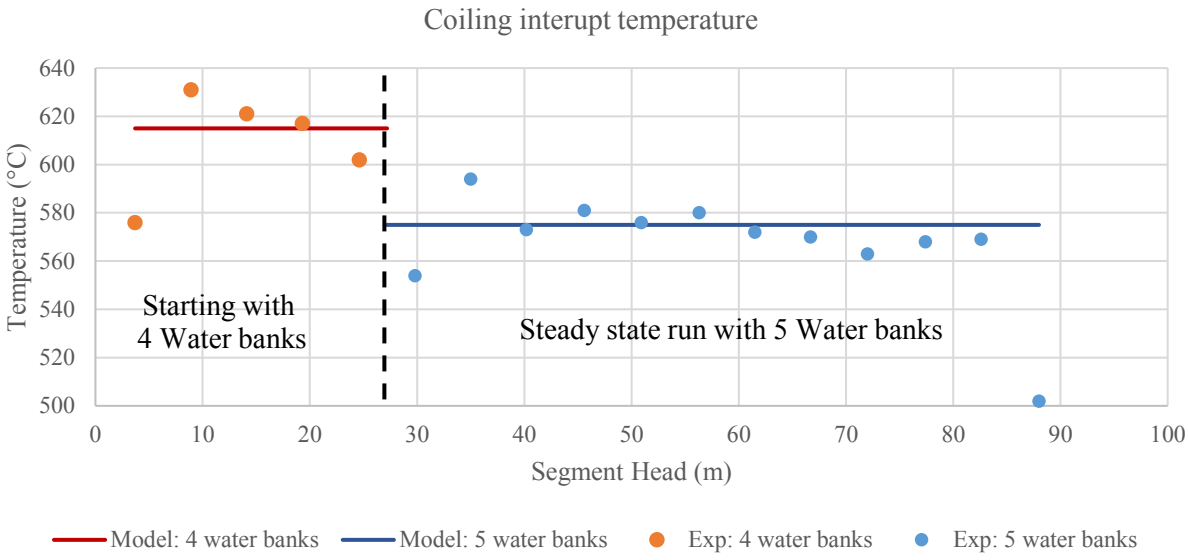


*Figure 3- 11: Comparison between the experimental CIT and the CIT predicted by the model at the surface (node A) for two different ROT configurations.*

Knowing the run-out table conditions and the material properties, it seems that the thermal model can accurately predict the thermal history of the steel strip. Additionally, it appears that the model gives consistent results for different ROT configurations. The benefit of this model is that it shows the thermal history of the strip, which is unavailable with experimental measurements. Since the cooling rate is an important factor in the steel microstructure, it could now be controlled through an optimization of the run-out table configuration.

# Chapter 4: Metallurgical Model

The effect of ROT cooling on the steel microstructure is complicated, as multiple structures are formed simultaneously and the skelp undergoes non-continuous cooling. As discussed in the literature [20-21], the Avrami equation has been used to predict the phase transformation of austenite during continuous cooling. The Avrami methodology has not been applied to simultaneous phase formation (i.e. two or more structures form at the same time). This section describes the metallurgical model that has been developed to predict the multiple structure transformation simultaneously for continuous cooling.

The model was developed using dilation curves obtained from a Gleeble machine and a dilatometer for two X70 steels and for one X80 steel. The fraction of austenite transformed will be determined using the lever rule on the dilation curves, and then fitted using a modified form of the Avrami equation. The simultaneous formation of multiple phases will be incorporated into the metallurgical model, which will be validated using CCT diagrams and micrographs of the dilation samples.

## 4.1. Steel composition

As mentioned previously, the purpose of this study is to predict the evolution of the microstructure of a 17.3mm X70 steel plate during ROT cooling. However, the dilation curves for the steel used in the ROT were unavailable, hence other steel with similar composition will be studied in this section. Evraz provided two different dilatation datasets for two compositions of X70 steels (which will be called X70-A and X70-B) and Canmet one for an X80 steel. What follows is the analysis of one of the datasets, with the results for the others included at the end of this section.

The metallurgical model will be developed with the Evraz X70-A steel that has the most similar composition with the steel used in the ROT. The two compositions are presented in Table 4-1 (the full compositions are presented in the Appendix C). The composition of the analyzed steel is slightly different from the one used in the ROT, since it comprise more carbon, molybdenum and niobium, and less manganese and silicon.

*Table 4- 1: Comparison between the X70 steel used in the ROT and the X70 used in the Gleeble machine*

| | C | Mn | Cr | Mo | Nb | Si |
|---|---|---|---|---|---|---|
| **X70 - ROT** | 0.043 | 1.67 | 0.09 | 0.192 | 0.067 | 0.26 |
| **X70-A steel** | 0.049 | 1.63 | 0.10 | 0.244 | 0.075 | 0.17 |

## 4.2. Dilation curve analysis

In this section, the dilation curves obtained from a Gleeble machine with the X70-A steel will be presented and then processed with the lever rule to obtain the fraction of austenite transformed as a function of temperature.

### 4.2.1. Description of the dilation curves

To develop the metallurgical model, the dilation data of four different cooling rates were obtained experimentally in a Gleeble machine. The dilation samples were heated up to 1050°C and held at this temperature for three seconds before being cooled down at the prescribed cooling rate (1, 3, 5 and 10°C/s). The thermal history of the dilation samples is presented in the Appendix D.

The measured dilation curves for each cooling rate are presented in Figure 4-1. The phase transformation of the steel can be observed through the rebound in the dilation curve. The rebound is characterized by a change in the dilation of the sample (i.e. the volume of the sample increases) as the austenite is transformed. Phase transformations can therefore be observed on the dilation curves, but the curves need to be processed in order to fully characterize the transformation present. It should be noted that the 3°C/s curve shows a dilation oscillation around 650°C. This is assumed to be due to the experimental procedure and not to the sample itself.

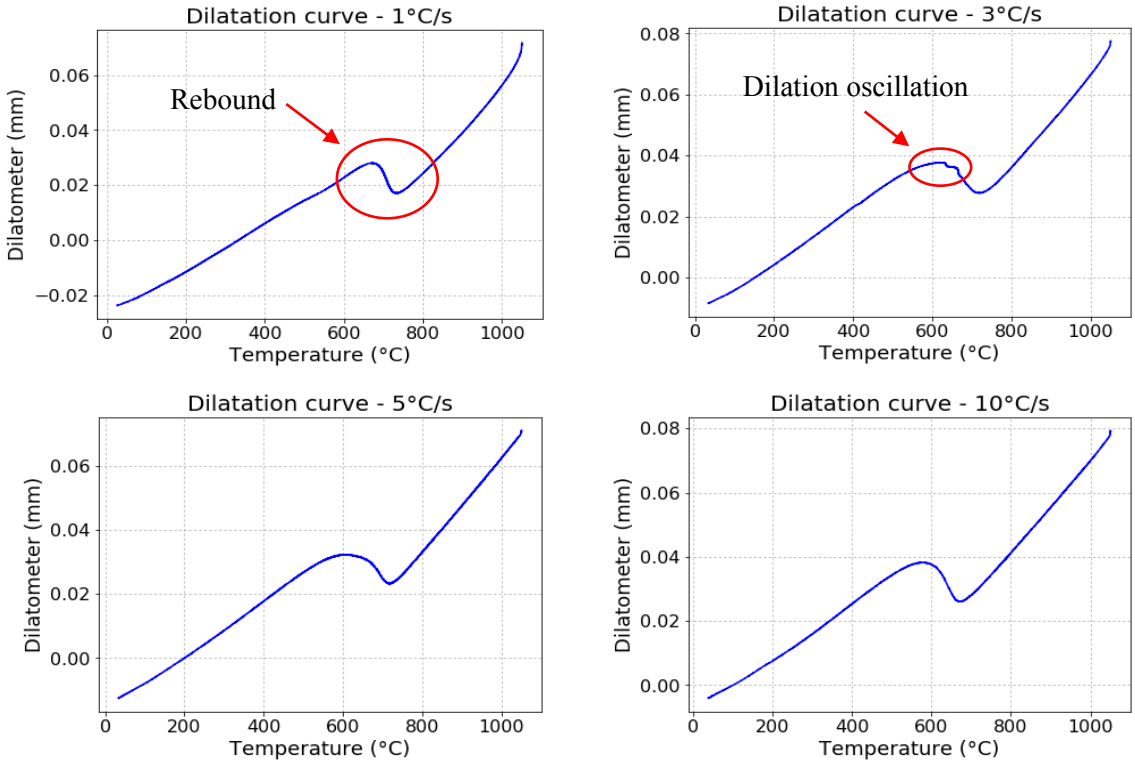


*Figure 4- 1: Dilation curves obtained for different cooling rates.*

### 4.2.2. Application of lever rule

The first step of the dilation curve analysis is to determine the evolution of the transformation of the austenite as a function of temperature. A well-established method to do this is the lever rule. The principle of the lever rule is that the fraction of the new structure relative to the old one can be defined by the deviation of the dilation curve from the line representing the parent structure.

The lever rule is illustrated in Figure 4-2 for 10°C/s and in Figure 4-3, with the line of the parent structure (i.e. the austenite) being the linear portion at the higher-temperature. In order to calculate the fraction f of the austenite transformed, two tangents must first be constructed, one that corresponds to the afore-mentioned parent structure, and the second immediately following the transformation. Because of the scattered nature of the dilation curves, they need to be smoothed in order to accurately position the tangents. The two tangent are then positioned manually as presented in Figure 4-3. The positioning of the two tangents is a crucial step of the metallurgical model, since it will directly affect the final results.

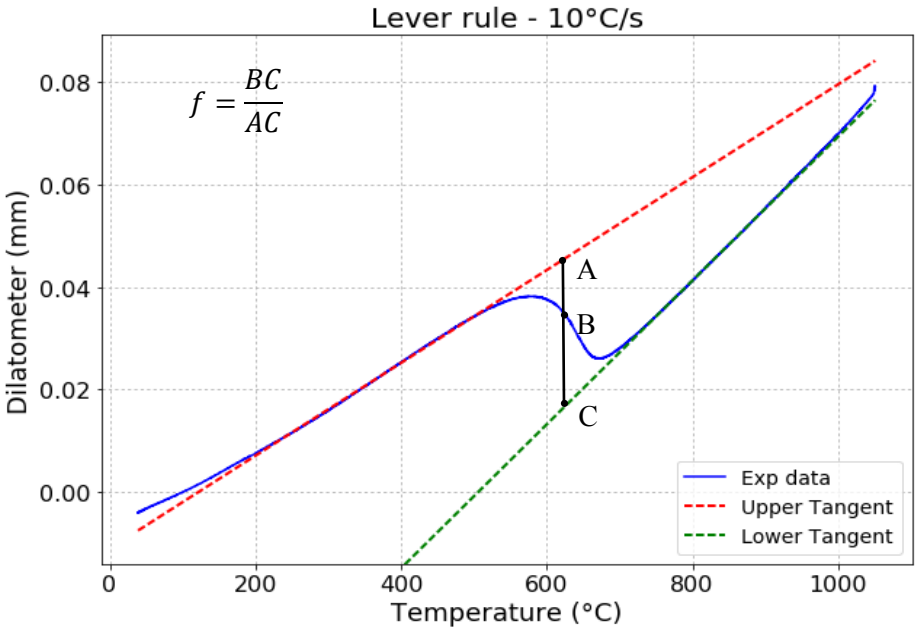


*Figure 4- 2: Illustration of the lever rule applied to the 10°C/s dilation curve.*

The thermal expansion was determined from the slope of the two tangents for each cooling rate. The thermal expansion has a value of $2.3.10^{-5}$ $K^{-1}$ for the austenite and $1.5.10^{-5}$ $K^{-1}$ for ferrite as reported in [36].

It is also important to note that there is a light second rebound on the dilation curve for 1°C/s between 400 and 600°C as shown in Figure 4-3. The rebound on the curve shows the formation of another structure after the first structure, characterized by the first large rebound.

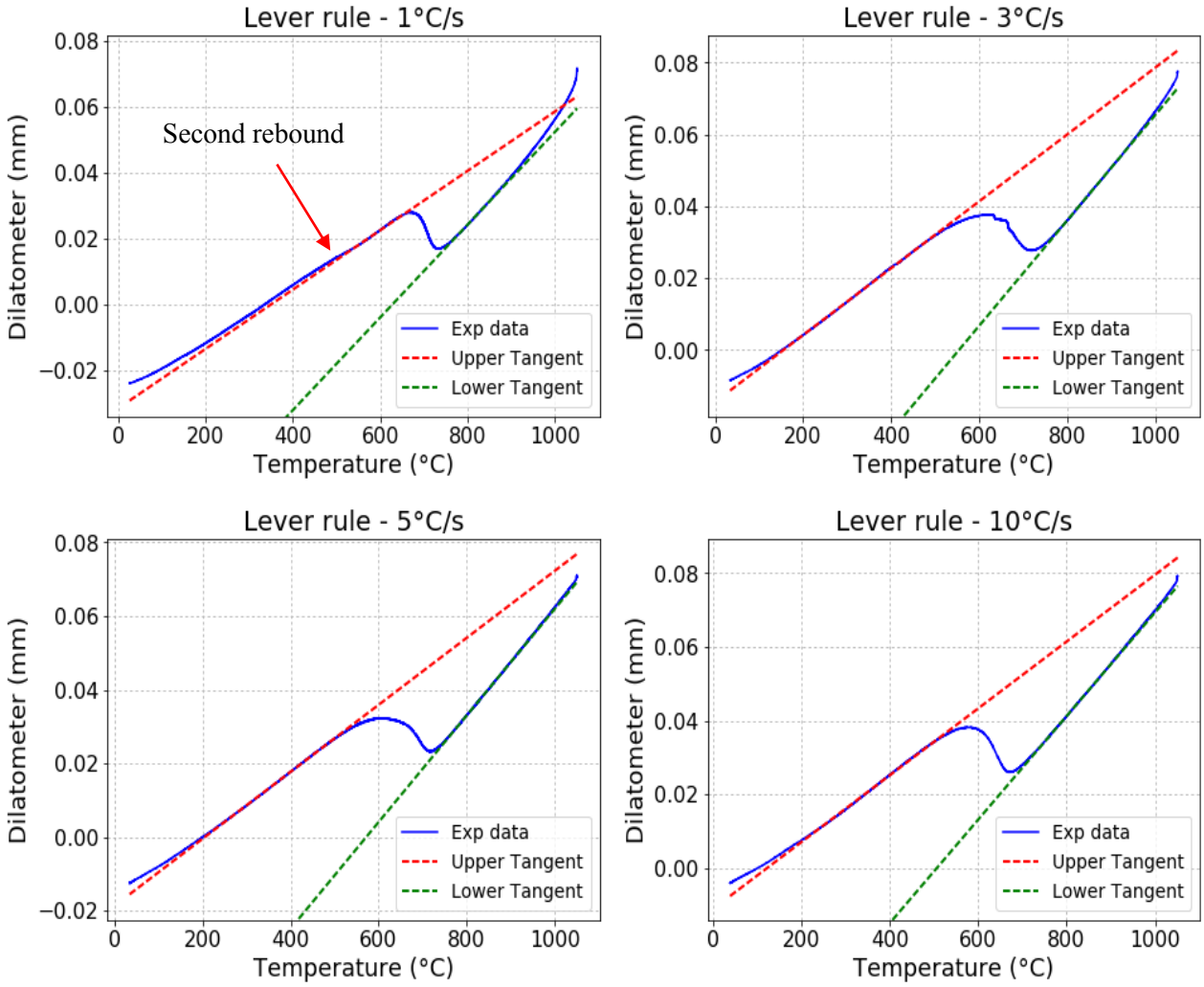


*Figure 4- 3: Positioning of the two tangents on the four dilation curves.*

The fraction transformed is calculated as the ratio between the distance from the austenite branch to the dilation curve, and the distance between the two tangents. The fraction transformed is calculated at every temperature, for each of the four different cooling rates. The results are presented in Figure 4-4.

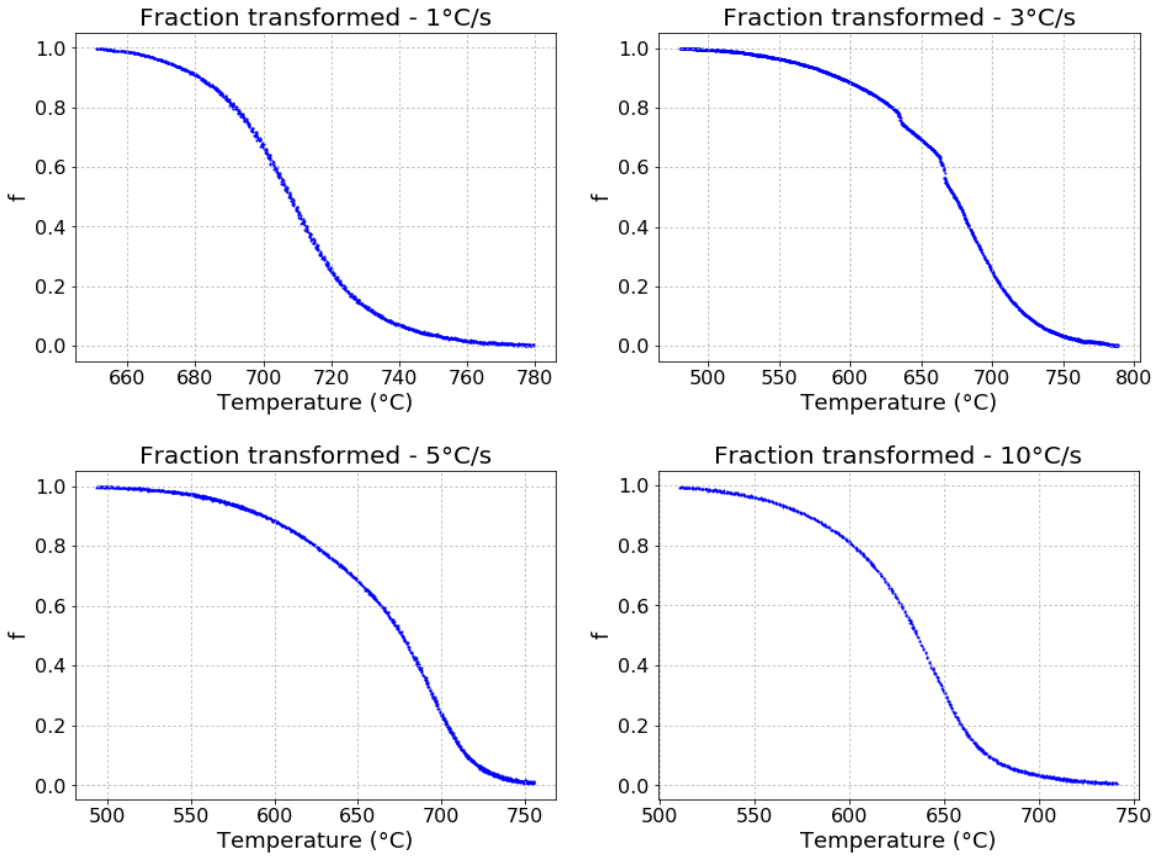


*Figure 4- 4: Evolution of the fraction of austenite transformed for 1, 3, 5 and 10°C/s.*

## 4.3. Prediction of the fraction of austenite transformed

The fractions transformed obtained through the lever rule are experimental in nature. The next step of the model is to find a theoretical expression of the evolution of the fraction transformed that will fit the experimental values. A form of the Avrami equation has been chosen to describe the transformation, which will be fitted to the experimental data. In this section, a curve fitting technique commonly used in the literature is modified in order to predict the evolution of the fraction of austenite transformed during continuous cooling.

### 4.3.1. Curve fitting with the Avrami equation

In the literature, the evolution of the fraction transformed is fitted using the Avrami equation. The usual expression of the Avrami equation corresponds to an isothermal transformation. The basic equation has therefore been transformed by Venkatraman et al. [22] to suit a continuous cooling transformation, and can be expressed as follows:

$$\begin{cases} f = 1 - \exp\left(-\left(\frac{t}{\tau}\right)^n\right) \\ \tau = \tau_0 exp\left(-\frac{Q}{RT}\right) \end{cases} \quad (4.14)$$

f represents the fraction transformed, Q the activation energy and τ the characteristic time. The three parameters (n, Q, $\tau_0$) are constants that depend on the material used. These parameters are called the Avrami parameters and are fitted to the experimental data.

To determine the Avrami parameters, some preexisting curve fitting algorithms, such as the least squares approach have been used. The principle behind this curve fitting algorithm is to minimize the error between the experimental and the theoretical values of the data. Unfortunately, it appears that for different sets of parameters, a similar fit can be found, as shown in Figure 4-5 and Table 4-2. Additionally, the theoretical expression never perfectly fits the experimental data. It shows therefore that working with this form of the Avrami equation is not a suitable way to find a good fit.

*Table 4- 2: Values of the Avrami parameters for three curve fitting tests.*

| | **Test 1** | **Test 2** | **Test 3** |
|---|---|---|---|
| **n** | 7 | 12 | 23 |
| **Q** | 31000 | 17000 | 4000 |
| **$\tau_0$** | 4660 | 710 | 125 |

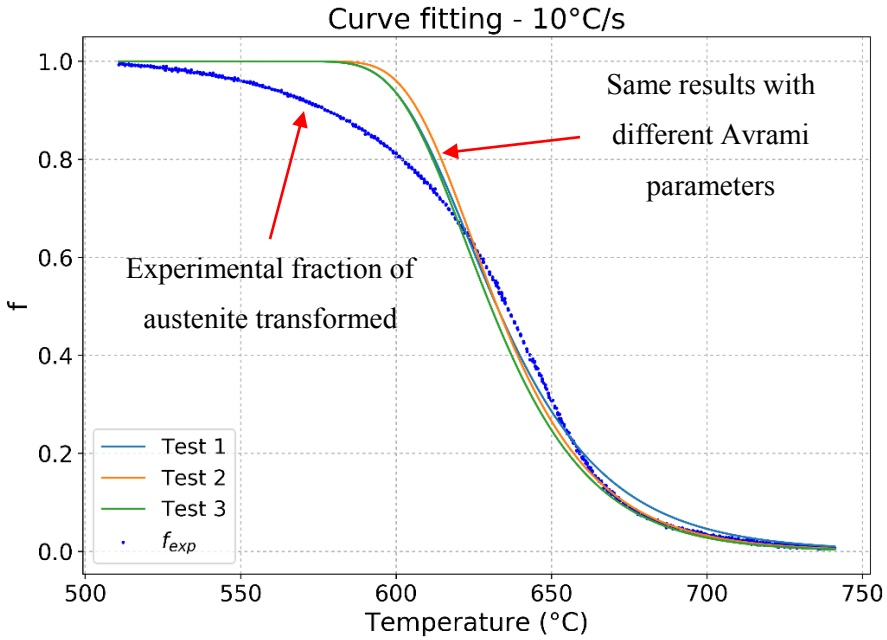


*Figure 4- 5: Curve fitting results with three different set of Avrami parameters.*

### 4.3.2. Modified form of the Avrami equation

In order to improve the curve fitting algorithm and to more easily manipulate the Avrami equation, the equation is modified. Modification is used as a form of the equation that allows easier identification of the three parameters n, Q and $\tau_0$ is wanted. Additionally, the expression also needs to depend only on either time or temperature. As constant cooling rates are only considered, both time and temperature are linked:

$$t = \frac{T_0 - T}{CR} \tag{4.15}$$

Where CR is the cooling rate and $T_0$ is the temperature at which the cooling has started (t=0). To transform the Avrami equation, the following inverse function is used:

$$f^{-1} = ln\big(-ln(1-f)\big) \tag{4.16}$$

Combining Equations 4.1, 4.2 and 4.3, the modified form of the Avrami equation is obtained:

$$f^{-1} = nln\left(\frac{T_0 - T}{CR}\right) - nln(\tau_0) + \frac{nQ}{RT} \tag{4.17}$$

Unfortunately, in the modified expression of the Avrami equation, $f^{-1}$ depends on both the logarithm and the inverse of T, making it not fully linear. Due to the fact that the weight of both these terms is equivalent over the entire range of temperatures, it is therefore impossible to find the parameters n or Q by simply plotting $f^{-1}$ with $ln\left(\frac{T-T_0}{CR}\right)$ or $\frac{1}{RT}$ (both these plots do not show a single line and are presented in Appendix E). Since no regression of $f^{-1}$ can be done, to facilitate the analysis, $f^{-1}$ is directly plotted with the temperature, as shown in Figure 4-6.

Additionally, plotting the modified form of the Avrami equation with the temperature shows an unexpected fact: while a single linear portion was expected, two branches can clearly be seen on the plots. These two branches can therefore correspond to the formation of two distinct structures.

The structure formations are usually predicted using a CCT diagram, like the one presented in Figure 4-7. Regrettably, the limit of the different structure domains are usually not clearly defined (such as the ferrite and bainite domains). Where these traditional CCT diagrams only show the beginning and the end of the transformation of the austenite, the modified form of the Avrami equation in Figure 4-6, clearly shows two branches that can corresponds to two different structures.

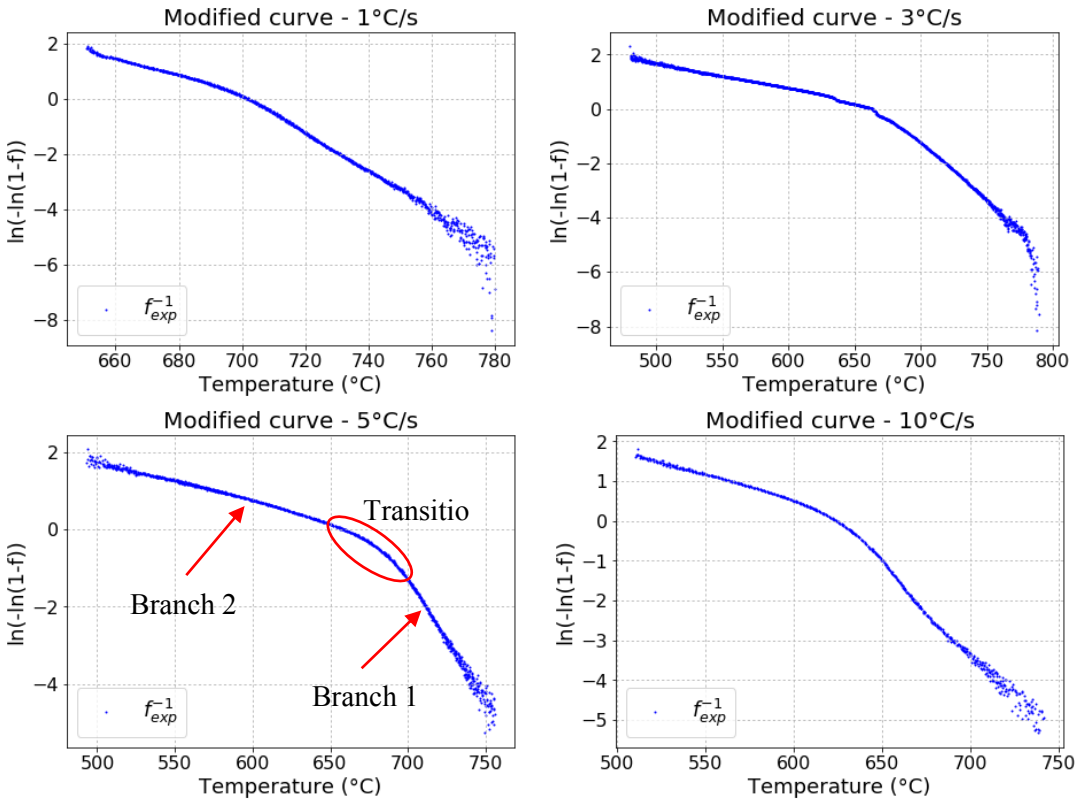


*Figure 4- 6: Modified form of the fraction transformed of austenite for 1, 3, 5 and 10°C/s.*

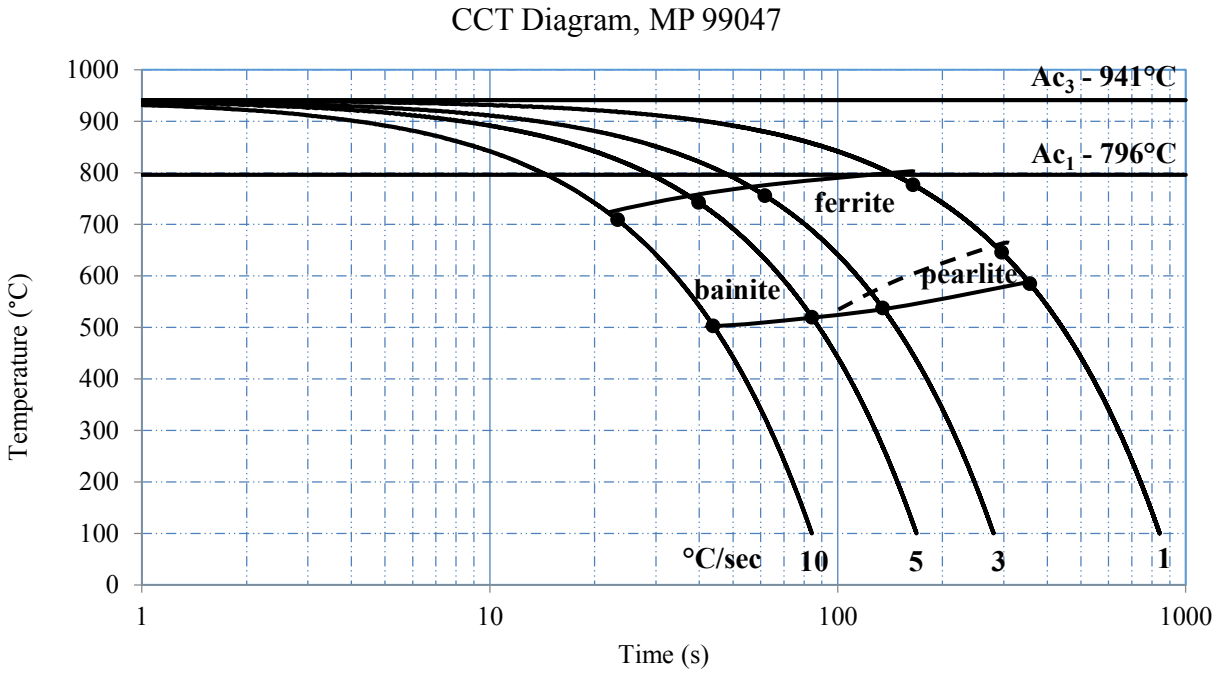


*Figure 4- 7: CCT Diagram of the X70 steel used in the ROT (Evraz).*

The large rebound in the dilation curves (shown in Figure 4-1) can therefore be the result of the simultaneous formation of two different structures. Consequently, the modified form of the Avrami equation shows the formation of multiple structures simultaneously, where it might be undetected otherwise in typical CCT diagrams. Therefore, for the remainder of this thesis, it is assumed that each branch (i.e. branch 1 or branch 2) on the modified form of the fraction transformed corresponds to the formation of one distinct structure. A crucial assumption that the rest of this model relies on. Additionally, the other dilatation curves (from the other datasets from Evraz and Canmet) tend to validate this assumption since they also show several branches using the same analysis.

For every cooling rate, two branches can be seen in Figure 4-6. The structure associated with the high-temperature branch will be called structure 1, while the one at lower temperatures will be known as structure 2. It will be shown later in this thesis that structure 1 and structure 2 correspond to ferrite and bainite, respectively. To facilitate the analysis, these two different branches are now fitted separately. Again though, the curve fitting algorithm faces the same issue as before. Several good fits can be found, leading to no unique solution. It appears that the algorithm is strongly dependent on the initial guess of the parameters due to the presence of the parameter Q in the term $\frac{nQ}{RT}$ in Equation 4.4. No matter the Q value chosen initially, the algorithm will almost always find a set of parameters n and $\tau_0$ that will fit the line.

Since the curve fitting algorithms do not give a unique triplet of parameters, another approach must be pursued.

### 4.3.3. Analytical solution of the problem

To overcome the problem of not finding a single triplet of Avrami parameters, an analytical approach has been developed. In the previous section, a pre-existing curve fitting algorithm was used on the modified curves, but no unique solution were found. In this section the curve fitting algorithm will be developed analytically to determine if it is possible to find a unique solution to the problem. Thus, a mathematical analysis of the least-squares problem, mentioned above, is developed in Appendix F and the main results are presented as follow:

The variables $y_i, x_i$ and $z_i$ are introduced such as:

$$\begin{cases} y_i = ln\left(-ln(1-f_i)\right) \\ x_i = ln\left(\dfrac{T_0 - T_i}{CR}\right) \\ z_i = \dfrac{1}{RT_i} \end{cases} \tag{4.18}$$

Where f is the experimental value of the fraction of austenite transformed, $T_0$ the temperature at which continuous cooling has started (t=0), CR the cooling rate and R the gas constant. The resolution of the least-squares problem results in three equations for n, $\tau_0$ and Q.

$$n = \frac{cov(y, Qz + x)}{var(Qz + x)} \tag{4.19}$$

$$\tau_0 = exp\left(Q\bar{z} + \bar{x} - \frac{\bar{y}}{n}\right) \tag{4.20}$$

$$\begin{aligned} \big(cov(y,z) - cov(y,x)\big)var(z)Q^2 + (cov(x,z)cov(y,z) - cov(y,x)var(z))Q \\ + (cov(y,z)var(x) - cov(y,x)cov(x,z)) = 0 \end{aligned} \tag{4.21}$$

Where $\bar{y}$, $\bar{x}$ and $\bar{z}$ are the mean value of y, x and z over the whole range of data; and cov and var are the covariance and variance respectively:

$$\begin{cases} cov(x,y) = \dfrac{1}{m}\displaystyle\sum_{i=1}^{m}(x_i - \bar{x})(y_i - \bar{y}) = \overline{xy} - \bar{x}\bar{y} \\ var(x) = cov(x,x) \end{cases} \tag{4.22}$$

The expressions of n and $\tau_0$ in Equation 4.6 and 4.7 both depend on Q, whereas no analytical solution has been found for Q, which verifies a second degree polynomial in Equation 4.8. The x, y and z values are all experimental, as shown Equation 4.5, since they depend on the values of T or f. Thus, if these expressions are subbed into Equation 4.8 to calculate the discriminant, a negative value is obtained. This means that there is no solution for Q in this equation.

This corroborates the observation made in Section 4.3.2, because for any Q value it is possible to find a value for n and $\tau_0$ that minimize the squared loss function. The consequence of this observation is quite important since it means that there is no unique triplet of parameters that will fit the experimental value.

One Q value has to be chosen for each structure, since a solution can be found for any Q. The CCT diagram in Figure 4-7 shows that the two structures that are formed are ferrite and bainite (this will be confirmed later in this thesis). According to Kang et al. [26], a common value of the activation energy for the transformation of austenite to ferrite is 200kJ, whereas for the transformation to bainite is driven by

the carbon diffusion and the activation energy is approximately equal to 80kJ. Now that the Q values are chosen, the parameters n, and $\tau_0$ can be determined using Equations 4.6 and 4.7.

### 4.3.4. Optimization of the Avrami parameters by statistical bootstrap method

The two parameters are calculated for each branch of the experimental data in Figure 4-6. The Bootstrap method [27] was chosen to minimize the numerical error introduced by the scattered aspect of the data, on calculation of the parameters n and $\tau_0$. This statistical method consists in creating random samples with different sizes from the original dataset, and then calculate the two parameters with these samples. Thus, the calculation is made a large number of time (i.e. arbitrarily 20000 times in this thesis), which results in the distributions of the two parameters value, presented in Figure 4.8. The value of the parameters n and $\tau_0$ for each branch are identified as the mean value of these distributions.

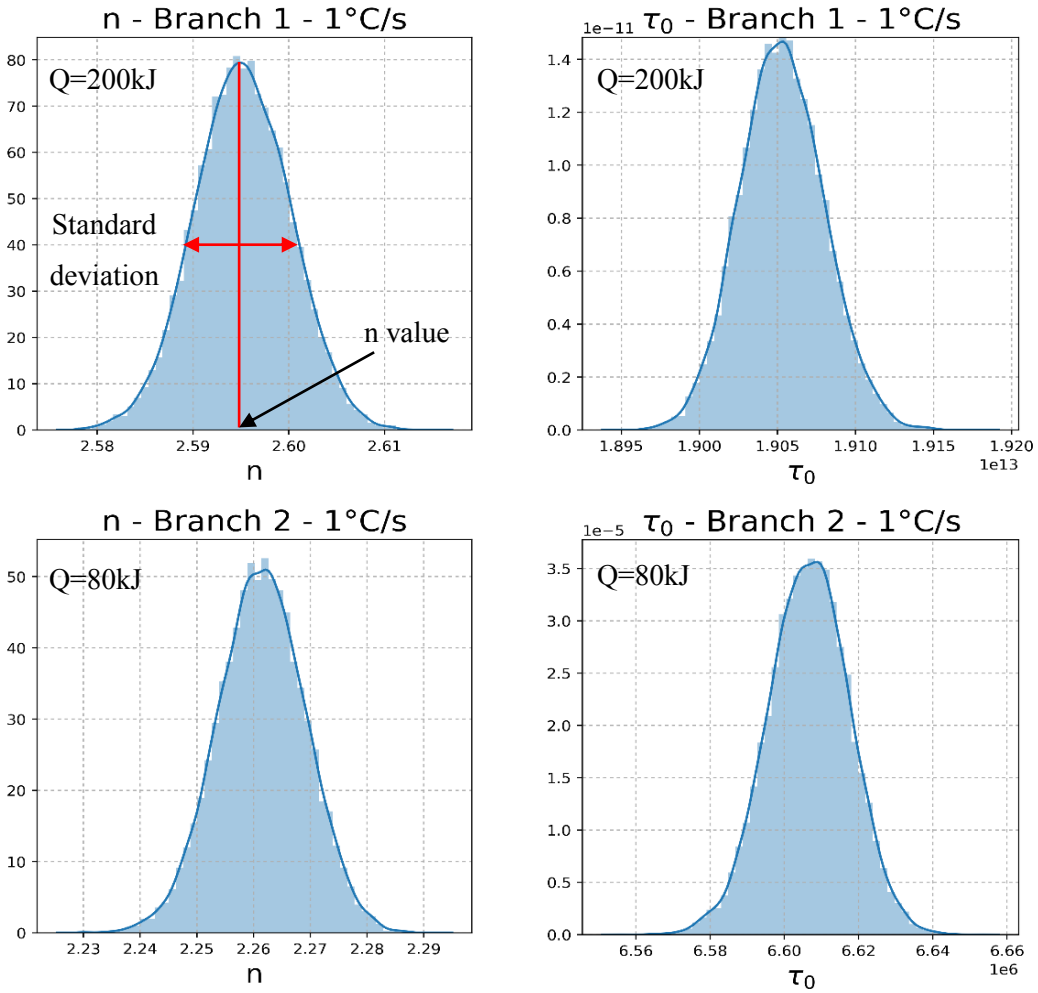


*Figure 4- 8: Distribution of the Avrami parameters obtained with the bootstrap method for 1°C/s.*

The benefit of this method is that it robustly removes the influence of the outliers by calculating the parameters on a large number of data samples with different sizes. The incertitude on the measurement is determined by looking at the standard deviation of the distribution and is less than 0.5% for every cooling rates, which is relatively accurate.

Another source of error can come from the modified curves. Despite all the advantages of the Bootstrap method, there are two parts of the modified curves that might not be relevant for the calculation of the Avrami parameters due to the experimental nature of the data. Indeed $f^{-1}$ is given by Equation 4.3, and it is well defined because the f values are between 0 and 1 (excluded). However, if f is close to 0 or 1 then the modified function will tend to diverge, as shown in Figure 4-9. This effect is also strengthened by the scattered aspect of the experimental data that might not precisely follow the theoretical formula. These two scattered regions can affect the Bootstrap method, and thus, to minimize this impact, the tails of the modified curves must be removed.

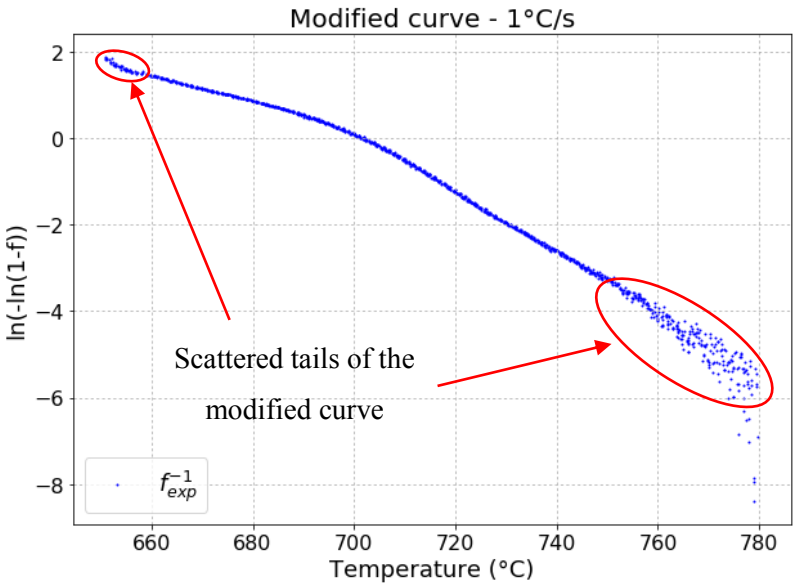


*Figure 4- 9: Modified form of the fraction of austenite transformed for 1°C/s.*

### 4.3.5. Results of curve fitting

Figure 4-10 shows the different parameters n and $\tau_0$ calculated with the bootstrap method for different cooling rates. The $\tau_0$ for the two branches are not presented on the same graph, since they do not have the same order of magnitude. The literature [19-31] cites that n must be between 0 and 4, which is the case for the four different cooling rates. It also appears that there is no trend in these parameters that will allow an extrapolation of n or $\tau_0$ for any given cooling rate, as shown in Figure 4-10 and in Appendix G. The

fact that it is not possible to reasonably guess the Avrami parameters for any cooling rate will affect the thermo-metallurgical model developed later in Chapter 5.

With the two triplets of Avrami parameters found for each branch of the modified curve (Figure 4-6), the fraction of austenite transformed is fitted with two curves, as presented in Figure 4-11. The two curves $f_1$ and $f_2$ (in Figure 4-11), predicted by the bootstrap method, are simply a tool to fit the experimental fraction transformed curve, and do not give the evolution of the volume fractions of structure 1 and structure 2.

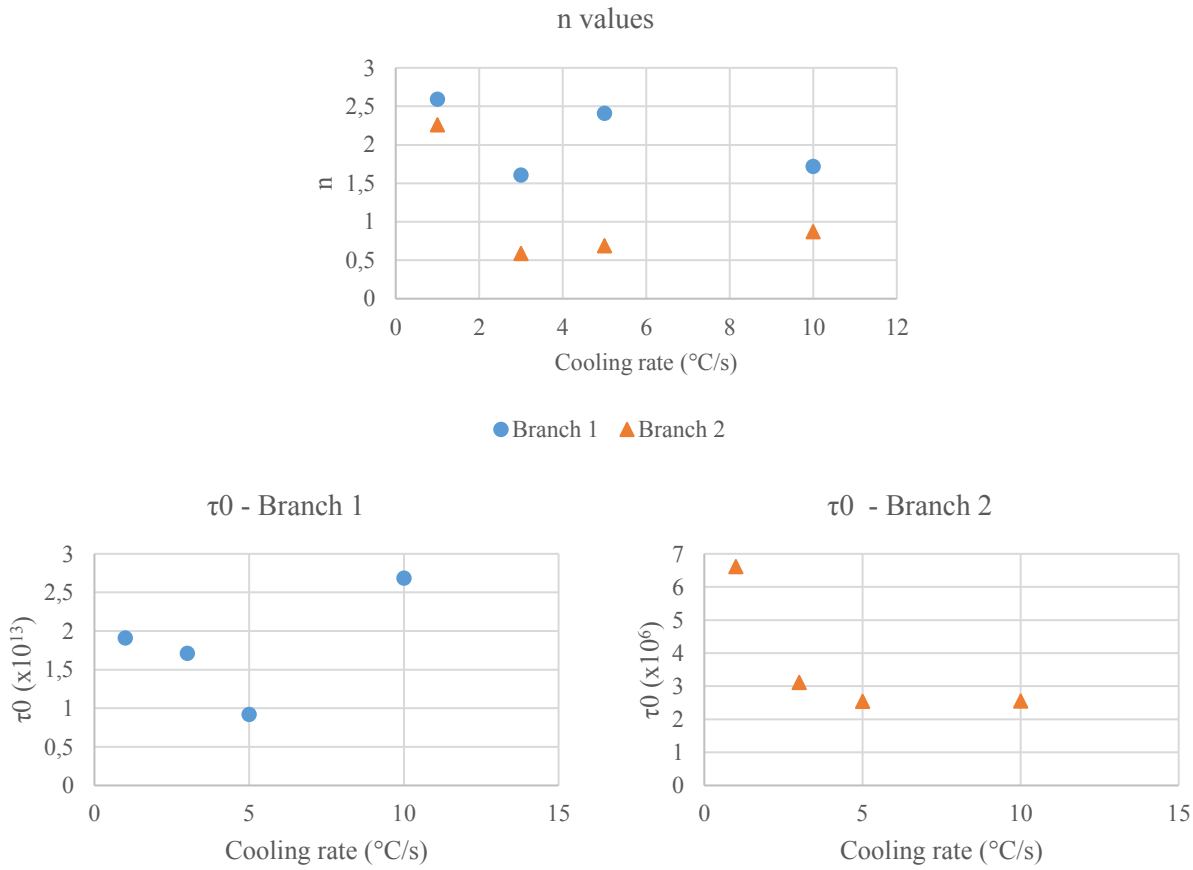


*Figure 4- 10: Avrami parameters found for the two branches of the modified curve depending on the cooling rate.*

It has been shown in this section that the curve fitting technique used in the literature is unable to fit the entire fraction transformed curve obtained with the lever rule. However, this method is able to accurately fit each branch of the modified form of the Avrami equation. The next step of the model is now

to combine the two curves $f_1$ and $f_2$ to have a single curve that fits accurately the experimental fraction of austenite transformed curve in Figure 4-11.

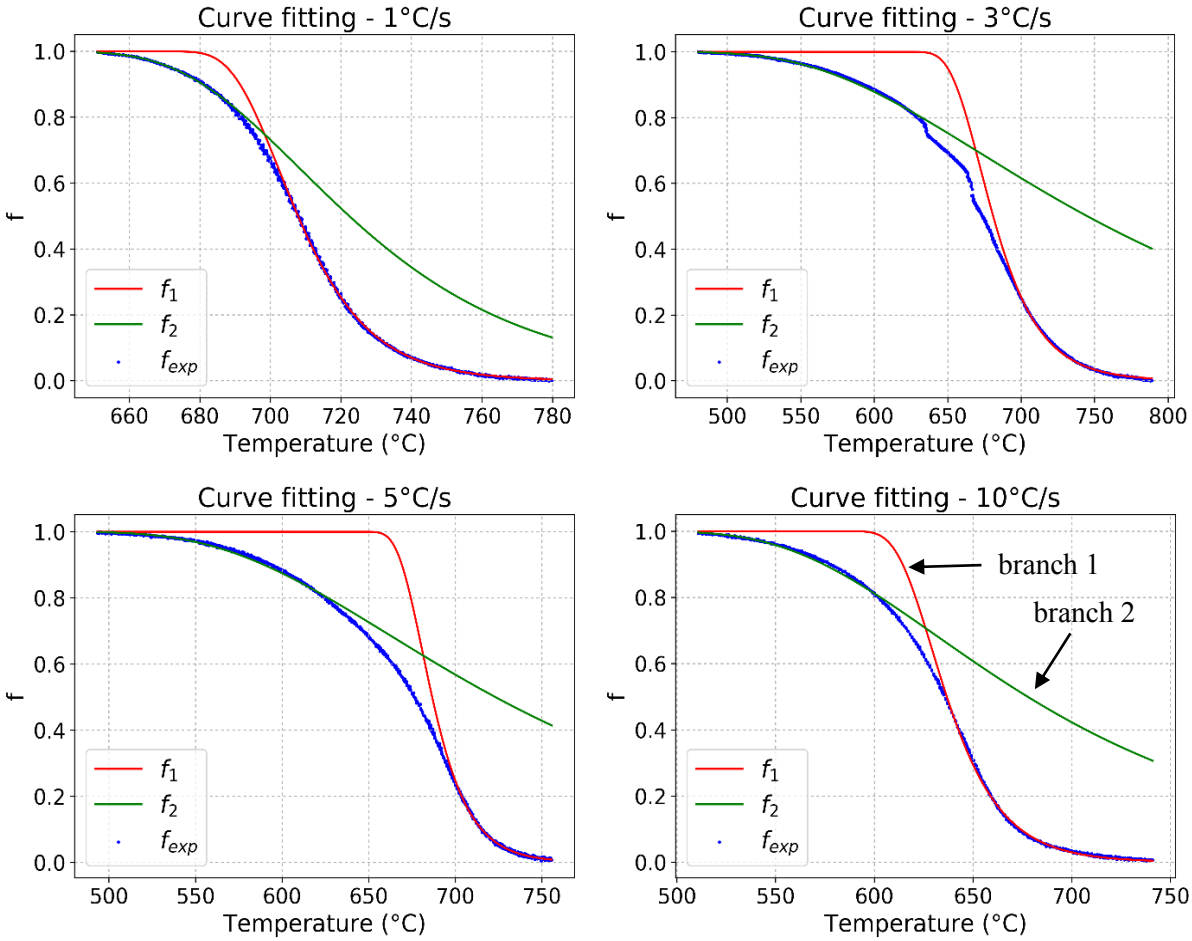


*Figure 4- 11: Curve fitting of the fraction transformed data for 1, 3, 5, and 10°C/s.*

## 4.4. Determination of the volume fractions

A new approach developed in this work and based on the derivation of the modified form of the Avrami equation, will be introduced, in order to predict the evolution of the volume fractions of every structure during the transformation. This technique characterizes the simultaneous formation of the structures 1 and 2 during continuous cooling. The results will then be compared to the experimental fraction of austenite transformed, which was determined with the lever rule in Section 4.2.2.

### 4.4.1. Derivation of the modified curve

In the literature, the structure transformations are treated sequentially. It is assumed that only one structure is formed at a time. However, looking at Figures 4-6 and 4-12, it appears that there is a region

where two structures are formed at the same time. This can be seen on the modified curve of the fraction transformed, where the experimental curves goes from one branch to the other.

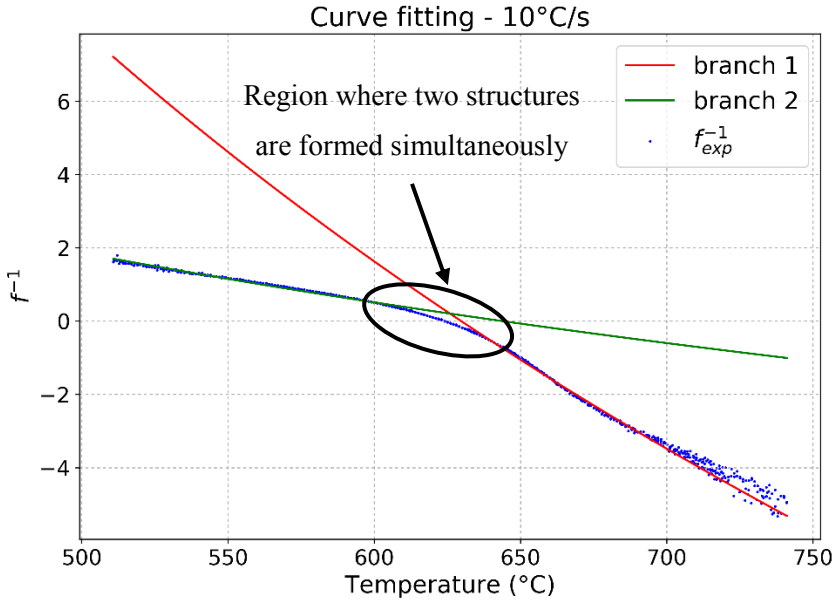


*Figure 4- 12: Curve fitting of the modified form of the fraction transformed.*

After a closer look at the modified curves, it appears that in the region where both structures are formed, the slope of the experimental curve appears to be between the slopes of $f_1$ and $f_2$. Due to the scattered aspect of the modified curve, it has to be smoothed in order to be able to take the numerical derivative. The slope s of each curve has then been obtained using a finite difference formula on the smoothed curve:

$$s = \frac{f_{i+1} - f_i}{T_{i+1} - T_i} \tag{4.23}$$

Where f is the fraction of austenite transformed and T the temperature. This numerical approach can be done because the interval between two consecutive points is always less than 1°C, which is small compared to the range of temperature and the total number of data points. The slopes of the modified fraction transformed curve and the two branches are presented for each cooling rate in Figure 4-13 (these curves are explained in more detail in Appendix H).

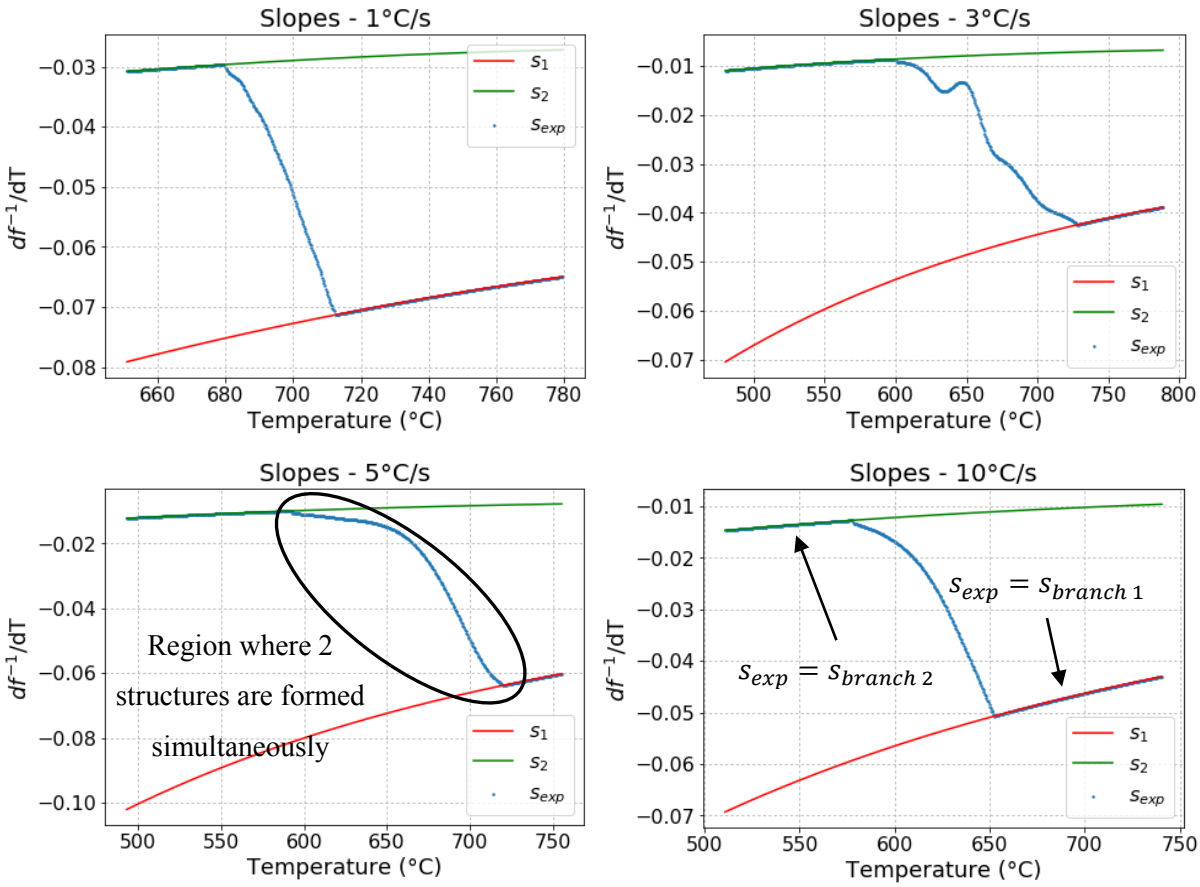


*Figure 4- 13: Slopes of the modified curves for different cooling rates.*

Now the region where both structures are forming simultaneously will be addressed. Since the slope of the experimental curve varies between the slopes of the two branches, we can combine the slopes of the two branches to obtain the modified experimental one at any temperature. Thus, the parameter α is created. This parameter characterizes the fractional contribution of each slope for any given temperature in the temperature range where both structures are present. So the parameter α is defined such as:

$$s(T) = \alpha(T)s_1(T) + \big(1 - \alpha(T)\big)s_2(T) \tag{4.24}$$

Where $s_1$ and $s_2$ are the slopes of the two branches at any temperature, and s is the modified experimental slope. The modified experimental slope is expressed as a combination of the slopes of the two branches. Thus α represents the weight of the slope of the first branch. In the temperature range where the two structures are forming, α is calculated using this formula:

$$\alpha(T) = \frac{s(T) - s_2(T)}{s_1(T) - s_2(T)} \tag{4.25}$$

For higher temperatures (where the experimental slope is equal to the slope $s_1$ of the first branch), α is equal to 1, which means that only structure 1 is forming. Similarly for lower temperature (where the experimental slopes is equal to the slope $s_2$ of the second branch), α is equal to 0, which means that only structure 2 is forming. The evolution of the different α parameters for each cooling rate is presented Figure 4-14, which illustrates that the behavior of α differs for every cooling rate. Therefore, it appears that it is not possible to extrapolate a particular shape of α that will predict the slope of the modified form of the Avrami equation. This is also the case for the two other steels that have been studied for this thesis.

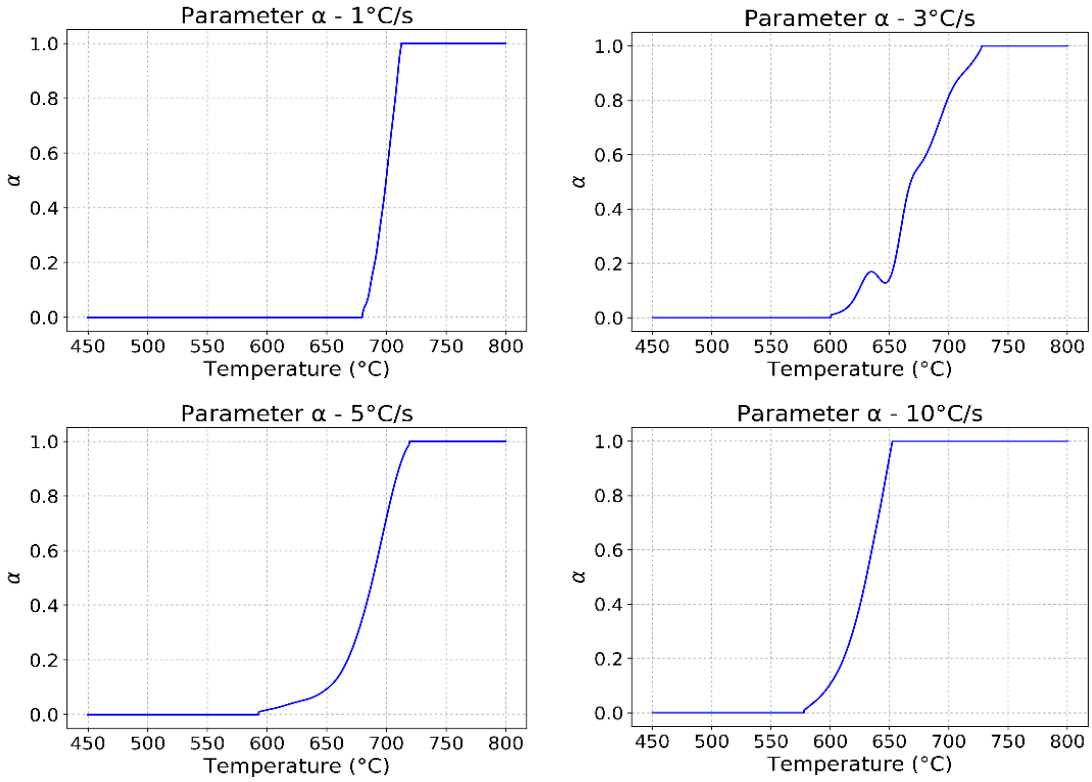


*Figure 4- 14: Evolution of the parameters α with temperature for different cooling rates.*

Now that α is known at every temperature and for every cooling rate, the relative proportion of structure 1 and structure 2 that is formed during the continuous cooling may be determined. The terms $\alpha(T)s_1(T)$ and $\big(1-\alpha(T)\big)s_2(T)$ of Equation 4.11 represents the proportion of the slope of branch 1 and branch 2 in the experimental slope respectively. Thus, each of these terms is numerically integrated using the trapezoidal rule, in order to go back to the modified form of the fraction transformed. The results are presented Figure 4-15, where there are now two theoretical curves that actually corresponds to the modified curve of structure 1 and structure 2 (see Section 4.3.5, where $f_1$ and $f_2$ did not correspond to the evolution of the volume fraction of structure 1 and structure 2). The experimental curves match the curve

associated with structure 1 for higher temperatures and the curve associated with structure 2 for lower temperatures. This shows that the introduction of the parameter α did not affect the curve fitting realized in the sections above.

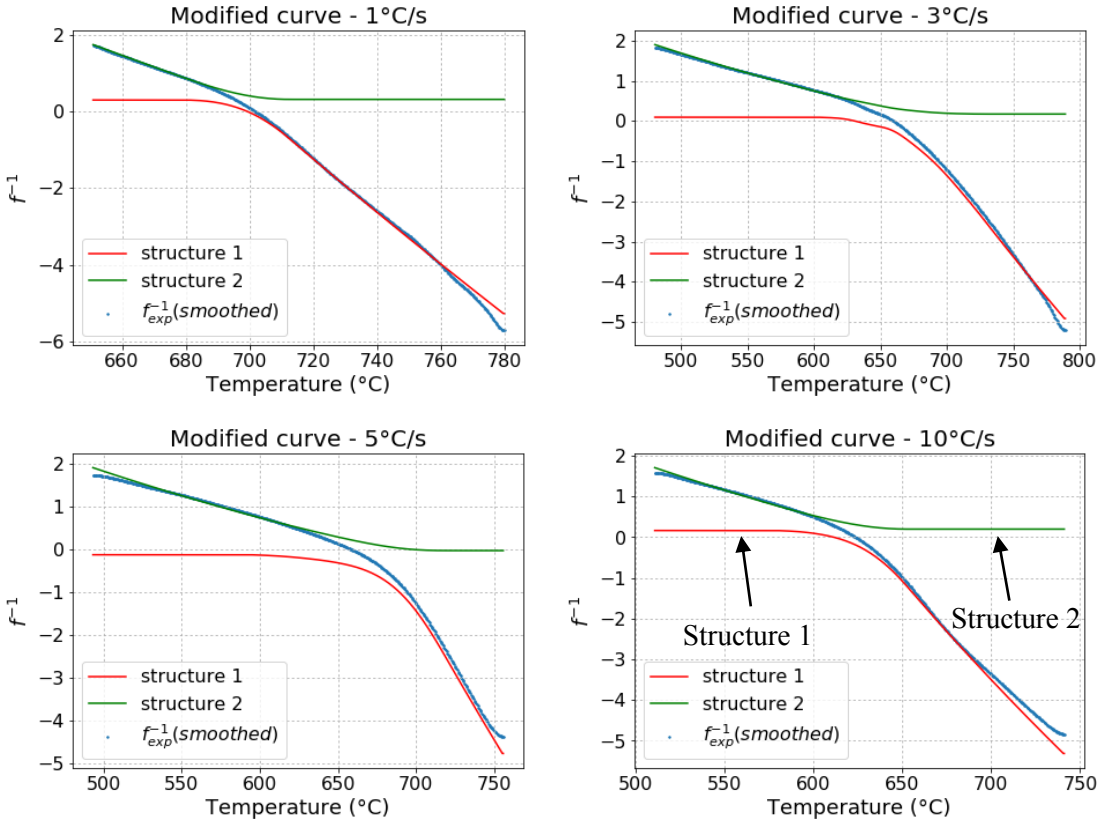


*Figure 4- 15: Modified curve obtained for the formation of structure 1 and structure 2.*

Lastly, in order to go back to the usual form of the evolution of the fraction transformed, the following function is applied to the two modified theoretical curves associated with structure 1 and structure 2 in Figure 4-15:

$$f = 1 - exp\left(-exp(f^{-1})\right) \tag{4.26}$$

The parameter α has been created in order to fit the slope of the modified form of the Avrami equation in the simultaneous structure transformation region. However, working with the numerical derivative of the modified curve can add some numerical error in the model. This error is difficult to quantify but its impact should not be too important, since the interval between two points of the modified curve is small. The same type of error occurs during the integration step mentioned above.

### 4.4.2. Results of the predicted volume fractions

Figure 4-16 shows the evolution of the proportion of structure 1 and structure 2 that is formed from the amount of austenite being transformed. The theoretical evolution of the transformation of austenite is given by the sum of the structure 1 and structure 2 curves. It is assumed that only two structures are formed from the austenite transformation. The curves in Figure 4-16 should therefore fit the curve of the fraction transformed.

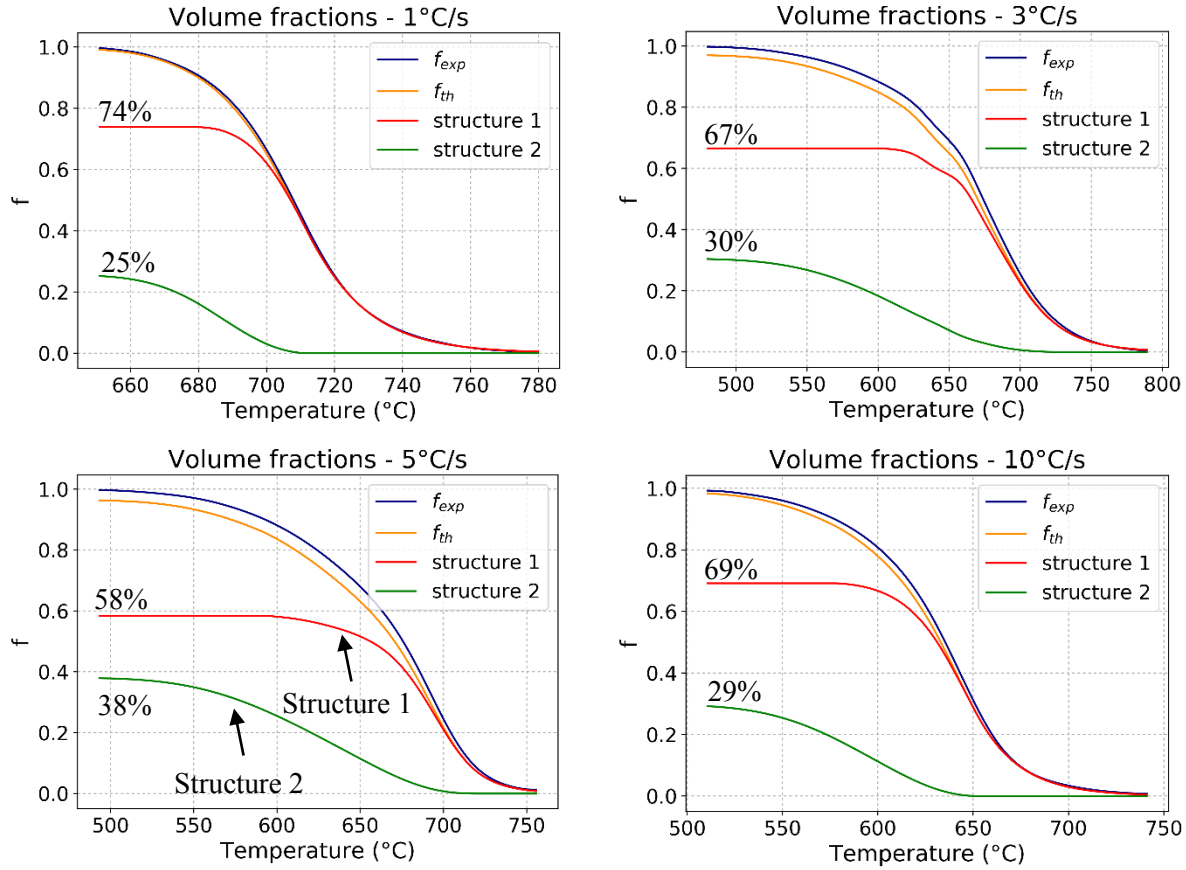


*Figure 4- 16: Evolution of the experimental and predicted fraction transformed and of the volume fraction of structures 1 and 2 with temperature for different cooling rates.*

There is a reasonable agreement between the experimental and the predicted curve for 1 and 10°C/s. For 3 and 5°C/s a difference between these two curves can be observed at the end of the transformation. This gap can be explained by all the numerical error and approximations that the model carries. Another explanation could be the introduction of the parameter α. This parameter has been created artificially, hence there could be a more adequate method. The method used in this thesis was the one which shows the better fit and the most encouraging results. Additionally, the theoretical results provide a reasonable

fit to the experimentally measured curve and difficulty in producing an experimental curve may be the cause of the observed deviations. In the end, the approach developed above seems to be the most appropriate to predict the proportion of structure 1 and structure 2.

## 4.5. Experimental validation of the model

The metallurgical model will be validated by comparing the predicted volume fractions with the ones measured on micrographs provided along with the dilation curves.

### 4.5.1. Volume fraction measurements

The metallurgical model takes as an input the dilation curves for different continuous cooling transformations and outputs the evolution of the transformation of austenite and the volume fractions of the structures formed. Experimentally the only way to have access to this evolution is to quench the sample at various temperatures and to look at the microstructure. This procedure is very complicated and would require multiple repetitions at different temperatures. It is also possible to look at the resulting microstructure at the very end of the transformation because it requires only one observation per cooling rate and it does not need any quenching. From each sample (corresponding to different cooling rate) the volume fraction of each structure can be estimated and then compared to the theoretical values. The theoretical volume fractions can be found on Figure 4-16 at the end of the transformation for each cooling rate.

### 4.5.2. Analysis of the micrographs

As mentioned previously, Evraz provided the dilation curves, and for each cooling rate they also provided one micrograph, presented in Figure 4-17. One micrograph is not enough to effectively quantify the structure fraction of the sample but it gives a good approximation that can be compared with the theoretical values. On all four micrographs we can identify two to three structures. The samples have been etched so as to reveal the ferrite as a light gray/white phase and the bainite as a dark gray/black phase. Looking at the micrographs it appears that the two structures comprised in the samples are ferrite and bainite. Looking at the proportion of ferrite to bainite makes us think that structure 1 is ferrite and structure 2 is bainite. It also appear that some pearlite can be seen on the micrographs for 1 and 3°C/s, as shown in Figure 4-17. However, the formation of pearlite was not considered by the model at this stage.

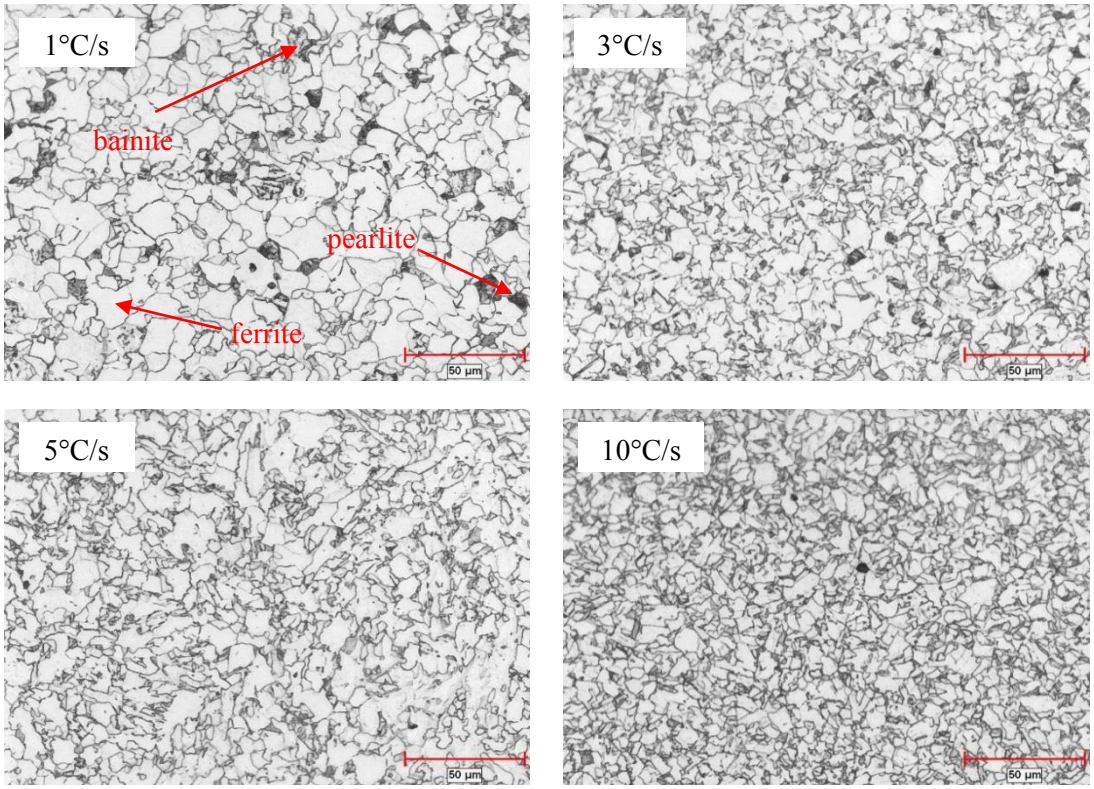


*Figure 4- 17: Micrographs of the dilation samples for different cooling rates.*

### 4.5.3. Digitalization of the micrographs

Matlab R2015b has been used so that the structure fractions on the micrograph can be analyzed more precisely. Each micrograph is converted into a gray scale picture. The gray level of each pixel is then counted. The distribution of the gray level of each micrograph is showed in Figure 4-18. All the distributions seem to show the same trend. They all have a bimodal distribution with one peak in the "white" region and the other one in the "black" region. Thus, a threshold is fixed manually at the minimum between these two peaks for each cooling rates. The position of the threshold is adjusted for each cooling rate. All the pixels below this limit are considered black and are classified as bainite and all above are white and classified as ferrite. The processed pictures are presented in Figure 4-19.

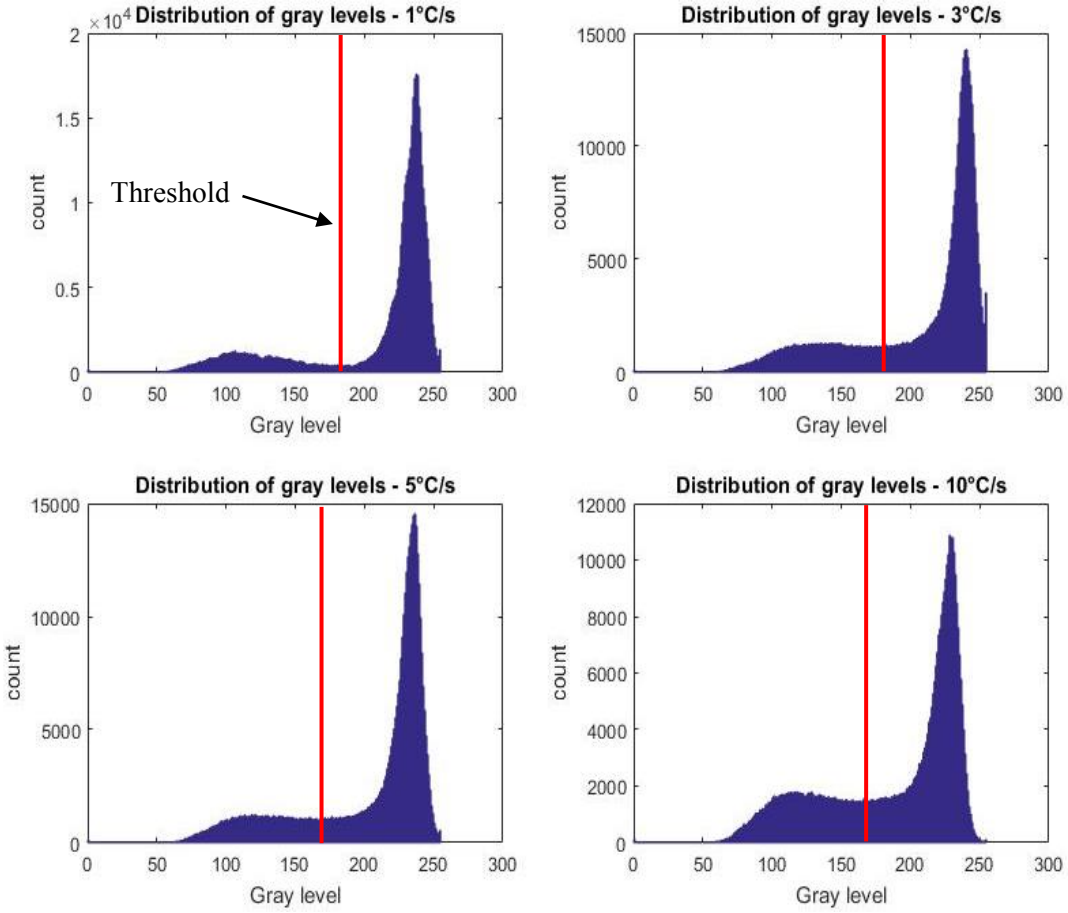


*Figure 4- 18: Distribution of the gray level for the four micrographs.*

The measure of the volume fraction is driven by the position of the threshold, because a slight variation in its position can modify the value of the measured volume fraction. Additionally, the measurement of the volume fraction is only an estimation due to the lack of micrographs. The comparison between the theoretical and experimental volume fraction for each cooling rate is presented in Figure 4-20. The predicted and experimental volume fractions are quite similar. However, even though this comparison is only qualitative it seems that the theoretical model overestimates the amount of bainite for all cooling rates. It also appears that the predicted amount of bainite increases with cooling rate, except for 10°C/s. Figure 4-16 shows that the fit between the experimental and predicted fraction of austenite transformed is better for 1 and 10°C/s than for 3 and 5°C/s. Comparing the predicted and experimental results, it shows that the predicted volume fractions are more accurate for 1 and 10°C/s. Thus, it appears that a good fit between the predicted and experimental fraction transformed (Figure 4-16) results in an accurate volume fraction prediction at the end of continuous cooling.

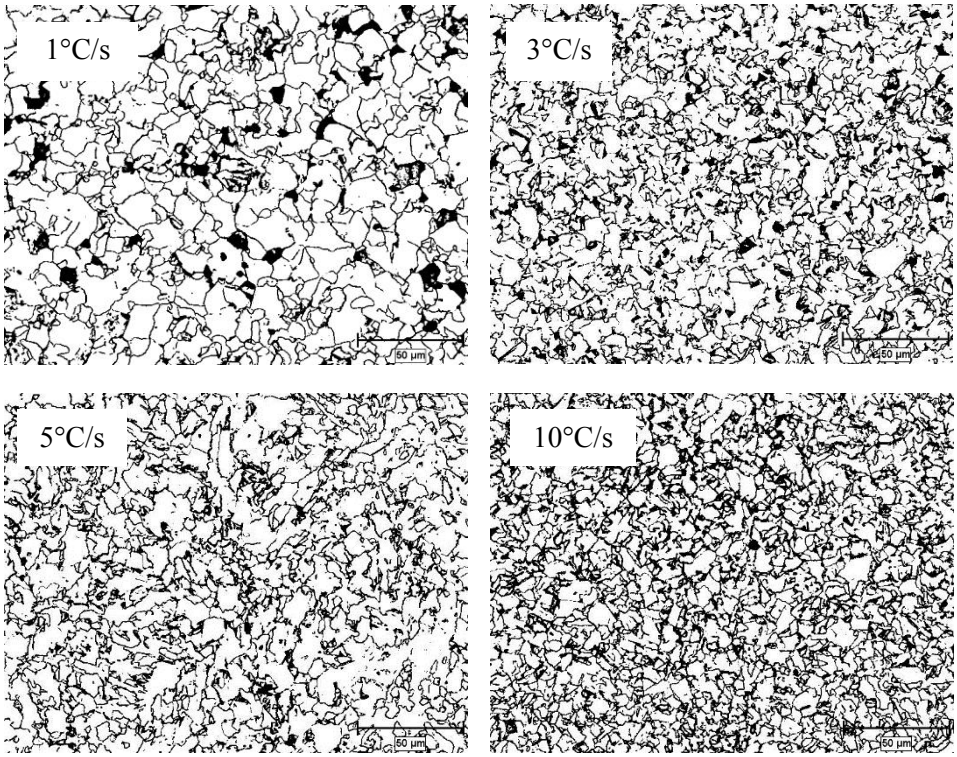


*Figure 4- 19: Processed micrographs for each cooling rates.*

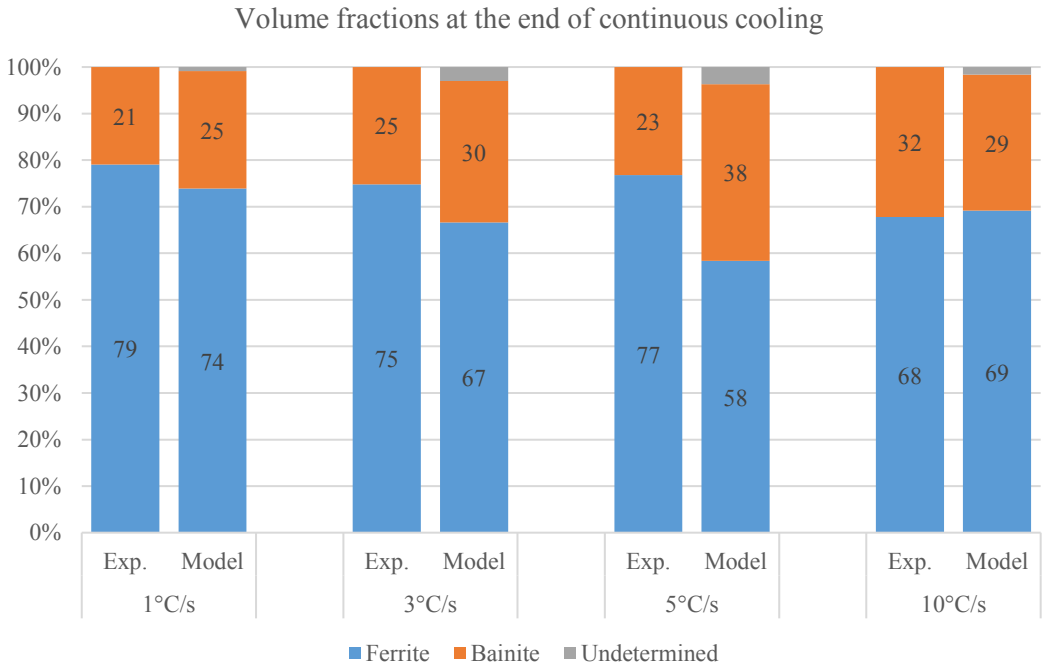


*Figure 4- 20: Comparison between the experimental and predicted volume fraction at the end of four different continuous cooling.*

The theoretical model gives a good approximation of the evolution of the volume fraction of each structure. However, the experimental validation has only been made with one micrograph due to the lack of data. Additionally, the theoretical model's evolution of ferrite and bainite volume fractions during continuous cooling cannot be validated, because only the experimental volume fractions at the end of the transformation are available.

## 4.6. CCT diagrams

Phase transformations during continuous cooling are commonly characterized using CCT diagrams. The structure transformation in those diagrams are sequential. It means that the structures form only one after the other. It has been demonstrated that there is a region where the two structures form at the same time. Thus, a new CCT diagram can be built to take into account this observation.

Since the transformation of austenite into two different structures is considered, four transformation temperatures needs to be determined: $T_1$(start), $T_2$(start), $T_1$(stop) and $T_2$(stop). They correspond to the start and finish temperatures of the formation of structure 1 and structure 2. At the beginning of the transformation only structure 1 is forming and at the end it is only structure 2. So $T_1$(start) and $T_2$(stop) correspond to the beginning and the end of the transformation of austenite respectively. Next we need to identify $T_2$(start) and $T_1$(stop) that correspond to the temperatures where structure 2 starts forming and where structure 1 stops forming respectively. These two temperatures define the region where both structures are forming simultaneously.

The first two temperatures $T_1$(start) and $T_2$(stop) can be identified on the fraction transformed diagram. If the transformation is considered to occur when the fraction transformed is between 1 and 99%, then the two temperatures can be determined as presented in Figure 4-21. These threshold values are commonly used to build CCT diagrams. The identification of these temperatures is very sensitive to the position of the tangents on the dilation curve.

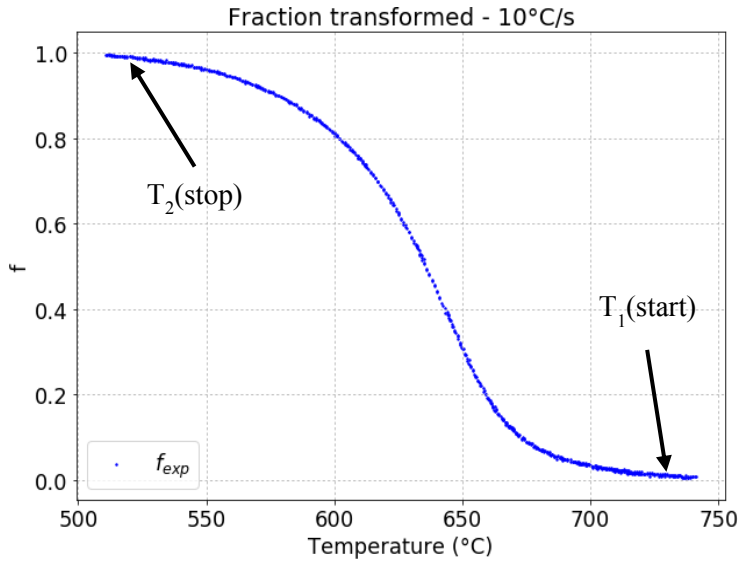


*Figure 4- 21: Identification of the transformation temperatures on the fraction transformed curve for 1°C/s.*

The two temperatures $T_2$(start) and $T_1$(stop) can be determined in Figure 4-22 by looking at the slopes of the modified curve and the two branches, when the experimental slope is equal to the slope of one of the other branch. This technique is quite accurate because it identifies the exact moment when the experimental curve drifts from the branches. However, it also can overestimate the temperatures because it strongly depends on the accuracy of the experimental data. A small instability on the modified experimental data has a pronounced impact when looking at its derivative and can then distort the results.

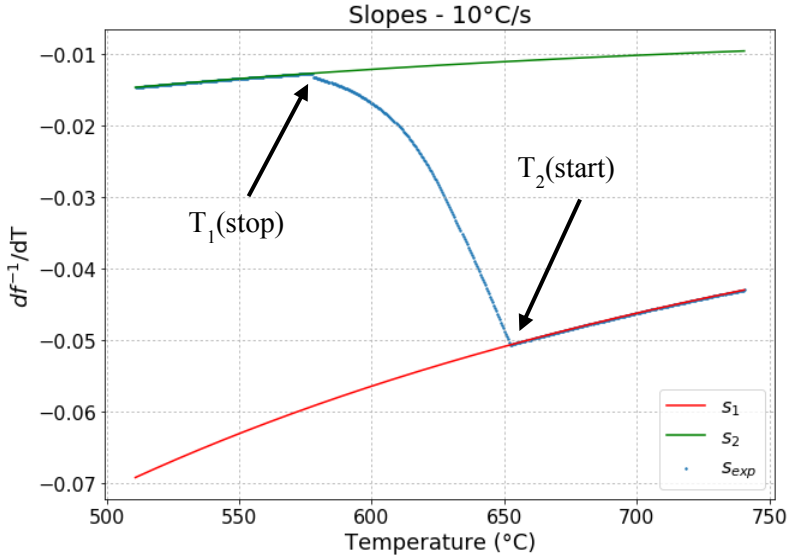


*Figure 4- 22: Identification of the transformation temperatures on the slopes curve for 1°C/s.*

Figures 4-23 shows the comparison between the CCT diagram from Evraz (also based on the dilation curve) and the predicted CCT diagram using the transformation temperatures determined above. These two CCT diagrams are fairly close in terms of identification of the transformation of austenite beginning and finish temperatures. The benefit of this new approach is that it gives more precise information on the domains where the structures are forming. For a cooling rate of 1°C/s the "pearlite" domain is obtained by looking at the second rebound that was identified on the dilation curve in Figure 4-3. Since this rebound is clearly after the first one, it shows that the formation of this third structure (identified as pearlite by Evraz) starts after the transformation of the two previous structures.

On the CCT diagram, the structure 3 domains corresponds to the formation of a third structure due to the presence of a second rebound on the dilation curve for 1°C/s (as shown in Figure 4-3). Since the two rebounds are not in the same temperature range, it shows that the formation of this third structure (identified as pearlite by Evraz) starts after the transformation of the two previous structures (i.e. the formation of structure 3 and the formation of structures 1 and 2 are not simultaneous).

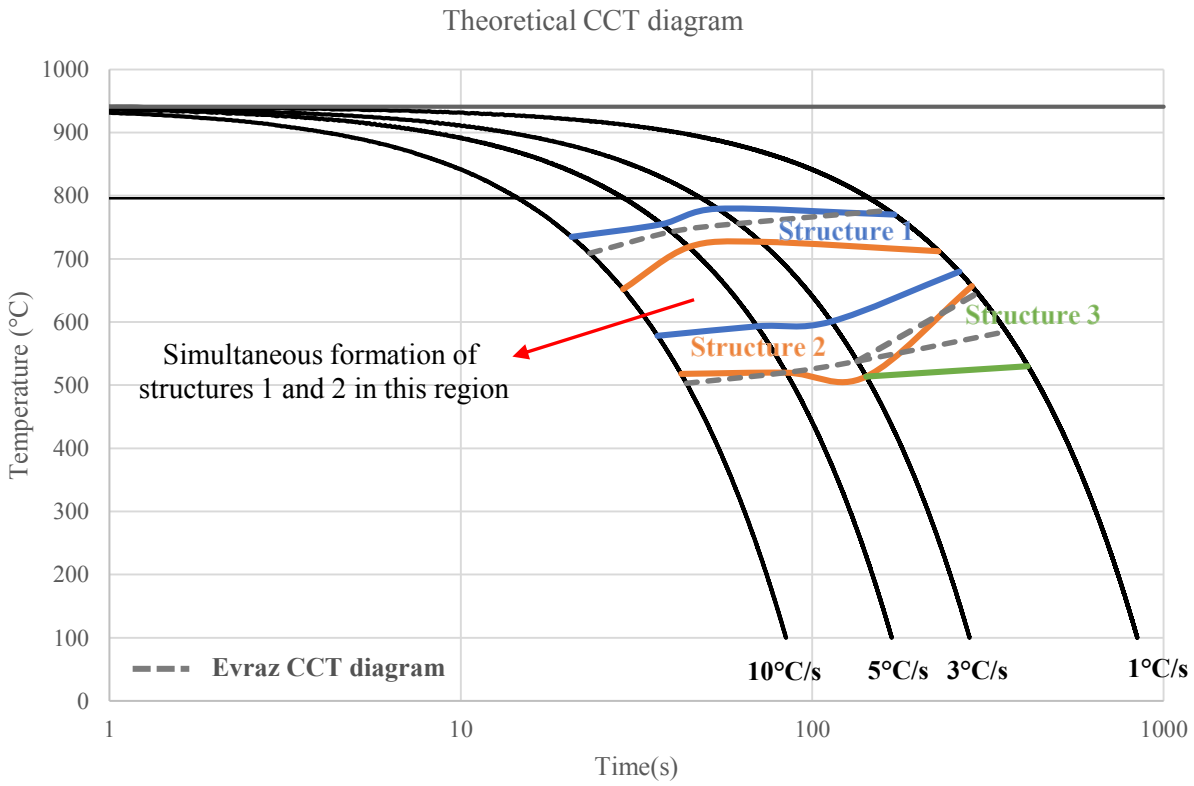


*Figure 4- 23: Comparison between the predicted and Evraz CCT diagram.*

## 4.6. Other steels

To try to validate the model, two other steels and dilation curves were tested. The data for the first steel was also provided by Evraz and the second one by Canmet. In this section, only the major results will be presented (the intermediary results are presented in Appendix I).

### 4.6.1. Evraz X70-B

#### *4.6.1.1. Steel composition*

A partial chemical composition of this X70 steel is presented in Table 4-3. The composition is different from the one used in the run-out table (Table 4-3). The Mn content is the similar, but the Cr, Mo and Nb contents are different. With this other composition, it will be assessed if the model is consistent with a change in the steel composition.

*Table 4- 3: Comparison of the steel composition between two X70 steels.*

| | C | Mn | Cr | Mo | Nb |
|---|---|---|---|---|---|
| **X70 - B** | 0.057 | 1.68 | 0.001 | 0.012 | 0.26 |
| **X70 - 17.3mm - ROT** | 0.043 | 1.67 | 0.09 | 0.192 | 0.067 |

#### *4.6.1.2. Application of the metallurgical model*

The dilation curves associated with this steel are presented in Figure 4-24. The dilation samples were heated up to 1200°C and held at this temperature for 1h15. For 1 and 3°C/s the dilation curves show an unusual behavior at the "rebound". It is as if there was a second rebound inside the first one. First, it will be assumed that it is due to experimental manipulation.

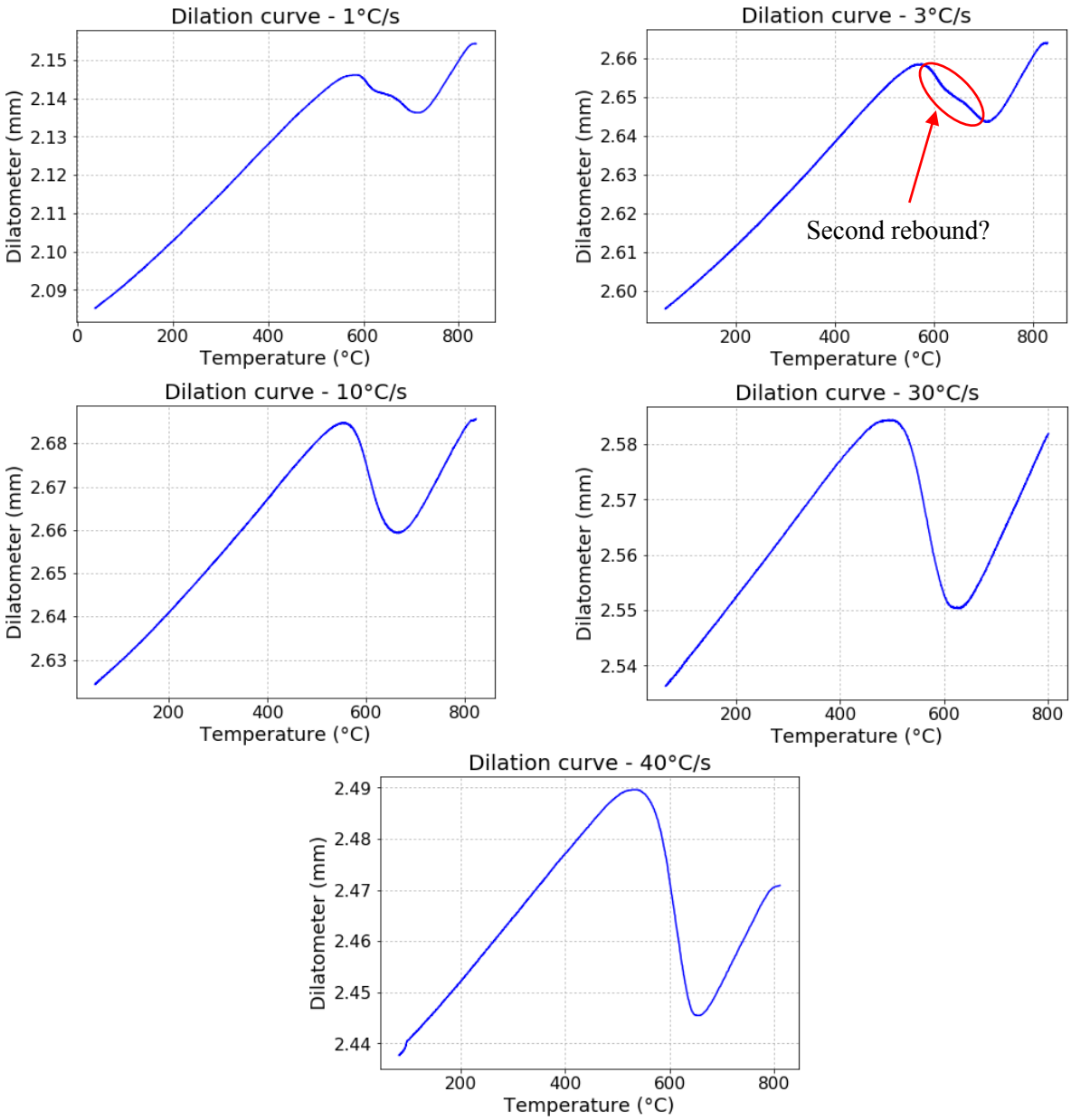


*Figure 4- 24: Dilation curves for the Evraz X70-B steel.*

The lever rule is then applied to five different cooling rates and the transformed austenite fraction curves are presented in Figure 4-25. As expected the experimental inconsistency for 1 and 3°C/s propagates to these curves, and thus, might influence the final results of the metallurgical model.

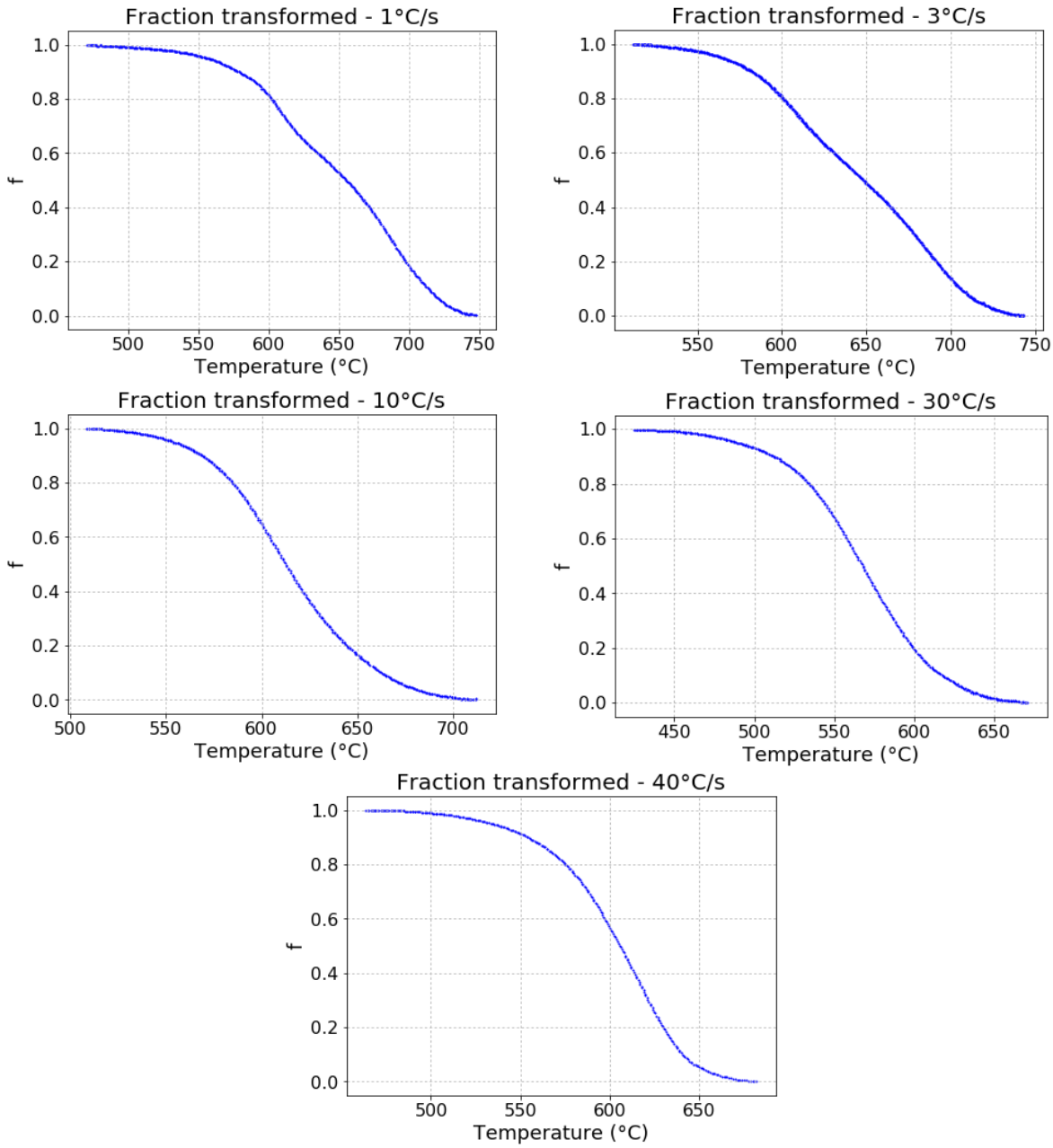


*Figure 4- 25: Evolution of the fraction transformed of austenite for different cooling rates (Evraz X70-B steel).*

Determining the Avrami parameters and introducing a parameter α for each cooling rate, the predicted evolution of the different volume fractions with temperature is presented in Figure 4-26.

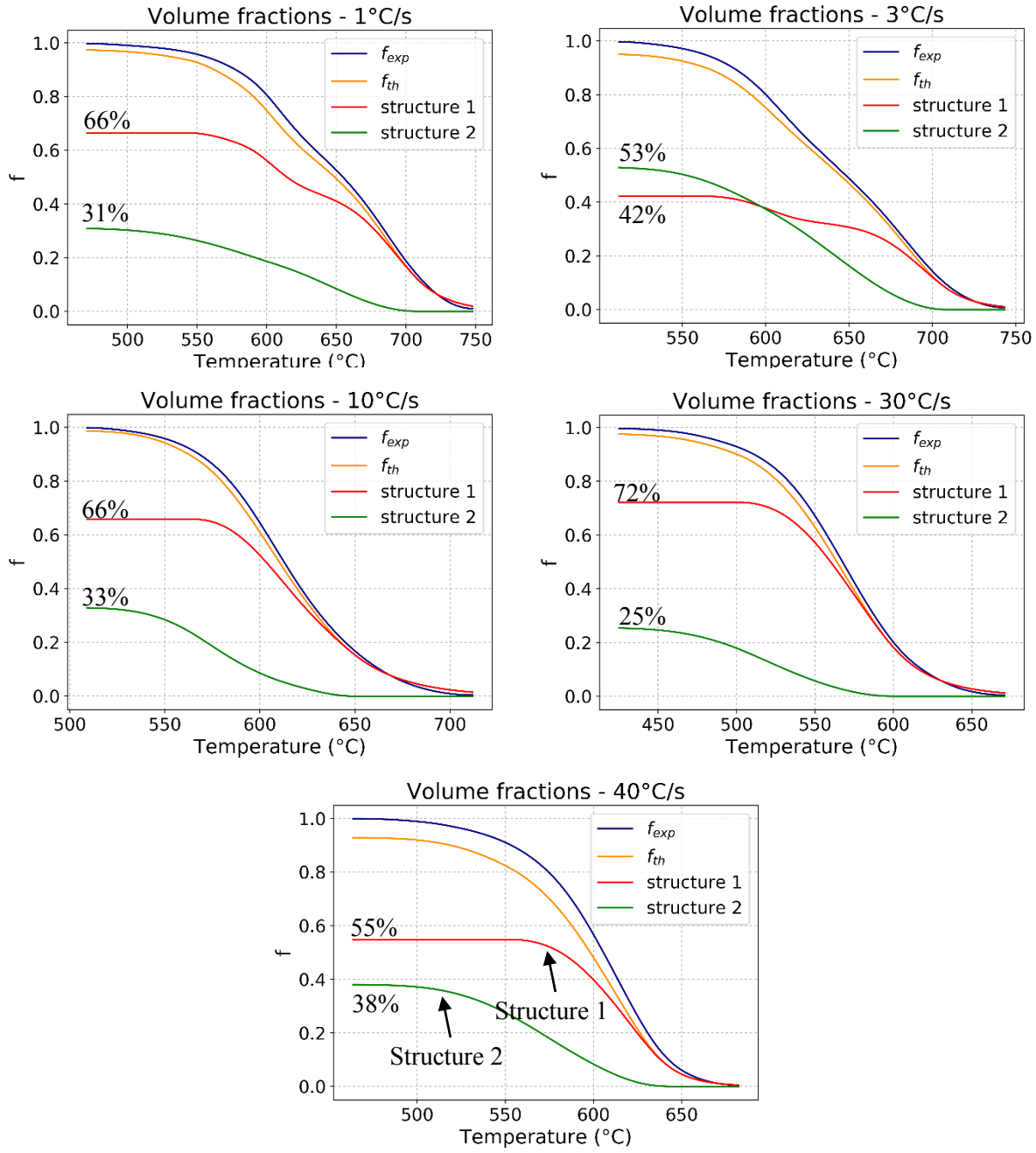


*Figure 4- 26: Evolution of the volume fraction with the temperature for different cooling rates (Evraz X70-B steel).*

Despite a small difference between the experimental and predicted fraction of transformed austenite at the end of the cooling, it appears that the model succeeds in fitting the total experimental fraction transformed curve. Nevertheless, the amount of structure 1 for 40°C/s seems too small compared to the one for 30 and 10°C/s, but it will be confirmed by the microstructure analysis. The model has also

troubles predicting the fraction transformed for 1 and 3°C/s. As mentioned before, the evolution of these dilation curves is unusual and it impacts the final results. The results for these two cooling rates can be questioned particularly by looking at the evolution of structure 1 and structure 2. For both cooling rates, structure 2 starts forming at a higher temperature compared to the previous steel (for the same cooling rates). Additionally, it appears that the structure 1 curve has an unusual second inflexion point between 550 and 650°C, as shown in Figure 4-24. These results can be explained by the error in the dilation curves that propagates throughout the model. This may have occurred due to sample slippage.

Another explanation could be that this second rebound inside the first one corresponds to the formation of a third structure. Looking at the CCT diagram in Figure 4.23, there is a third structure domain (usually associated to pearlite) for 1°C/s located after the formation of structure 1 and 2. This third domain was associated with a second rebound at lower temperature in the dilation curve for the X70-A steel. For the Evraz X70-B steel at 1°C/s, the range of temperature of these two rebounds might overlap, and thus, merge into a single large rebound that contains a smaller one. This could explain the shape of the dilation curve for 1 and 3°C/s.

Looking at the modified curve for 1 and 3°C/s in Figure 4-27 three branches that might correspond to three structures can be seen. The modified curve shows now two regions where two structures are forming simultaneously. A first one that corresponds to the simultaneous formation of structure 1 and structure 2, and a second one for structure 2 and structure 3. Thus, instead of introducing a single parameter α to find the fraction transformed, a second parameter β may be introduced. The slope of the modified curve can then be expressed as follow:

$$s = \alpha s_1 + (1 - \alpha - \beta) s_2 + \beta s_3 \tag{4.27}$$

The sum of the three pre-factors associated with the slopes of branch 1, 2 and 3 still equals 1. The form of this equation comes from the fact that the two regions where austenite turns into two structures simultaneously are clearly separated. For the first region, we have β=0, thus, Equation 4.14 is similar to Equation 4.11. For the second region α=0 and Equation 4.14 also have the same form as the Equation 4.11. Then similarly to Section 4.4.1 the three terms are integrated and then transformed back to the fraction transformed expression. The results are shown in Figure 4-28.

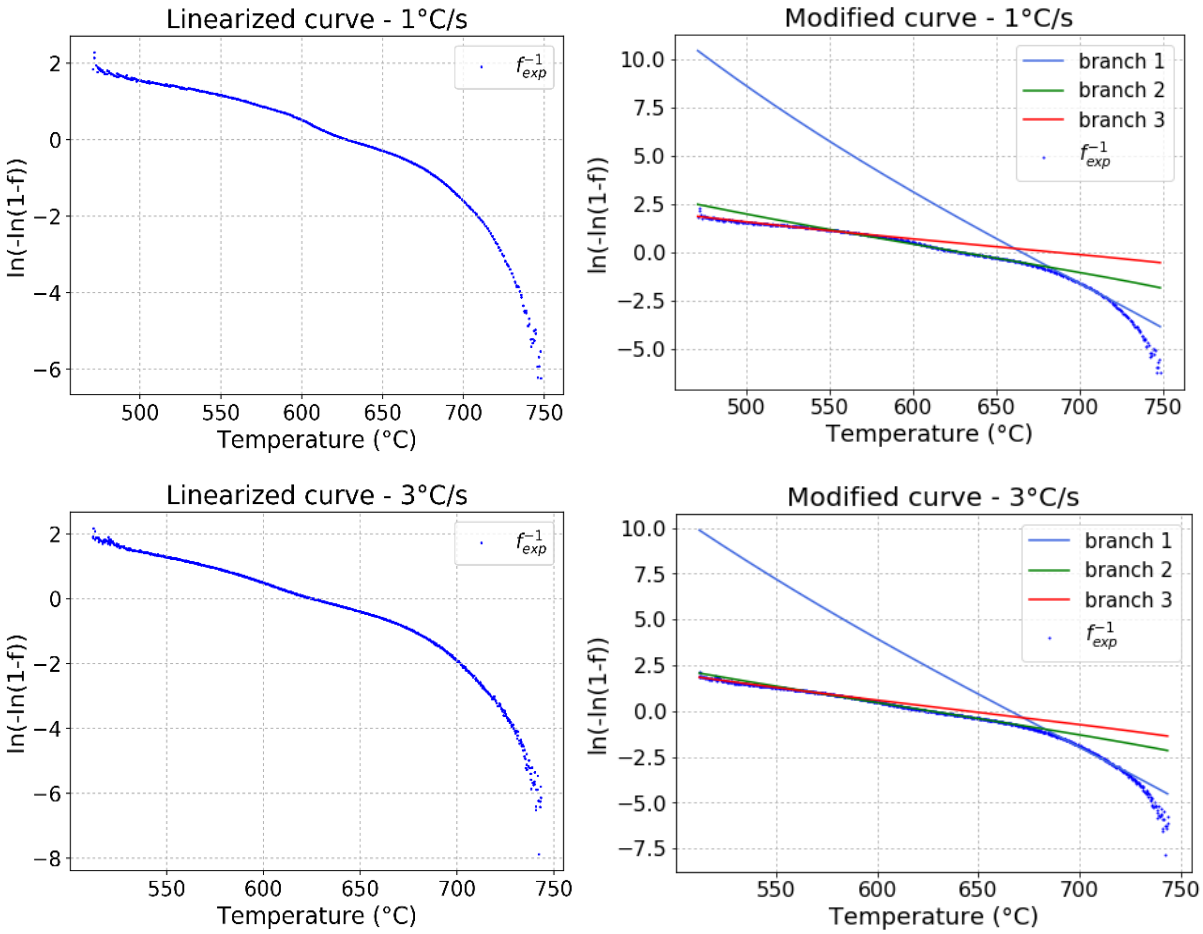


*Figure 4- 27: Modified curve and curve fitting associated for 1 and 3°C/s (Evraz X70-B steel).*

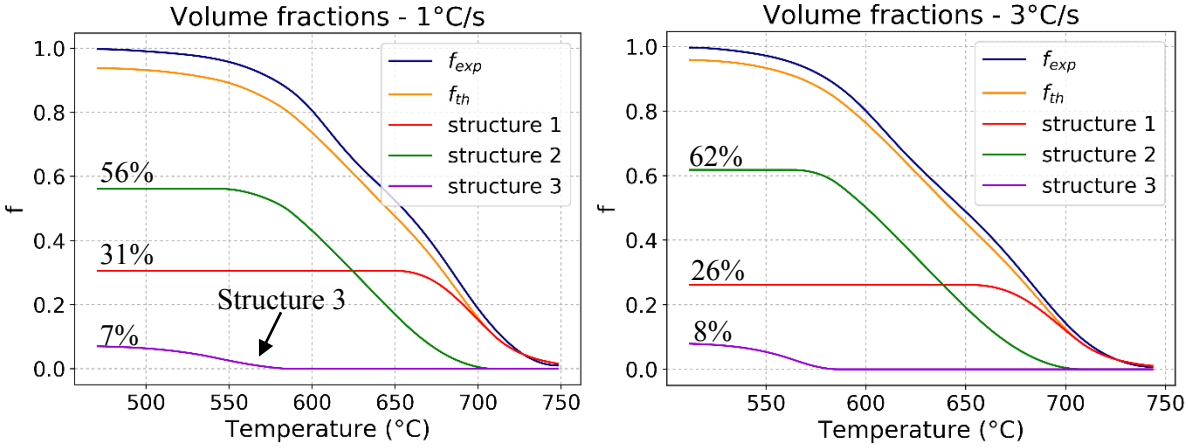


*Figure 4- 28: Evolution of the fraction transformed for the "three structures" approach for 1 and 3°C/s (Evraz X70-B steel).*

The fit of the experimental data is also acceptable with this approach. The shape of the evolution of structure 1, 2 and 3 is more consistent with the one found for the other cooling rates. Each inflexion point of the fraction transformed curve corresponds to the apparition of one structure. But for both results the amount of structure 1 seems low compared to the amount obtained with the previous steel (Evraz X70-A steel). This approach allows therefore to have a more regular shape of the evolution of the proportion of structures forming. However, it is only an assumption since this could also be a consequence of an experimental error in the dilation curve. A view of the microstructures may help resolve this issue.

#### *4.6.1.3. Experimental validation*

In Figure 4-29 the structure domains found with the model considering only two structures are compared with the Evraz CCT diagram. The start and finish temperature of the whole transformation are in agreement with the ones determined by Evraz, but the structures domains differ between the two CCT diagrams. It can also be noted that the transformation temperatures for 40°C/s do not agree with the CCT diagram from Evraz. The computed diagram predicts for every cooling rate the presence of two structures whereas in the Evraz CCT diagram there are three distinct structures. These are ferrite and pearlite at low cooling rate and only bainite for cooling rates over 10°C/s. However, the quality of the dilation curve for 1 and 3°C/s could affect the identification of the domains. For 1 and 3°C/s there is no distinct second rebound (i.e. following the first one) in the dilation curve that could justify the presence of a third structure like pearlite.

For each cooling rate two branches can be identified on the modified curve. According to the assumption made previously it means that two structures are formed over this range of temperatures. Nevertheless, the nature of the structures cannot be determined by the model. For example, according to the computed CCT diagram two structures are forming at 30 and 3°C/s. However, these two structures might not be the same depending on the cooling rate. At 30°C/s it could be bainite and martensite whereas at 3°C/s it could be pearlite and ferrite. The transition between these different structures at different cooling rates cannot be seen on the CCT diagram due to the lack of dilation data for intermediary cooling rates between 30 and 10°C/s as well as between 10 and 3°C/s.

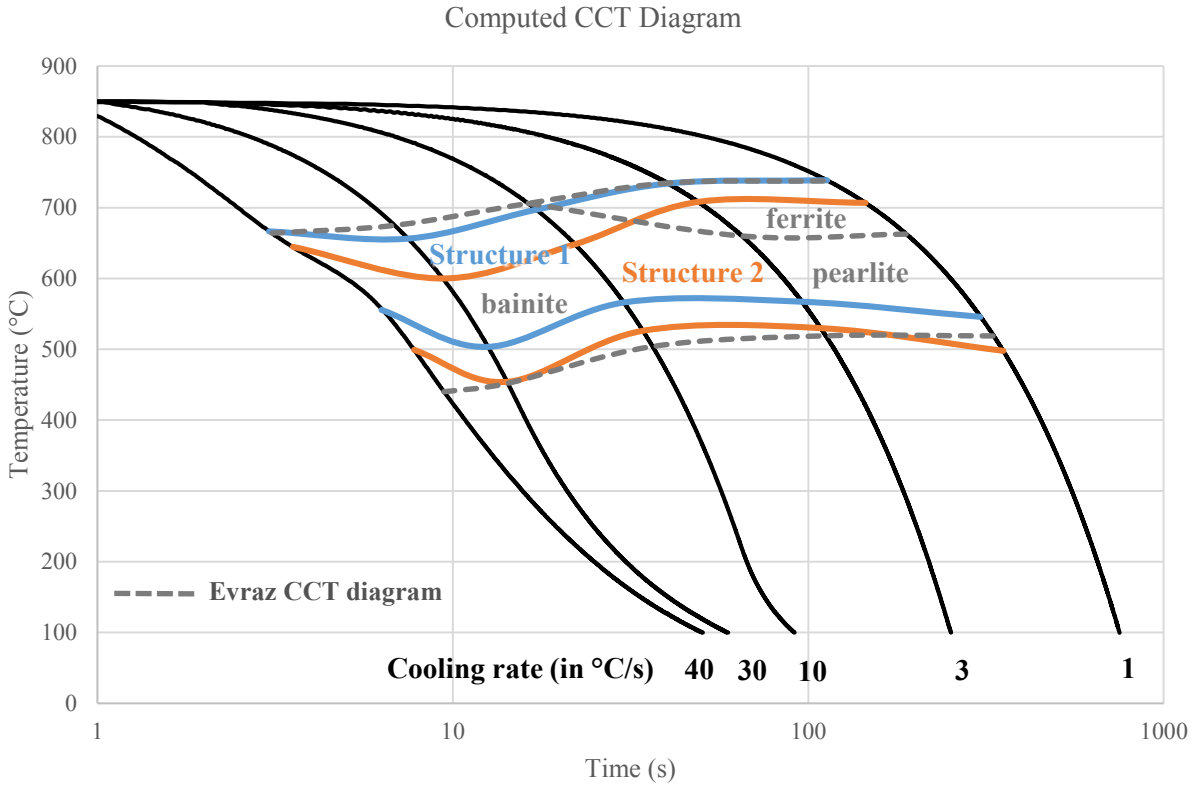


*Figure 4- 29: Comparison between the Evraz and computed CCT diagram considering the formation of only two structures for the Evraz X70-B steel.*

If the formation of a third structure for 1 and 3°C/s is assumed, the appearance of the CCT diagram is then modified as presented in Figure 4-30. With this approach, the domain for structure 1 match the ferrite domain for 1 and 3°C/s on the Evraz CCT diagram, which is a good indication on the validity of this three-structure approach. Additionally it appears that the domains of structure 1 and structure 2, and structure 2 and structure 3 are overlapping, which indicates a simultaneous formation of these structures.

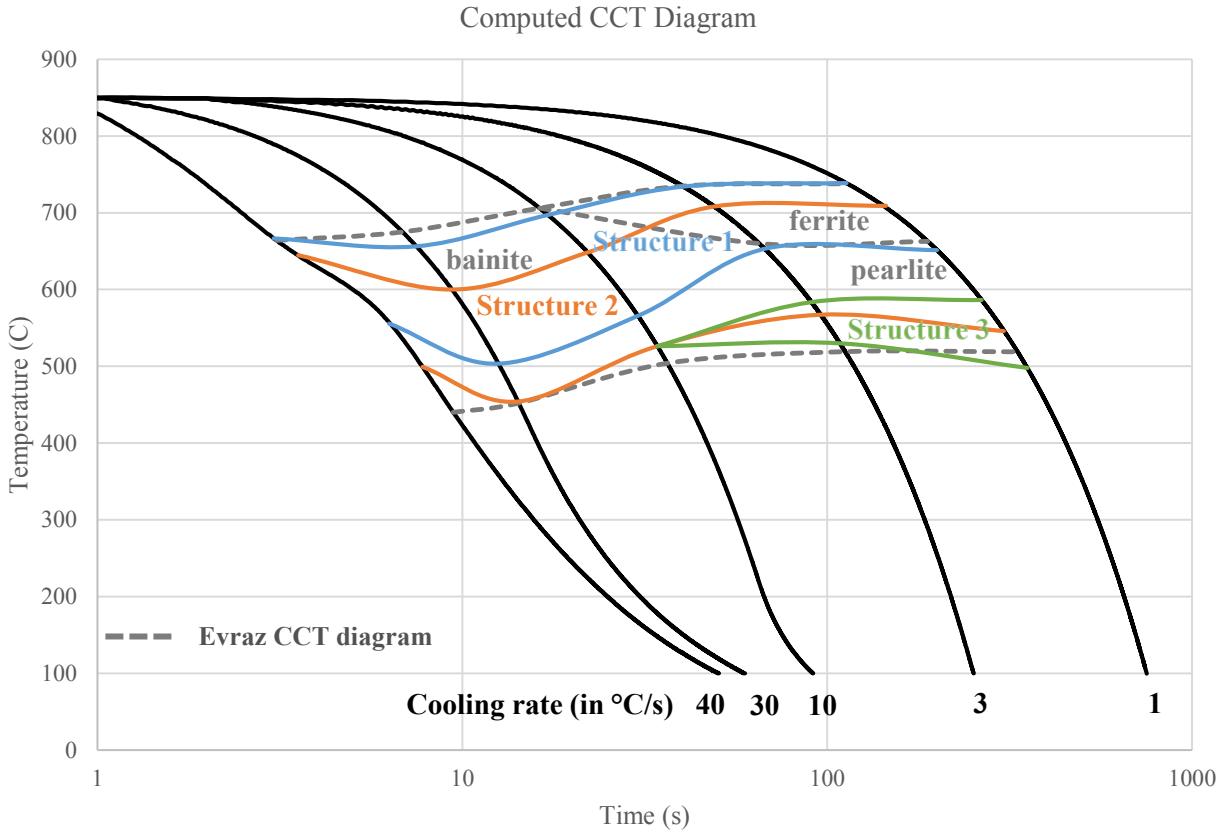


*Figure 4- 30: Comparison between the Evraz CCT diagram and the computed one using the "three structures approach" for the Evraz X70-B steel.*

Another way to validate the model is to look at the actual microstructures of the dilation samples and to compare the volume fraction with the computed one. As in Section 4.5.2, Evraz provided one micrograph per cooling rate. Thus, the micrograph only gives a qualitative assessment on the validity of the model. The micrographs are presented in Figure 4-31. Even if no pearlite can clearly be seen on the 1°C/s micrograph, Evraz added a pearlite domain on their CCT diagram, which might result from a more precise microstructure analysis.

The micrographs are then processed using the same approach as mentioned in Section 4.5.2, to find the experimental volume fraction. In this case, this technique is questionable, because for higher cooling rates it is hard to distinguish the polygonal ferrite from the acicular ferrite or bainite or martensite. The fact that only one micrograph at one magnification for each cooling rate is available complicates the microstructure analysis. The line-intercept method could be used, but it will have a similar uncertainty on the measurement. Thus, all the experimental results only give a general idea on the microstructure.

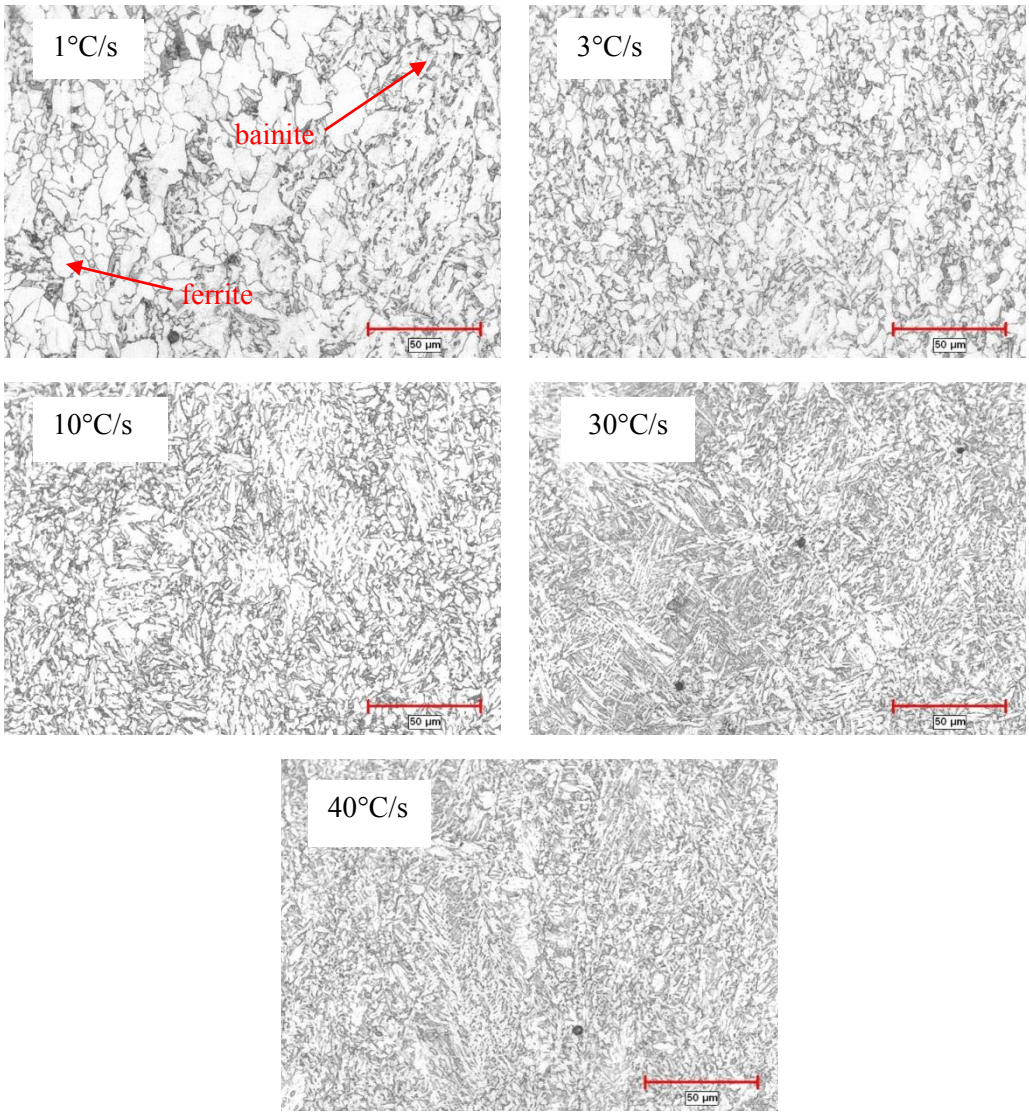


*Figure 4- 31: Micrographs of the dilation samples at different cooling rates (Evraz X70-B steel).*

The comparison between the experimental and computed values of the volume fractions is presented in Figure 4-32. This first graph shows the volume fraction obtained if only the formation of two structures for each cooling rate is considered. For 40°C/s the model seems to underestimate the amount of ferrite. This can come from the model itself because the fit is not perfect on the fraction transformed curve in Figure 4-26. However, the undetermined part would not compensate the gap between the model and the experimental measurement. The error could also come from the method used to experimentally measure the volume fraction on the micrographs, as mentioned previously.

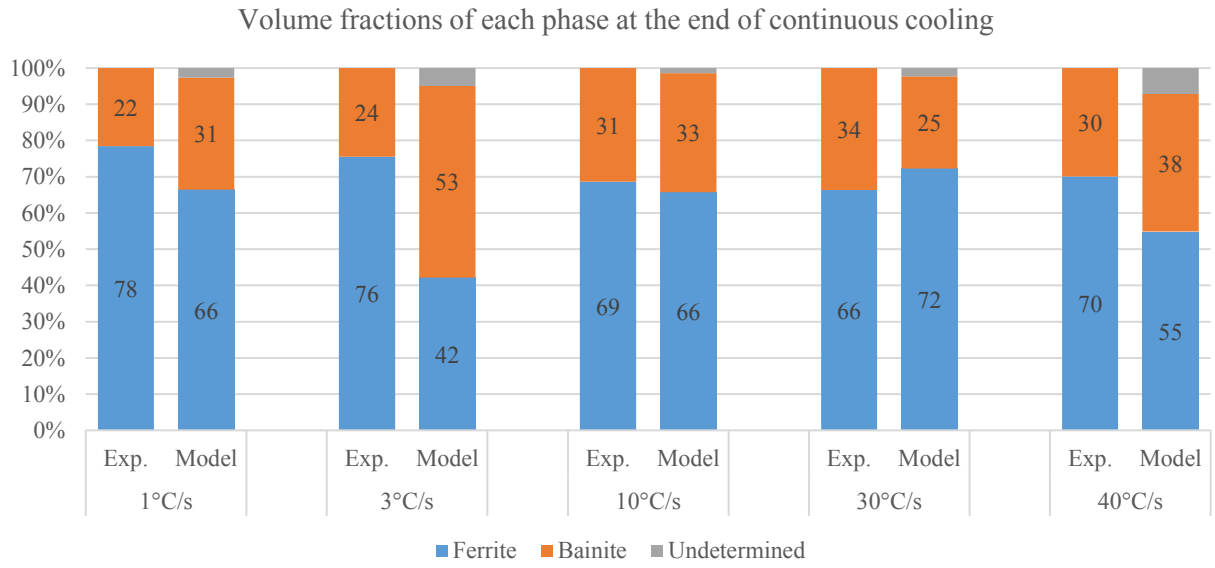


*Figure 4- 32: Comparison between the experimental and predicted volume fractions for the different cooling rates (Evraz X70-B steel).*

For 10 and 30°C/s the experimental and the computed value are almost in agreement, which is also the case for the fraction transformed in Figure 4-26. The model seems to be working whenever there is a good fit between the experimental and predicted fraction transformed. It was also the case for the steel studied previously for 1 and 10°C/s in Figure 4-16. It appears that a good fit between the predicted and experimental fraction transformed results in an accurate prediction of the volume fraction.

Lastly, for 1 and 3°C/s the model predictions do not match the experimental measurements. In both cases the model overestimates the amount of bainite. This effect is even stronger for 3°C/s, where the model predicts more bainite than ferrite. This error could come from the shape of the dilation curve (mentioned previously), that could affect the final prediction. Figure 4-33 shows the results for the "three structures" approach. In this case, the model estimation is worst because it overestimates significantly the volume fraction of bainite. The micrograph for 1°C/s in Figure 4-31 clearly shows some big grains of polygonal ferrite at a proportion probably higher than the 30% predicted by the model. Thus, the microstructure analysis tends to contradict the "three structures" approach for 1 and 3°C/s, since the experimental and the predicted volume fractions are different.

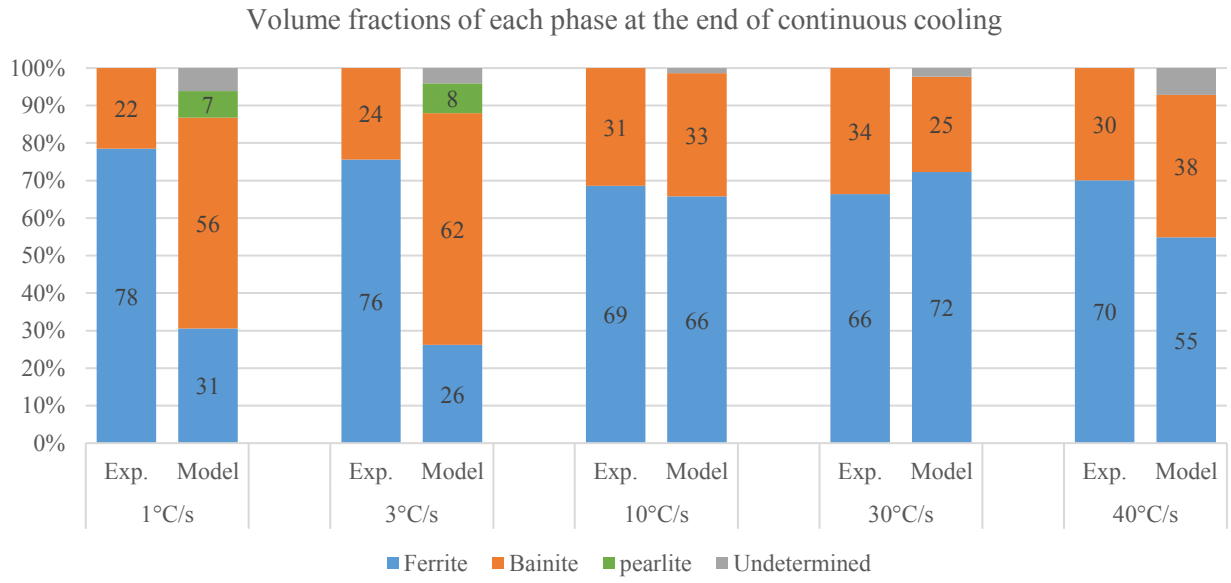


*Figure 4- 33: Comparison between the experimental and predicted volume fractions obtained with the "three structures" approach for the different cooling rates (Evraz X70-B steel).*

This steel has shown some mixed results for the model. On one hand, it confirmed the fact that a good fit on the fraction transformed curve leads to a reasonable prediction on the microstructure of the steel. On the other hand, both approaches on the dilation curves for 1 and 3°C/s did not give reasonable results for the microstructure. Nevertheless, the introduction of a third structure on the model has led to an improved agreement with the Evraz CCT diagram for the first structure.

## 4.6.2. Canmet - X80 steel

### *4.6.2.1. Steel composition*

Now the model is going to be validated on another steel where the data was generated at Canmet. The microstructure analysis has been done in detail by a previous member of the AMPL group in an unpublished work in 2015 [34]. The composition of this X80 steel is presented in Table 4-4.

*Table 4- 4: Comparison of the steel composition between the X80 steel from Canmet and the X70 steel used in the Evraz ROT.*

| | C | Mn | Cr+Ni+Mo+Cu | Nb |
|---|---|---|---|---|
| **X80 - Canmet** | 0.064 | 0.120 | 0.830 | 0.040 |
| **X70 - Evraz - ROT** | 0.049 | 1.630 | 0.634 | 0.075 |

#### *4.6.2.2. Application of the metallurgical model*

The dilation curves were obtained with a dilatometer and the samples were heated up to 950°C and held at this temperature for 15min. The dilation curves are presented in Figure 4-34. For 1 and 3°C/s the dilation curves are scattered in the middle of the large rebound. This will affect the whole analysis, since the model is based on these dilation curves. Additionally, a second rebound for 1°C/s between 400 and 600°C can be noticed. As mentioned previously, this second rebound might correspond to the formation of pearlite, which happens once the transformation of the previous structures associated with the first rebound is complete. It also appears that the dilation curves comprise less data points than the two-other steel studied before, which could also affect the result of the analysis.

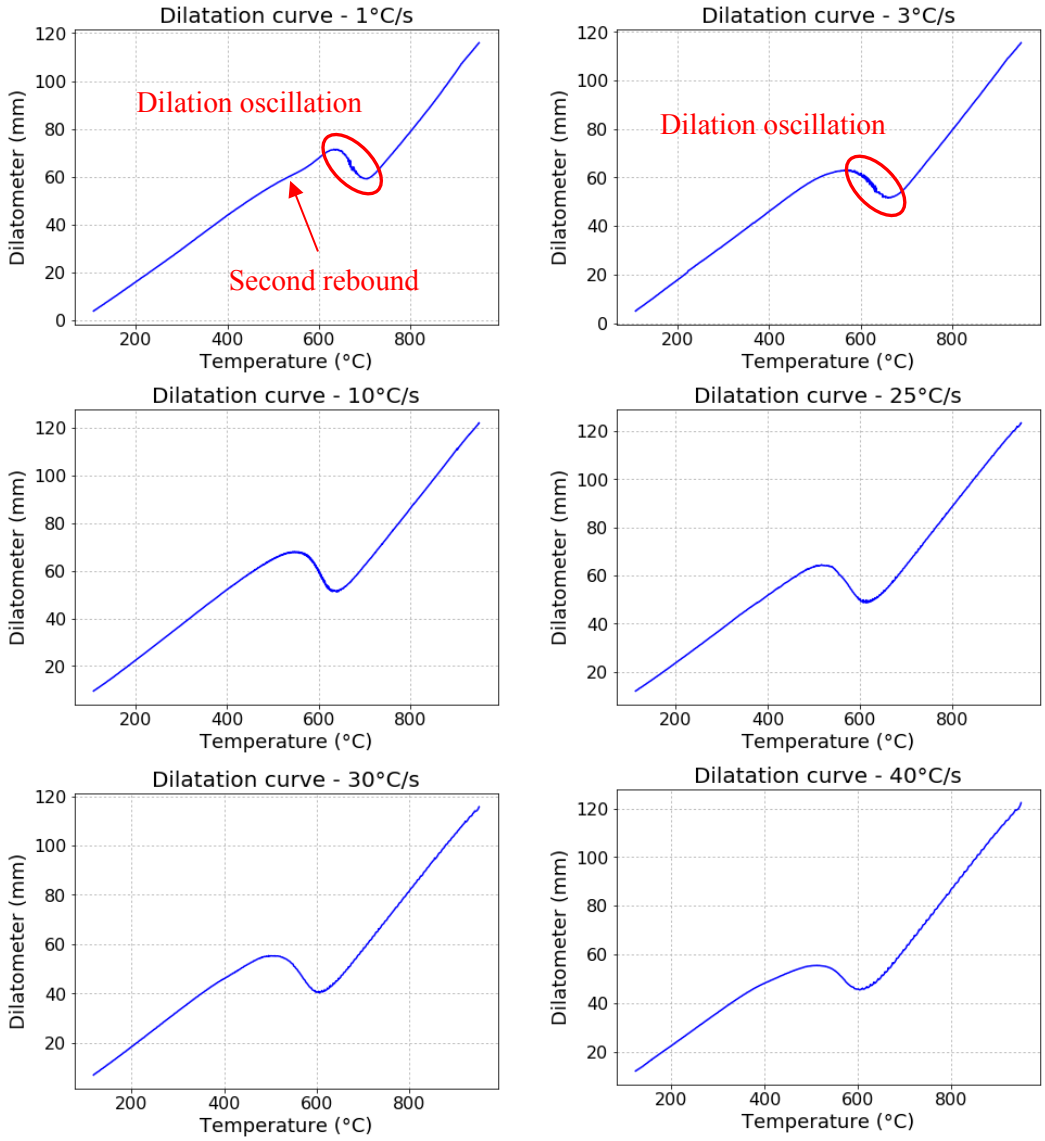


*Figure 4- 34: Dilation curves of the X80 samples for several cooling rates.*

The fraction of transformed austenite is obtained using the lever rule and the curves are presented in Figure 4-35. Overall, the data is more scattered compared to the previous steels, and as expected, there are also less data points, which will affect the accuracy of the curve fitting. This is particularly the case in the middle of the curves for 1 and 3°C/s. Nevertheless, all the modified curves reveal the formation of two distinct structures. However, as mentioned in the previous section these two structures might not be the same ones depending on the cooling rates. The only way to have information on the nature of the structures that are formed is to look at the microstructure.

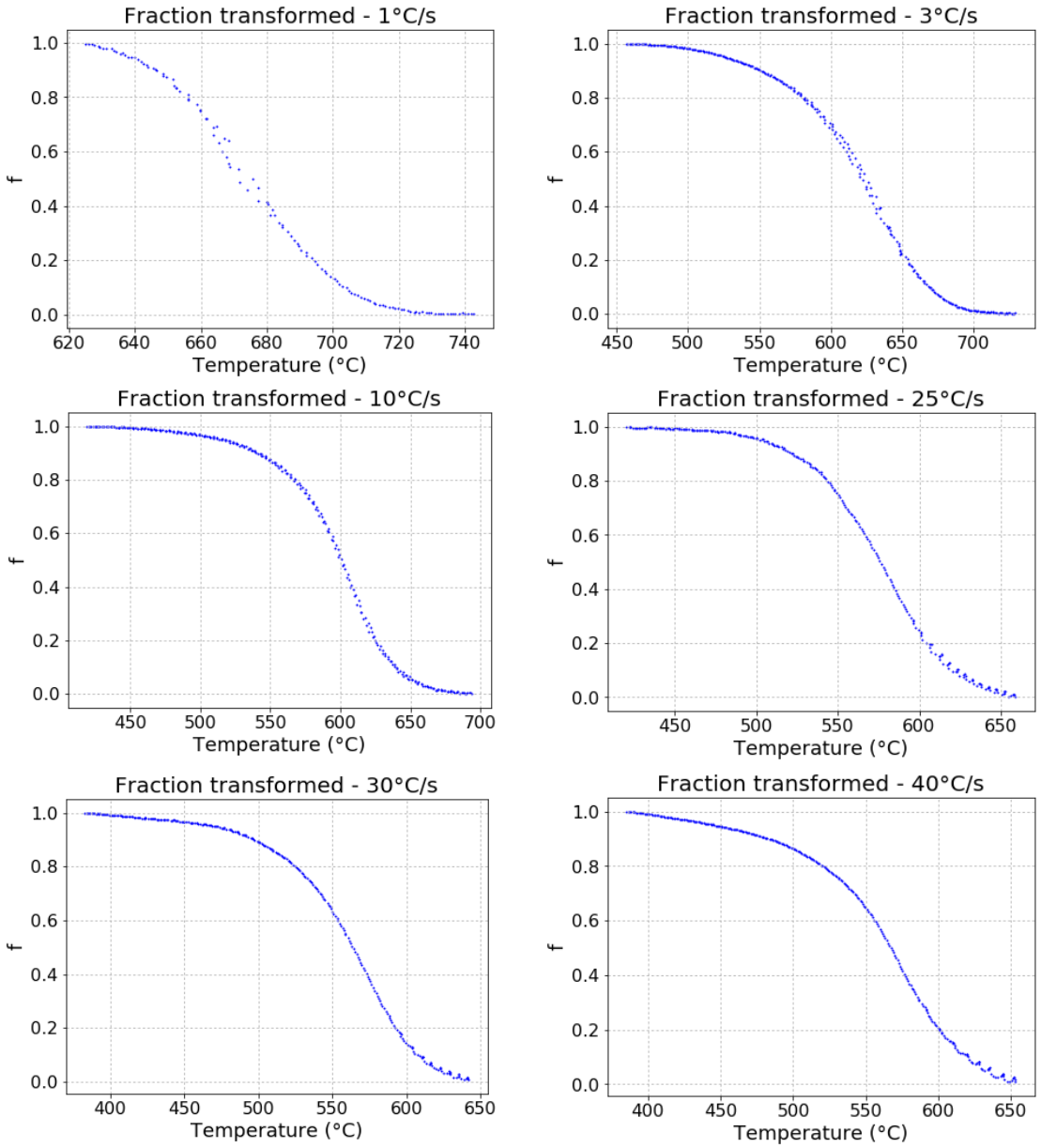


*Figure 4- 35: Fraction transformed for different cooling rates (X80 steel).*

The Avrami parameters (n, Q and $\tau_0$) are then determined and the evolution of the volume fractions is obtained by introducing a parameter α. The results are presented Figure 4-36. Overall, the fit of the fraction transformed of austenite is relatively good. For the cooling rates from 10 to 40°C/s the difference between the experimental and the predicted fraction transformed at the end of continuous cooling is relatively good. However, for 3°C/s, the shape of the evolution of structure 1 is influenced by the original shape of the fraction transformed. The scattered aspect of those curve might have introduced some numerical error in the model that could affect the final results. For 1°C/s, the lack of data points in the temperature range, where both structures are formed, have considerably affected the accuracy of the curve fitting.

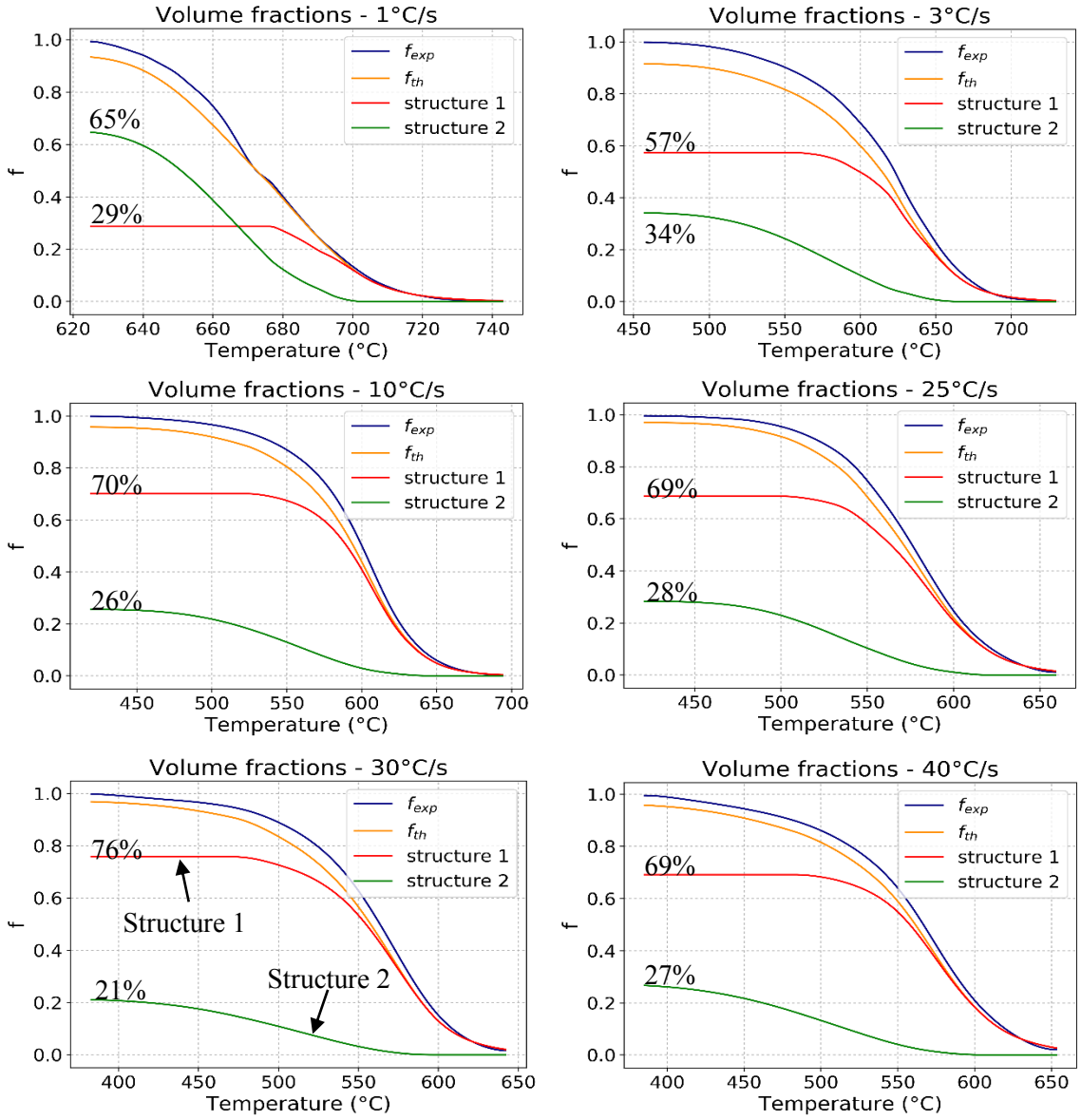


*Figure 4- 36: Fraction of austenite transformed for different cooling rates (X80 steel).*

At the end of the transformation, the volume fraction of structure 2 is higher than structure 1, which was not the case for the steels studied previously. Thus, the results for this specific cooling rate might not be relevant. This shows that the model is strongly dependent on the quality of the dilation data. If the curves are scattered or if they do not comprise enough data points, the final results on the structure fractions might then be skewed.

#### *4.6.2.3. Experimental validation*

The CCT diagram predicted by the model is presented in Figure 4-37. Unfortunately no experimental CCT diagram is available to validate the results. It appears that the transformation temperatures are consistent, except for 30 and 40°C/s, which might be due to the relatively poor quality of the dilation curves. It can also be noted that a second rebound in the dilation curves can be observed for 1°C/s in Figure 4-34, which justifies the presence of a structure 3 domain in the CCT diagram in Figure 4-37.

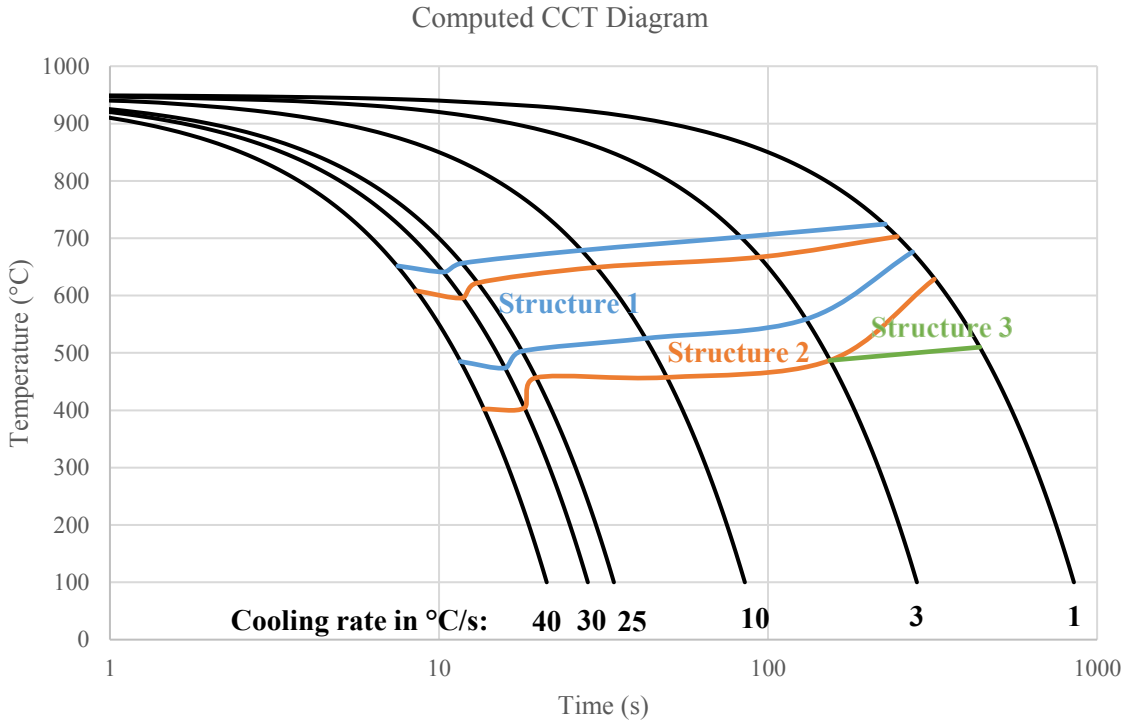


*Figure 4- 37: Predicted CCT diagram for the X80 steel*

Figure 4-38 shows the comparison between the volume fractions obtained experimentally and predicted by the model. As mentioned previously, the microstructure analysis was done by another

student in 2015 [34]. The measurement of the volume fraction was done using point count technique on SEM micrographs. For all the cooling rates, there are two main structures that are forming. For 1 and 3°C/s there are also some pearlite that is not predicted by the model (i.e. when the second rebound associated with pearlite is not in the same temperature range as the large rebound). Overall, it appears that the model underestimates the volume fraction of ferrite. For cooling rates between 10 and 40°C/s the error between the experimental and the predicted value is around 10%. The undetermined fraction never exceeds 5% for these cooling rates, and thus, it cannot be the main reason behind the underestimation of ferrite. Another explanation could be the error on the experimental measurement, but no information on its accuracy was provided. For 1 and 3°C/s the model has difficulties predicting the volume fractions. The amount of bainite is too large and especially for 1°C/s. This is probably due to the quality of the dilation curves mentioned previously and it confirms that the model strongly depends on the experimental input data.

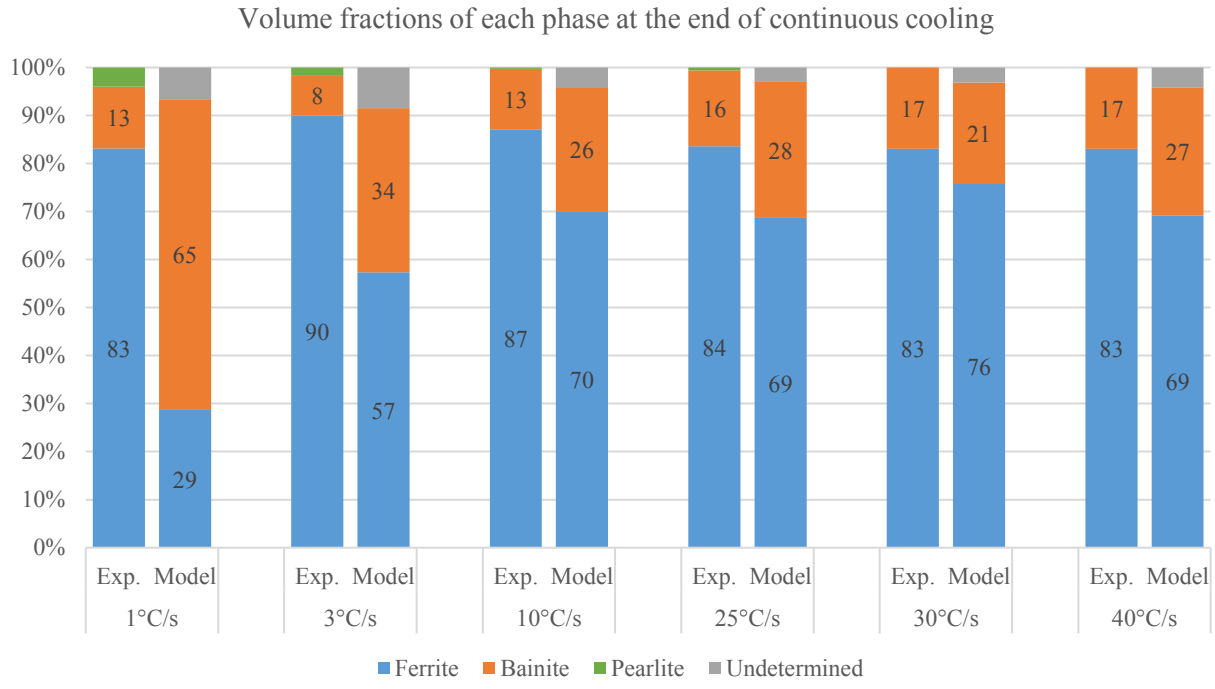


*Figure 4- 38: Comparison between the experimental and predicted volume fractions for the different cooling rates (X80 steel).*

The results on these two other steels have highlighted some strengths and weaknesses of the model. It has shown that the quality of the dilation curves is a key point for the accuracy of the model. It was also showed that the model could handle more than two structures. Even though, the volume fraction results

were not in agreement with the experimental measurement, the shape of the CCT diagram was promising with this approach. Finally, it was illustrated that a good fit of the fraction of austenite transformed will result in an accurate volume fraction prediction. This is really encouraging regarding the validity of the model.

## 4.7. Metallurgical model summation

In the literature, basic metallurgical models apply the Avrami equation in order to predict the evolution of the fraction of austenite transformed. Most researchers quantify the transformation by fitting the Avrami equation to obtain values of the Avrami parameters. In this work, a different approach is proposed. The approach is based on a modified form of the fraction transformed. A weighted fraction was used to transition between transformed structures. The simultaneous formation of two structures was addressed in the present work and three steels were evaluated with the model. Briefly, the strength of the model developed are:

1) Accurately predicts the evolution of the fraction of austenite transformed
2) Considers the simultaneous formation of two structures
3) Improves the basic CCT diagrams by clearly identifying the structure domains
4) Calculates the volume fractions of austenite, ferrite and bainite at the end of continuous cooling

However, the metallurgical model has also shown some weaknesses:

1) The accuracy of the analysis strongly rely on the quality of the experimental dilation data
2) The model does not study the transformation of the whole austenite, because only the large rebound is considered (i.e. the formation of pearlite is not predicted by the model). This is due to the lever rule that determines the evolution of the fraction of austenite transformed for only one rebound in the dilation curve at a time.
3) Numerical errors are introduced in the model, due to the processing of experimental data (i.e. position of tangents, curve fitting, numerical derivative and integration). Thus, the model can be improved using more complex and accurate numerical methods such as the Simpson's rule for the integration.
4) Some parts of the model were  are not based on existing theoretical work (i.e. interpretation of the modified form of the Avrami equation, introduction of the parameter $\alpha$)
5) The model results have not been accurately validated by a complete and precise microstructure analysis

# Chapter 5: Thermo-metallurgical Model

Cooling of the steel in the ROT has been modelled in Chapter 3. A model of the phase transformation has been developed for continuous cooling in Chapter 4. The objective of this section is to combine the thermal and the metallurgical models to predict the phase transformation and their respective volume fractions that occur during ROT cooling. This will be done using the Scheil's additivity rule. A microstructure analysis was done to validate the model, by comparing the predicted and measured volume fractions. The model will then be applied to hypothetical ROT configurations including an early cooling scenario and a delayed cooling scenario.

## 5.1. Application of the Scheil's additivity rule to ROT cooling

The metallurgical model is able to predict the evolution of the phase fractions during continuous cooling. The goal is to use the Scheil's additivity rule to extend this model to non-continuous cooling such as ROT cooling. The principle of this rule is to divide the thermal history into small time increments and apply the metallurgical model to the corresponding cooling rate.

First the cooling rate of ROT cooling needs to be determined by taking the derivative of the temperature profile. The thermal profile of the steel plate has been predicted with the thermal model. Since, the temperature profile varies through the thickness of the skelp, the analysis will only focus on the three control nodes A, B and C. Where A is located at the surface of the skelp, C at the centerline and B at the quarter, as presented in Figure 5-1. Thus, another objective of this section will be to characterize the difference in microstructure through the thickness of the steel.

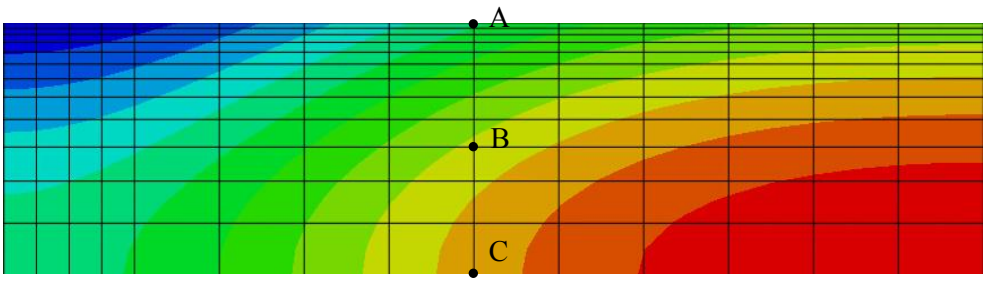


*Figure 5- 1: Position of the control nodes on the FEA region.*

### 5.1.1. ROT cooling rate

The three predicted temperature profiles for A, B and C are presented in Figure 5-2, which shows that the cooling rate is not constant during the process. The cooling rates at the three positions are presented in Figure 5-3. At the centerline, the cooling rate primarily oscillates between 10 and 20°C/s. For node B, since the impact of surface cooling is more important, the cooling rate alternates between stages of high cooling rates (up to approximately 35°C/s) and lower ones (approximately 3°C/s). Furthermore, the cooling rate at the surface is completely different. At the surface, the skelp undergoes a series of cooling stages and temperature rebounds. In both cases, a large range of cooling and heating rates is covered: from about 15 to 400°C/s (the negative values of cooling rate correspond to a temperature rebound).

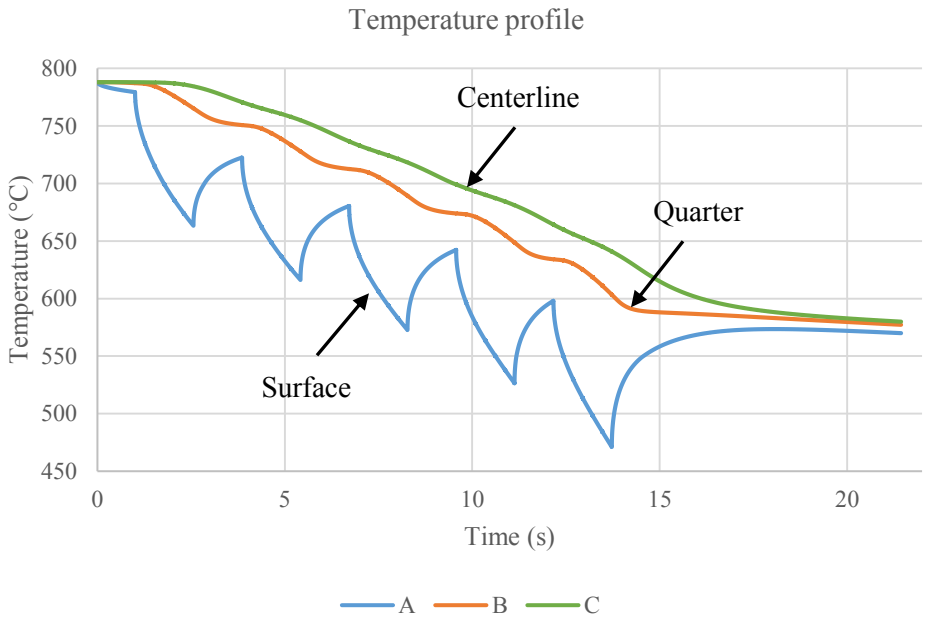


*Figure 5- 2: Thermal history of the control nodes.*

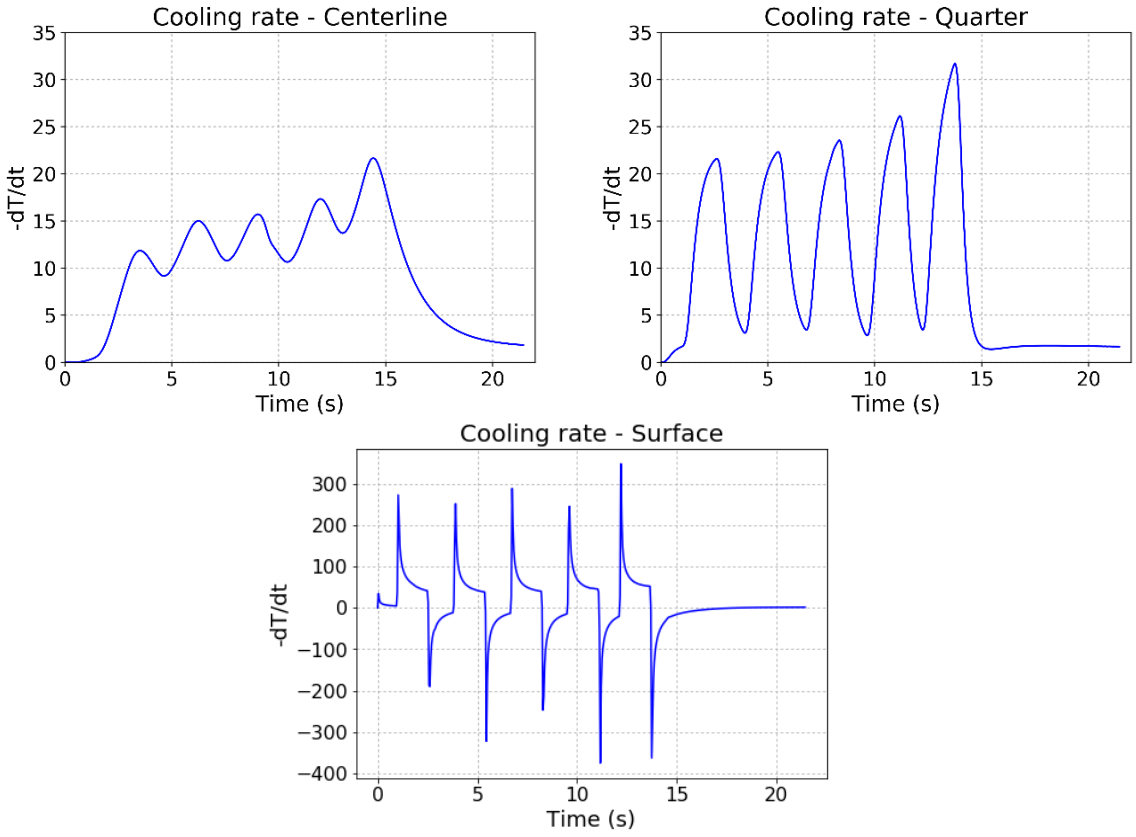


*Figure 5- 3: Cooling rate of ROT cooling at the three control nodes A (surface), B (quarter) and C (centerline).*

Ideally, in order to apply the Scheil's additivity rule, the Avrami equation for the whole range of cooling rates needs to be known. However, as mentioned previously in Chapter 4, the extrapolation of the Avrami parameters for any cooling rates was not possible. Thus, the model is not feasible to predict the evolution of the phase fractions for every value of cooling rate involved in ROT cooling. The cooling rate must therefore be estimated with the continuous cooling, for which dilation data is available.

The surface node A undergoes a succession of cooling and heating stages, which is problematic. In most cases, the cooling and heating dilation curves are different (usually the heating dilation curve is above the cooling one) [28]. It means that the phase transformation happens at different temperatures whether the sample is heated or cooled. This issue can be overcome by using the metallurgical model with heating dilation curves (i.e. following the same process described Chapter 4). However, only cooling dilation data was available for this work.

Another way to solve this issue is to assume that no reverse transformation will occur during heating. However, the surface node A reaches very high cooling rates (up to more than 350°C/s), whereas the maximum available cooling rate data for all the datasets is only 40°C/s.

Additionally, the temperature profile below the surface is similar to the top one as presented in Figure in 5-4. It compares the thermal history of the node A at the surface with a node 1.5mm below it (whereas node B is 4.3mm below the surface). The two curves are similar and the cooling rate below the surface peaks at 200°C/s, which is also higher than the experimental dilation data. For nodes between 0 and 3.5mm below the surface, reheating stages can be observed. For the remainder of the model it was therefore decided not to consider the node A and to only focus on nodes B and C.

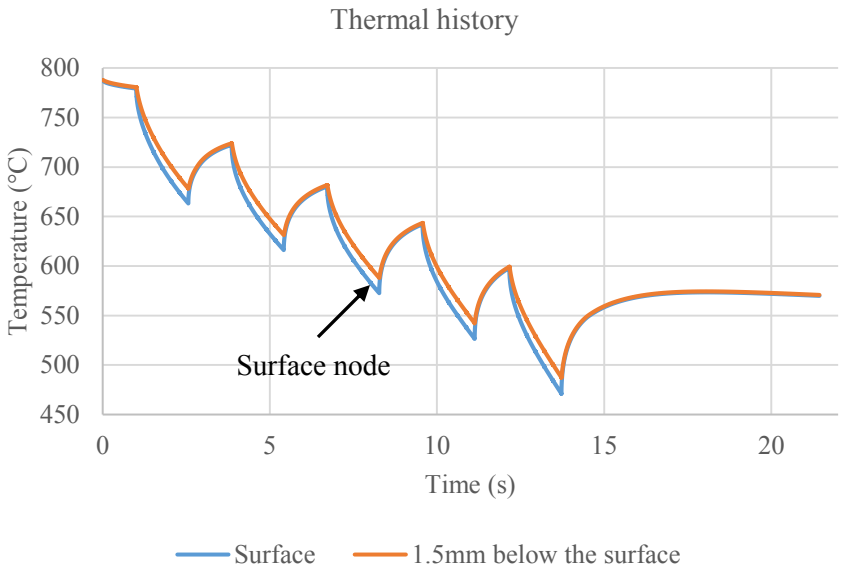


*Figure 5- 4: Thermal history of the surface node A and at a location 1.5mm below A.*

The cooling rate curves of nodes B and C are divided into four regions, associated with the four cooling rates, dilation data is available, as presented Figure 5-5. The thresholds between the domains is set at 2, 4 and 7.5°C/s (i.e. which are the middle values between the cooling rates 1, 3, 5 and 10°C/s of the available dilation data). Figure 5-6 shows the approximation of the cooling rate during the run-out table cooling.

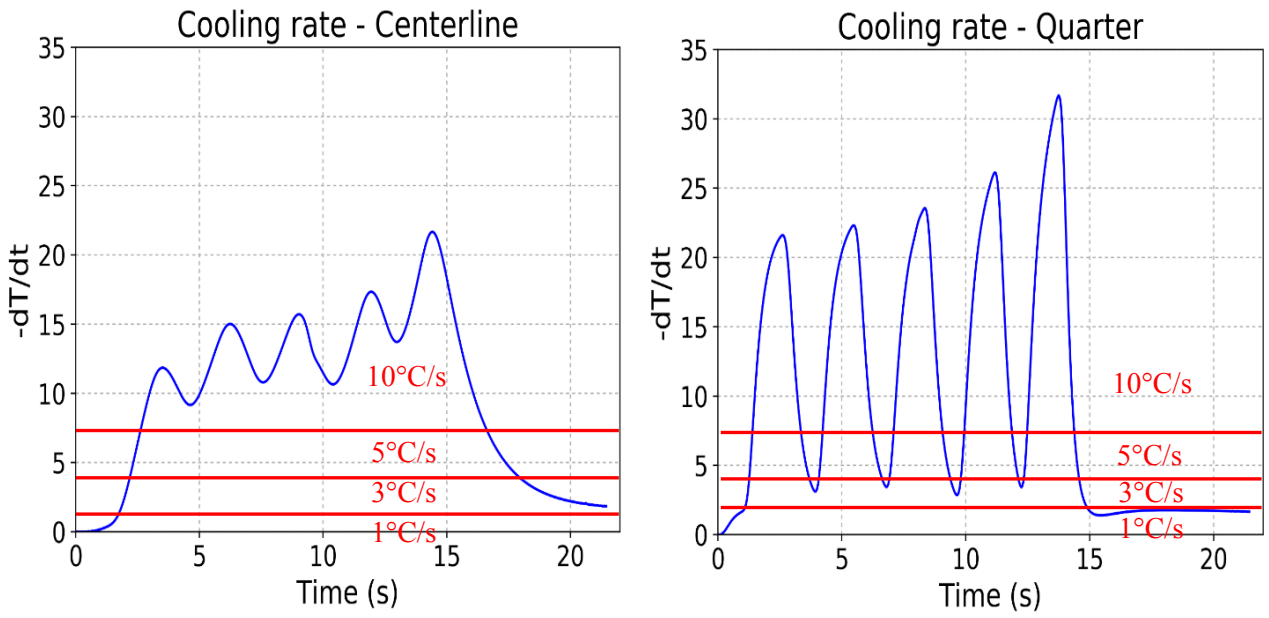


*Figure 5- 5: Evolution of the cooling rates with temperature for nodes C (centerline) and B (quarter).*

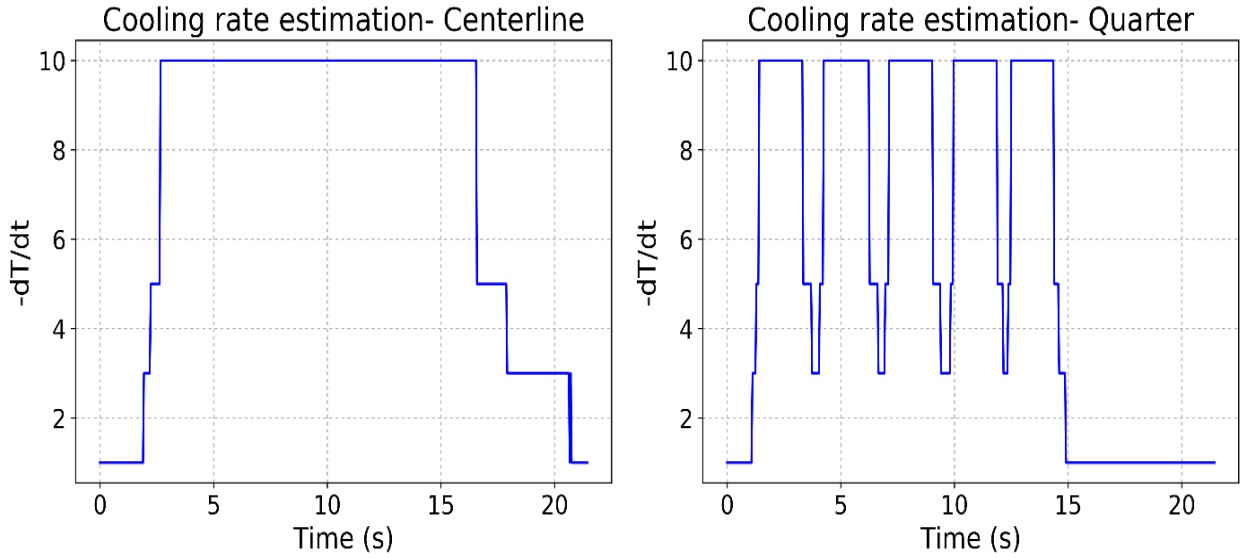


*Figure 5- 6: Estimation of the cooling rates for the centerline and the quarter node.*

### 5.1.2. Application of the Scheil's additivity rule to the estimated cooling rate

Now that the cooling rate is estimated for every temperature, the Scheil's additivity rule can be applied to nodes B and C and is expressed as follow:

$$\begin{cases} f_{i+1} = 1 - exp\left[-\left(\dfrac{t_i^* + \Delta t_{i+1}}{\tau_{i+1}}\right)^n\right] \\ t_i^* = \dfrac{ln(1-f_i)^{1/n}}{\tau_{i+1}} \end{cases} \tag{5.28}$$

Where f is the fraction of austenite transformed, t the time, τ the characteristic time. The theory behind Equation 5.1 is that at each time increment the Avrami equation (corresponding to the specific cooling rate) is applied. The Avrami equation gives the rate of transformation of a single structure. The Scheil's additivity rule is therefore applied to the transformation of austenite. Nevertheless, the volume fraction of ferrite and bainite can be determined, using the ferrite and bainite curves associated with the corresponding cooling rate during the process. In Equation 5.1, the introduction of the time $t_i^*$ reflects the fact that the transformation will resume from the previous value of the fraction transformed, but will follow the evolution of the cooling rate associated with step (i+1). This principle is illustrated bellow:

**Scheil's additivity rule:**

- The transformation starts when the temperature of the node considered, reaches the starting transformation temperature associated with the specific cooling rate. Those starting transformation temperatures where determined in Chapter 4 and are summed up in Table 5-1:

*Table 5- 1: Starting transformation temperature for different cooling rates.*

| Cooling rate | 1°C/s | 3°C/s | 5°C/s | 10°C/s |
|---|---|---|---|---|
| $T_{start}$ | 770°C | 779°C | 755°C | 734°C |

- Using the evolution of the cooling rate with temperature, the transformation start temperature and the values of cooling rates during the run-out table cooling are identified in Figure 5-7:

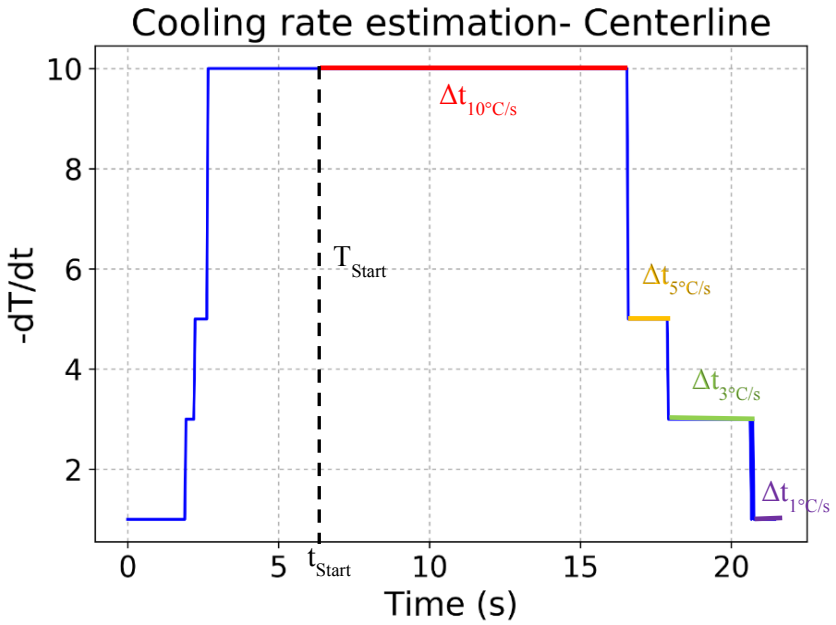


*Figure 5- 7: Evolution of the cooling rate estimation at the centerline with temperature.*

- Then the temperature profile is divided into regions with the same cooling rate, starting from $T_{start}$, and the associated change in temperature ΔT are determined in Figure 5-8:

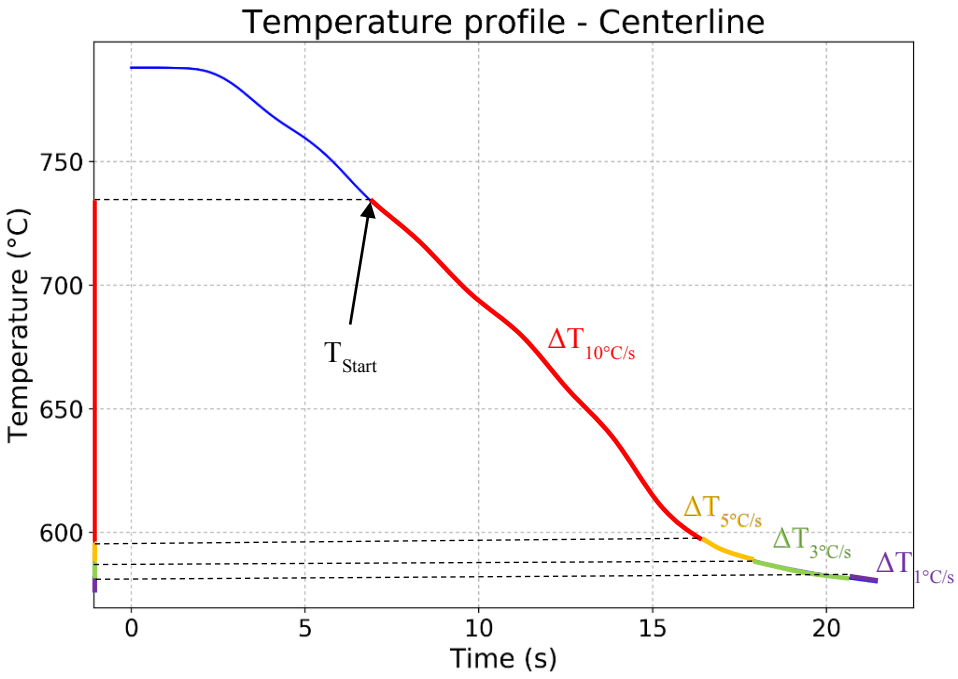


*Figure 5- 8: The thermal history of the centerline is divided into regions of constant cooling rate.*

- The fraction transformed for each cooling rate and the corresponding ΔT are identified Figure 5-9:

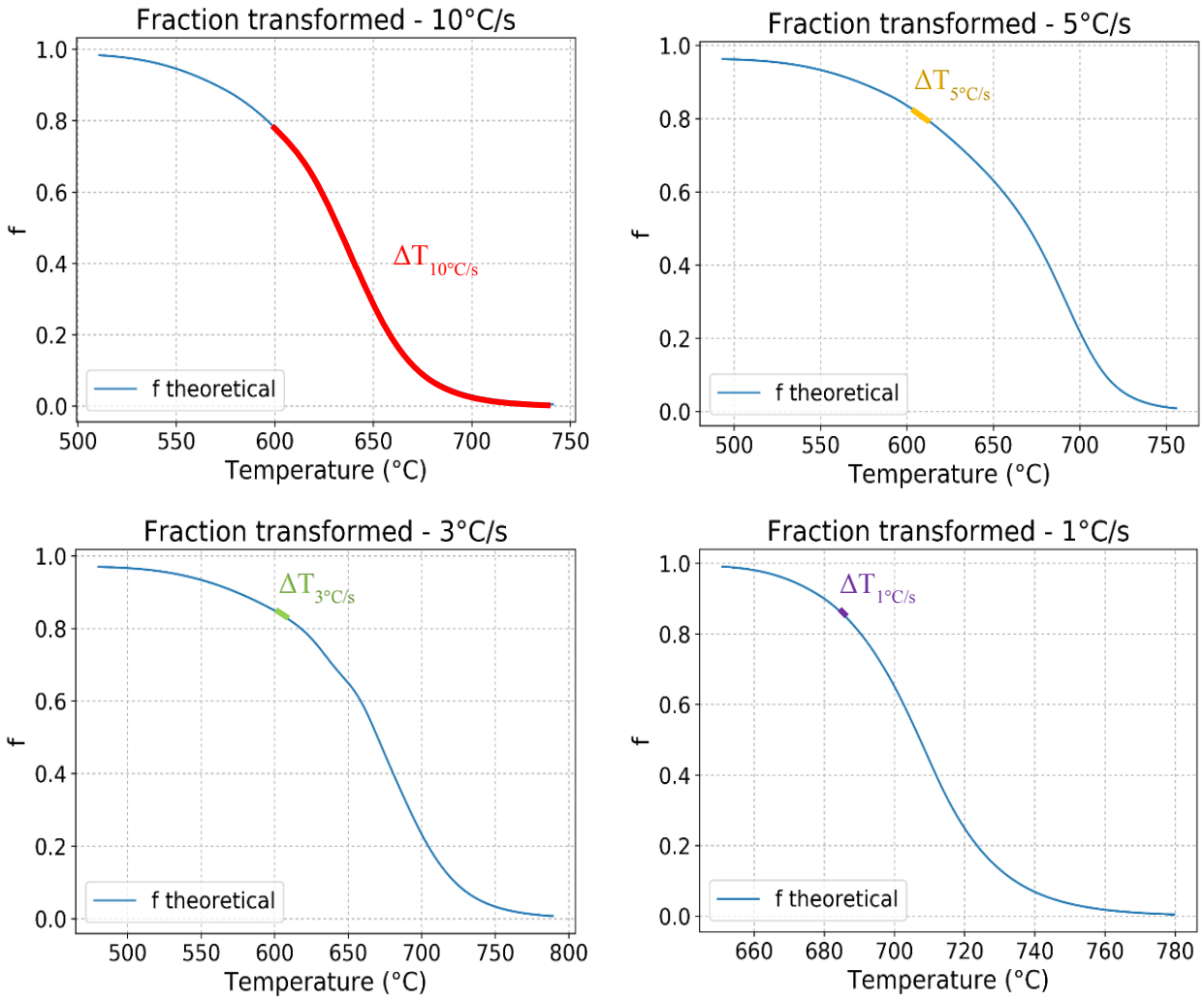


*Figure 5- 9: Fraction transformed of each cooling rate used for the Scheil's additivity rule.*

- The fractions transformed are then added on a single curve in Figure 5-10 to have the evolution of the theoretical fraction of austenite transformed with temperature:

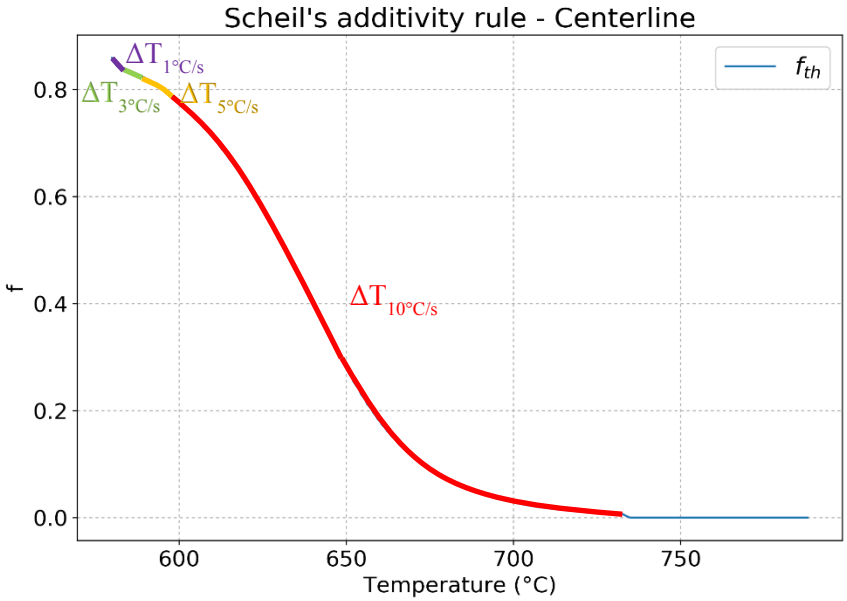


*Figure 5- 10: Evolution of the theoretical fraction transformed with temperature during the run-out table cooling.*

- Finally, the evolution of the theoretical fraction transformed with the time during the ROT cooling is obtained in Figure 5-11:

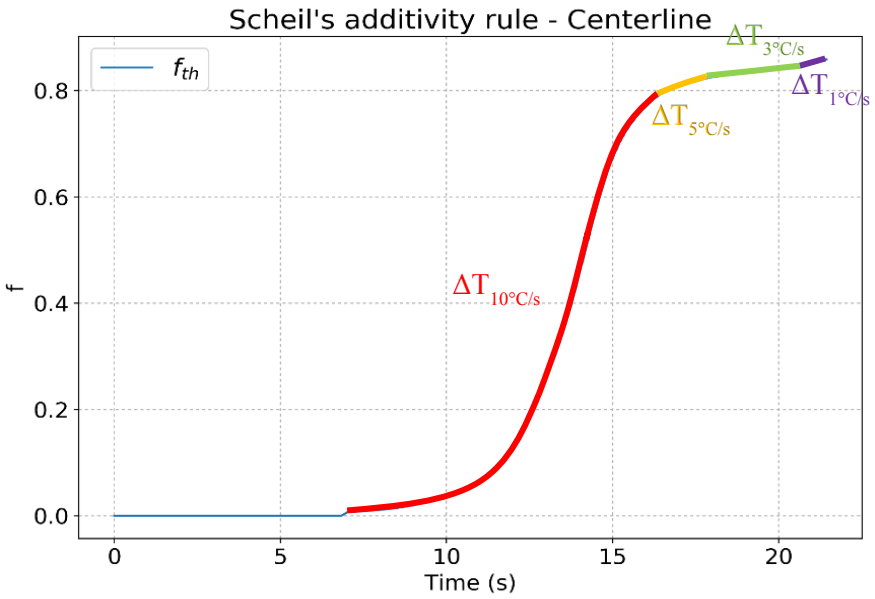


*Figure 5- 11: Evolution of the theoretical fraction transformed with time during the run-out table cooling.*

As the run-out table cooling progresses and while the cooling rate is constant, the fraction transformed will increase following the curve associated with the cooling rate corresponding (showed by the colored lines in Figures 5-7 to 5-11). When the cooling rate changes, the transformation will resume from the same value of f on the next fraction transform curve, and will then increase following its evolution. Meanwhile, the evolution of the ferrite and bainite fractions is obtained with the same method on the predicted ferrite and bainite curves obtained in Chapter 4.

### 5.1.3. Application to X70-A steel without strain

The results for nodes B and C are presented in Figure 5-12.

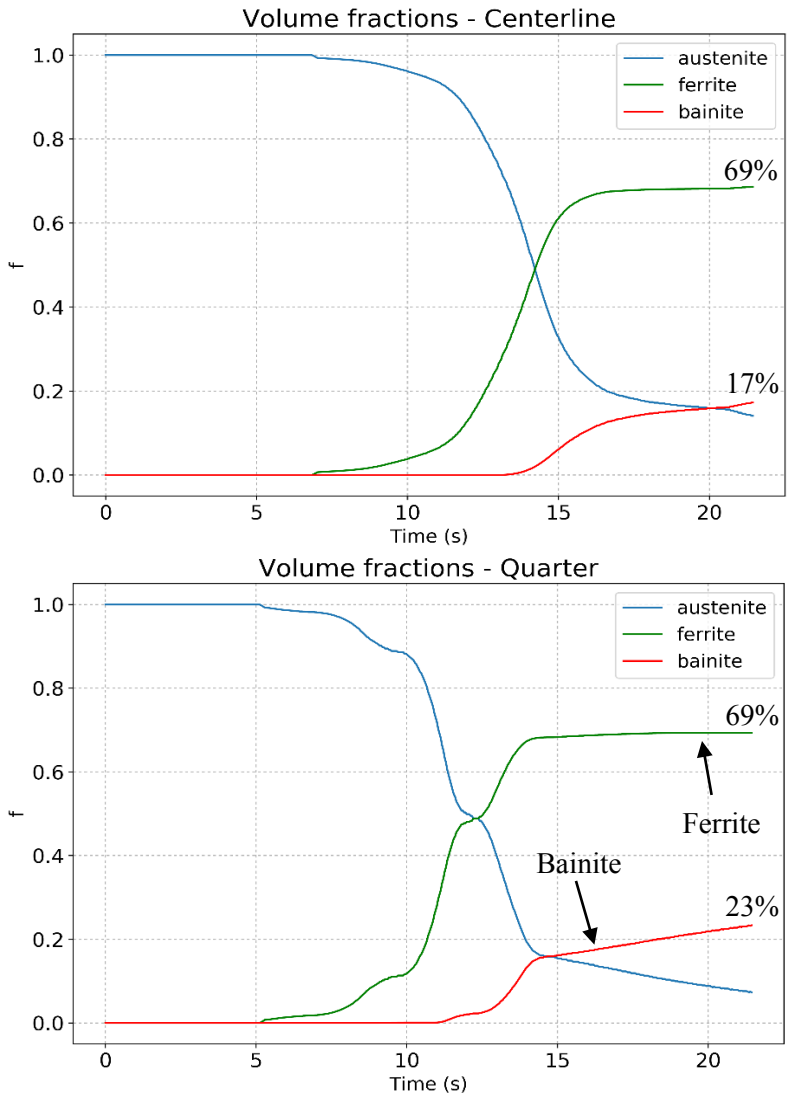


*Figure 5- 12: Evolution of the computed volume fraction of austenite, ferrite and bainite during the run-out table cooling.*

The results show that in both case the transformation is not complete. Looking at the CCT diagram Figure 5-13, it shows that for all cooling rates the transformation happens over a range of temperatures of more than 200°C. Additionally, the transformation starts at 734°C, which is the starting transformation temperature for 10°C/s. Thus, the global transformation during the ROT cooling should finish around 534°C (this is only an approximation). This temperature is below the one measured by the pyrometer at the end of the ROT (575°C), which explains why the transformation is not over yet.

However, after the pyrometer, no information on cooling is available. It can be assumed that the cooling is only radiative, and the cooling rate must be significantly less than 1°C/s, but this needs to be confirmed in a future work. For both positions on the skelp, it also seems that the formation of ferrite is complete. Thus, it can be assumed that the remaining austenite will probably transform into bainite, pearlite or remain as retained austenite. However, for very slow cooling, it appears that the CCT diagram predicts pearlite.

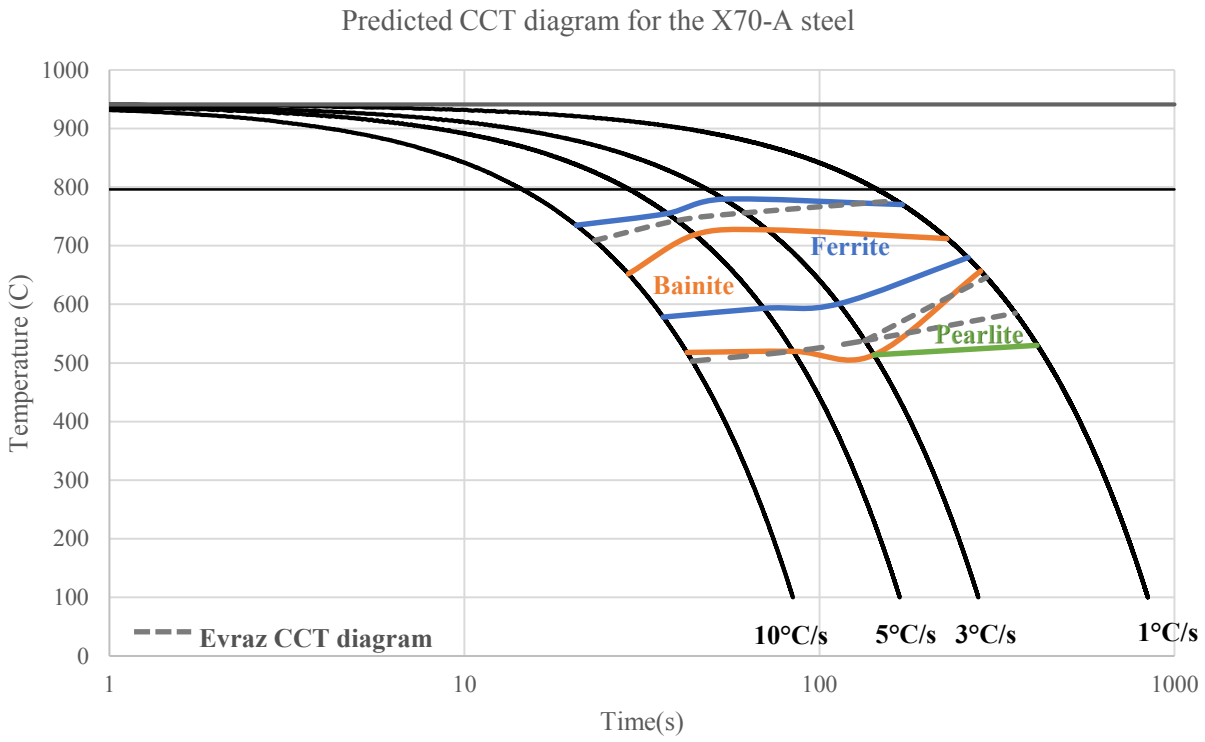


*Figure 5- 13: CCT diagram predicted by the model.*

### 5.1.4. Application to X70-A steel with strain

According to the model, the transformation of austenite only starts after approximately 5s (as shown in Figure 5-12), which leads to an incomplete transformation at the end of the ROT. Additionally, the amount of untransformed austenite seems higher than the values found in the literature [12]. One explanation could be the difference between the experimental and predicted fraction transformed of austenite for continuous cooling. For almost all continuous cooling, the predicted fraction transformed does not reach 100% due to numerical errors. This could partially explain the amount of untransformed austenite at the end of the ROT cooling.

Another reason could be the influence of the strain on the transformation temperatures. It has been shown in the literature that the strain has an impact on the phase transformations, which could start at a higher temperature [30]. An unpublished study made by Evraz shows that for a steel, similar than the one used in the ROT, the transformation of austenite for samples with a 65% deformation from their initial length, happens approximately 30°C higher than without deformation. It means that all the structure domains in the CCT diagrams are shifted up by 30°C. The deformation induced by the hot rolling mills is approximately 70%, whereas all the dilation curves have been obtained without any strain. In order to match ROT conditions, all the dilation curves must then be shifted by 30°C. This assumption is made in order to increase the accuracy of the model, but a study on the influence of the pre-strain on the CCT diagram has to be done to confirm and refine this assumption. The transformation then starts at a higher temperature, which results in a lower fraction of untransformed austenite predicted by the model. The results are presented in Figure 5-14.

For both positions, the amount of untransformed austenite at the end of the ROT is less important than without the pre-strain consideration. With this approach, approximately 95% of the austenite has been transformed into ferrite and bainite. This shows the influence of the deformation of the steel on the predicted volume fractions. The volume fractions at the end of the ROT for both the centerline and quarter position are presented in Table 5-1. The volume fraction of ferrite is not affected by the strain for both positions. However, with strain the volume fraction of bainite is more important and the amount of retained austenite at the end of the transformation smaller. The strain consideration gives more realistic results comparing with the literature, and as it is going to be confirmed in the next section.

A drawback of the model is that the formation of pearlite is not considered. The whole model is based on the study of the first large bump in the dilation curves. It has been showed that this bump characterizes the apparition of ferrite and bainite. Thus, when the fraction transformed is calculated with the lever rule, it corresponds to the fraction of austenite transformed into ferrite and bainite. When this fraction reaches 100% it means that all the ferrite and bainite has been formed, but it does not mean that 100% of the

austenite has been transformed. There could still be some austenite left that will be transformed into pearlite or kept as retained austenite once the transformation of ferrite and bainite is complete. Thus, this model calculates only the volume fraction of ferrite compared to bainite. A way to improve the model will be to find a way to include the formation of pearlite in the transformation of austenite.

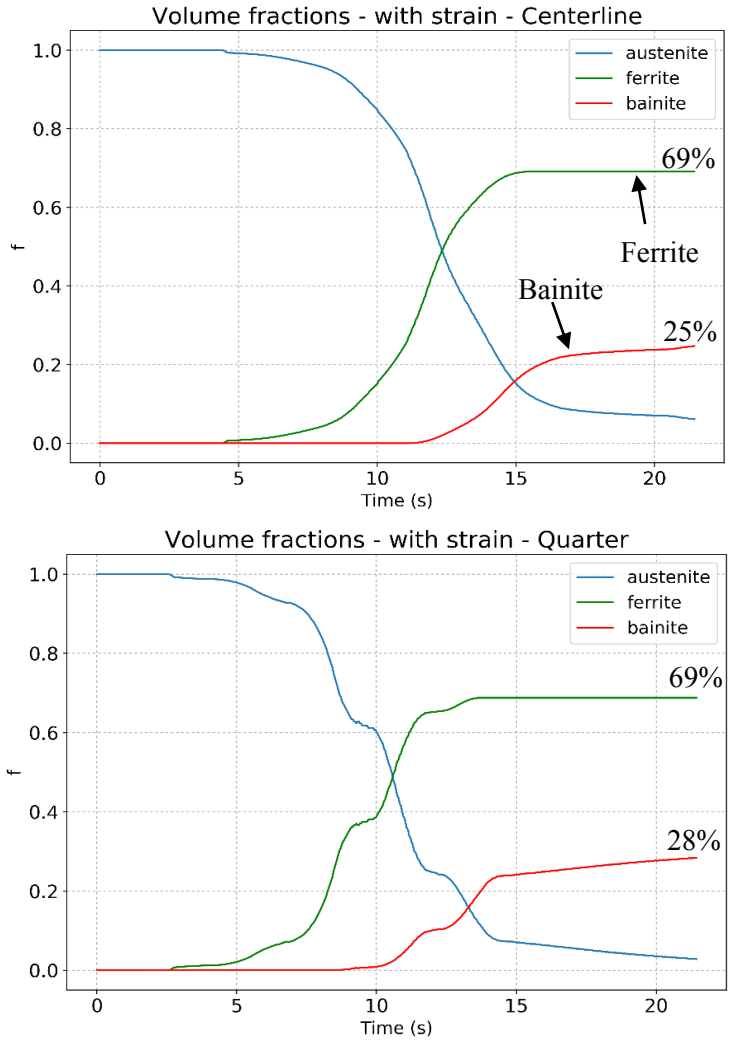


*Figure 5- 14: Scheil's additivity rule applied with the shifted transformation temperatures.*

*Table 5- 2: Comparison between the volume fractions obtained without and with strain considerations at the centerline and quarter of the skelp for the X70-A steel.*

| | Centerline | | Quarter | |
|---|---|---|---|---|
| | Without strain | With strain | Without strain | With strain |
| Ferrite | 69% | 69% | 69% | 69% |
| Bainite | 17% | 25% | 23% | 28% |
| Undetermined | 14% | 6% | 8% | 3% |

## 5.2. Experimental validation of the microstructure model prediction

As part of the thermo-metallurgical model, it is assumed that there is only austenite in the steel after the finish rolling. This might not be the case, because the thermodynamics predicts the presence of ferrite at this temperature and composition. Thus, it is assumed that due to kinetic arguments the steel comprise no ferrite before being cooled in the ROT.

The final volume fractions of ferrite and bainite predicted by the model can be read in Table 5-2. In order to confirm these results, a microstructure analysis has been performed on a pipe sample provided by Evraz. The composition of the X70 steel, the thickness of the skelp and the configuration of the ROT are the same that were described in the thermal model.

For the microstructure analysis, three samples at three different locations were studied using optical microscopy. The samples were taken at the surface of the outer diameter, at the centerline and in between the two locations, as presented in Figure 5-15. The three samples were then mechanically polished and etched with a LePera etchant [29]. This etchant consists of a 1% aqueous solution of sodium metabisulfite and 4% picric acid in ethanol. The advantage of this etchant is that it colors the different structures. Under the optical microscope the bainite will be dark brown/black, whereas the ferrite will be yellow and the martensite will appear almost white, as it can be seen in Figure 5-16.

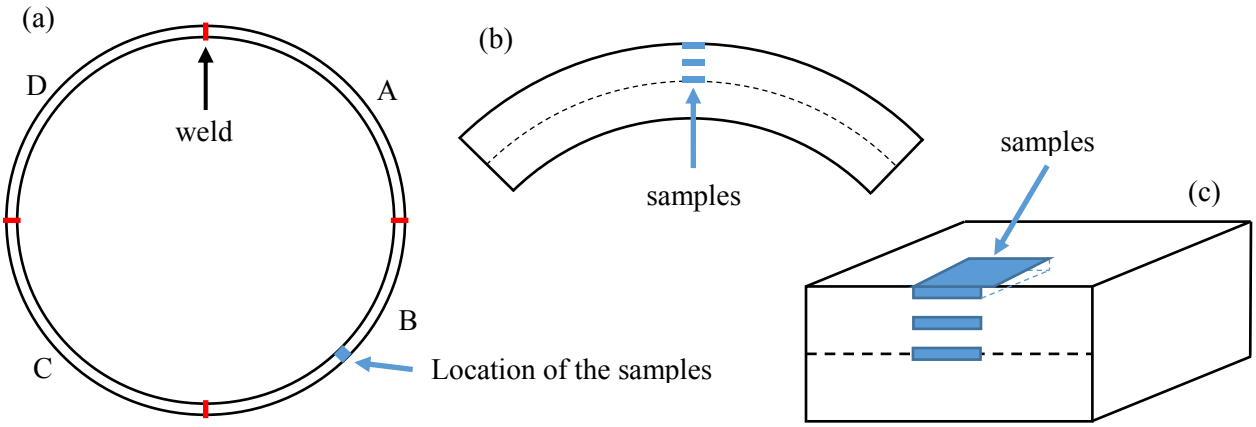


*Figure 5- 15: Location of the samples. (a) Schematic of the pipe. (b) Schematic of the quarter of the pipe B. (c) Schematic of part of the pipe where the samples are taken.*

In order to determine the volume fraction of each structures, the micrographs were processed with the same technique used in Section 4.5.2. In this case, several micrographs were taken at different locations in order to minimize the error on the experimental measurement. Figure 5-17 presents the comparison between the experimental and theoretical structure fractions.

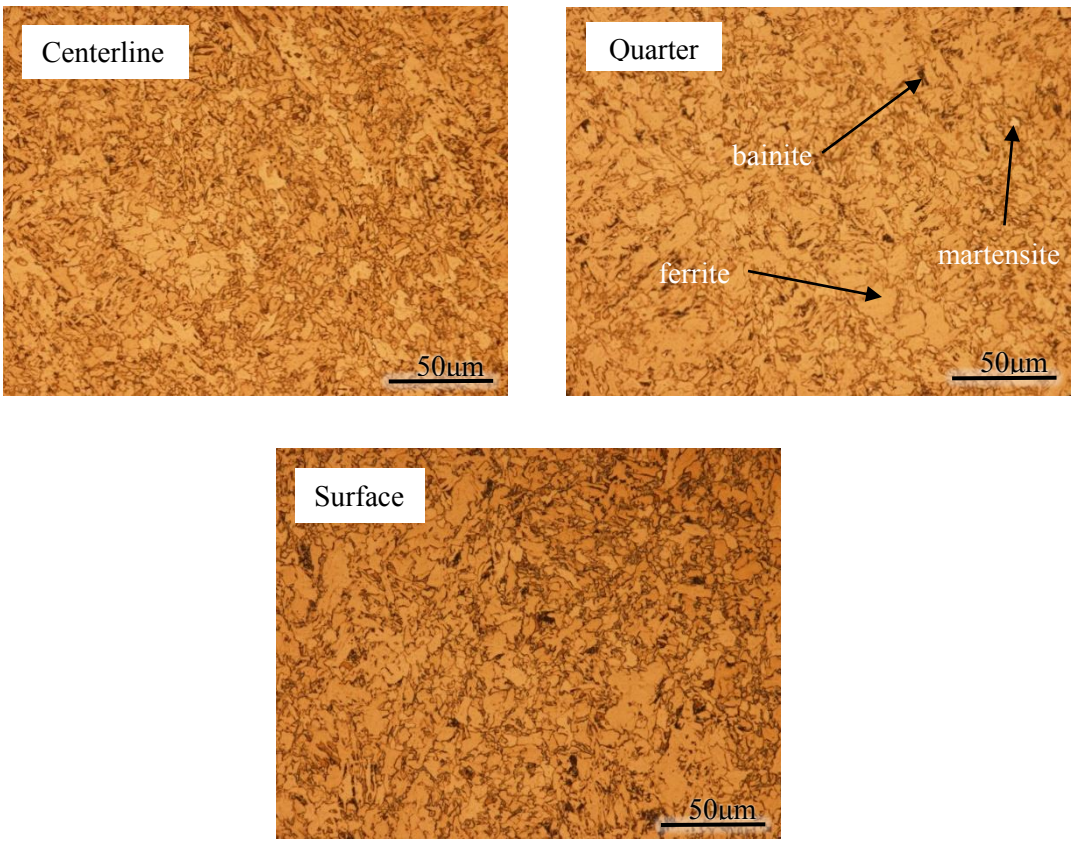


*Figure 5- 16: Micrographs of an X70 pipe samples at three different locations, mechanically polished and etched with LePera etchant.*

The results of the model are in relatively good agreement with the experimental measurement. However, it appears that the model tends to underestimate the volume fraction of ferrite compared to the experimental values. The undetermined part will mostly be bainite, because the formation of ferrite is almost over, as explained above. The experimental results shows that there is not a significant difference in the microstructure between the centerline and the quarter position of the pipe, and this trend is confirmed by the model. The bainite content is higher near the surface, but unfortunately, no theoretical results for this location are available due to the model restriction.

However, these results can be considered as a semi-quantitative comparison since the experimental volume fraction is quite difficult to estimate accurately. The predicted volume fractions were obtained with only four different dilation curves (corresponding to four cooling rates) and the highest cooling rate was 10°C/s, whereas for ROT cooling it is usually more around 20°C/s. Thus, the model tends to underestimate the cooling rate of ROT cooling. A way to overcome this issue is to obtain dilation curves for as many cooling rates as possible. Ideally, these cooling rates would cover the whole range of cooling

rates that the steel undergoes during ROT cooling. Nevertheless, despite all these weaknesses, it appears that the model gives consistent results with the experimental measurements.

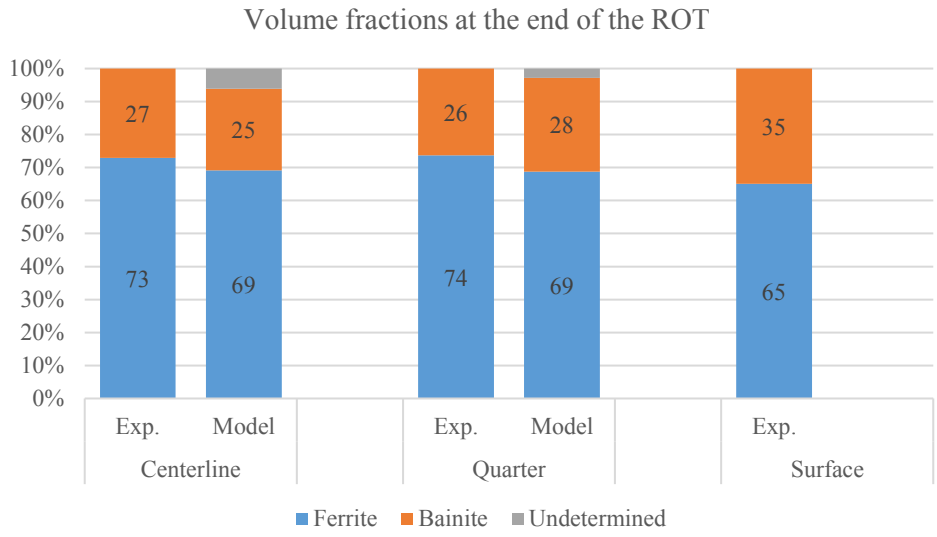


*Figure 5- 17: Comparison between the experimental and predicted volume fractions at different locations.*

## 5.3. Other steels

To test the reliability of the thermo-metallurgical model, it was then applied to the two other steels considered in this work (i.e. X70-B and X80 steels). These two steels do not have the same composition as the Evraz X70 steel used in the ROT (or even the same grade for one of them), but it will test the consistency of the model regarding different compositions and grades.

### 5.3.1. Evraz steel – X70-B

This steel has already been described in Section 4.6.1. To apply the thermo-metallurgical model to this specific steel (i.e. Evraz X70-B), the fraction transformed curves, calculated with the metallurgical model and associated with this steel, were used. For this steel, the evolution of the fraction transformed for five different continuous cooling are available. The temperature profile used in this section corresponds to the ROT configuration and was determined by the thermal model. As mentioned previously, the cooling rate at the centerline at the middle oscillates around 15°C/s. With the previous steel (Evraz X70-A steel) dilation data only for cooling rates under 10°C/s was available, which led to an underestimation of the overall cooling rate of the ROT. However, in this case, the evolution of the fraction of austenite transformed has been predicted for 1, 3, 10, 30 and 40°C/s. Thus, the cooling rate of

the ROT can be estimated more accurately. Instead of putting a threshold arbitrarily between the different values of cooling rates, the thresholds were manually adjusted to approach at best the mean cooling rate of the run-out table. Figure 5-18 illustrates this principle for the cooling rate at the centerline and the quarter nodes. The average cooling rate at the centerline and the quarter are respectively 9.8 and 9.7°C/s. The approximation of the ROT cooling rates is made in order to keep the same average value for both positions.

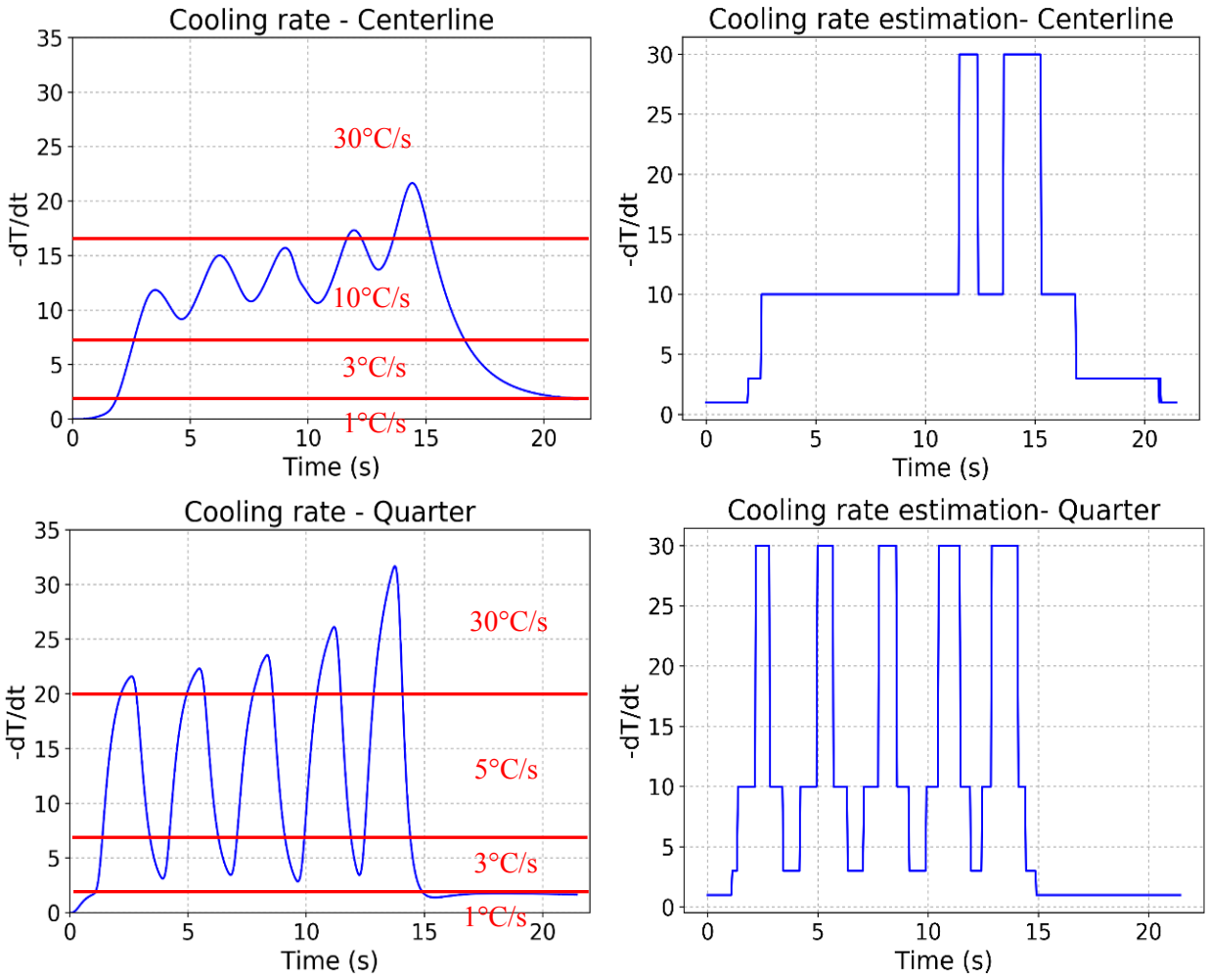


*Figure 5- 18: Cooling rate of ROT cooling at the centerline and quarter node (left) and their approximations for the Evraz X70-B steel (right).*

The Scheil additivity rule is then applied at the centerline and quarter positions. The results are presented in Figure 5-19. As mentioned previously, these results have been obtained while considering the pre-strain of the skelp induced by the finish rolling. A simulation without strain, results in an unfinished transformation of austenite. However, even with this consideration, it appears that the

transformation is not complete at the end of the ROT. This can be explained by the CCT diagram presented in Figure 5-20. Compared to the steel studied previously (i.e. X70-A steel) the transformation of austenite starts at a much lower temperature for the X70-B steel (approximately 40°C lower) and the transformation happens over a range of approximately 200°C. A lower starting temperature leads then to a higher amount of untransformed austenite.

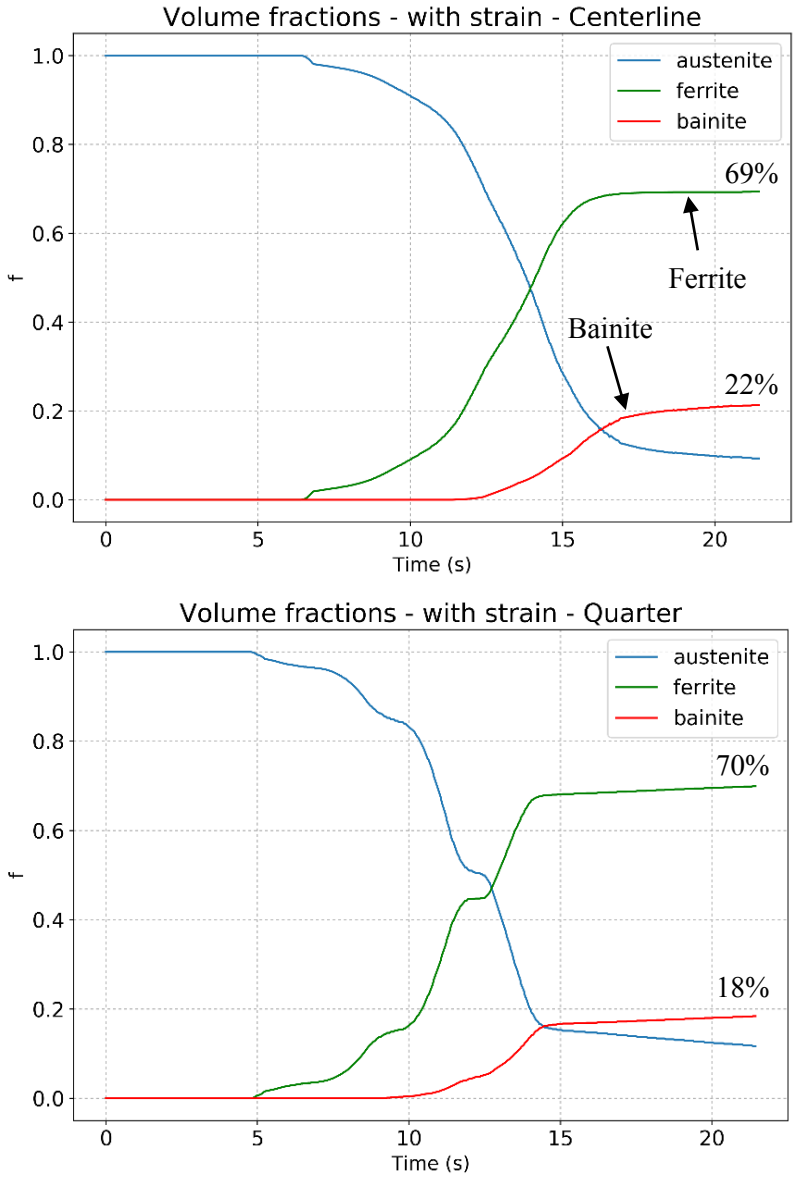


*Figure 5- 19: Evolution of the volume fractions during ROT cooling for the Evraz X70-B steel at the centerline and quarter.*

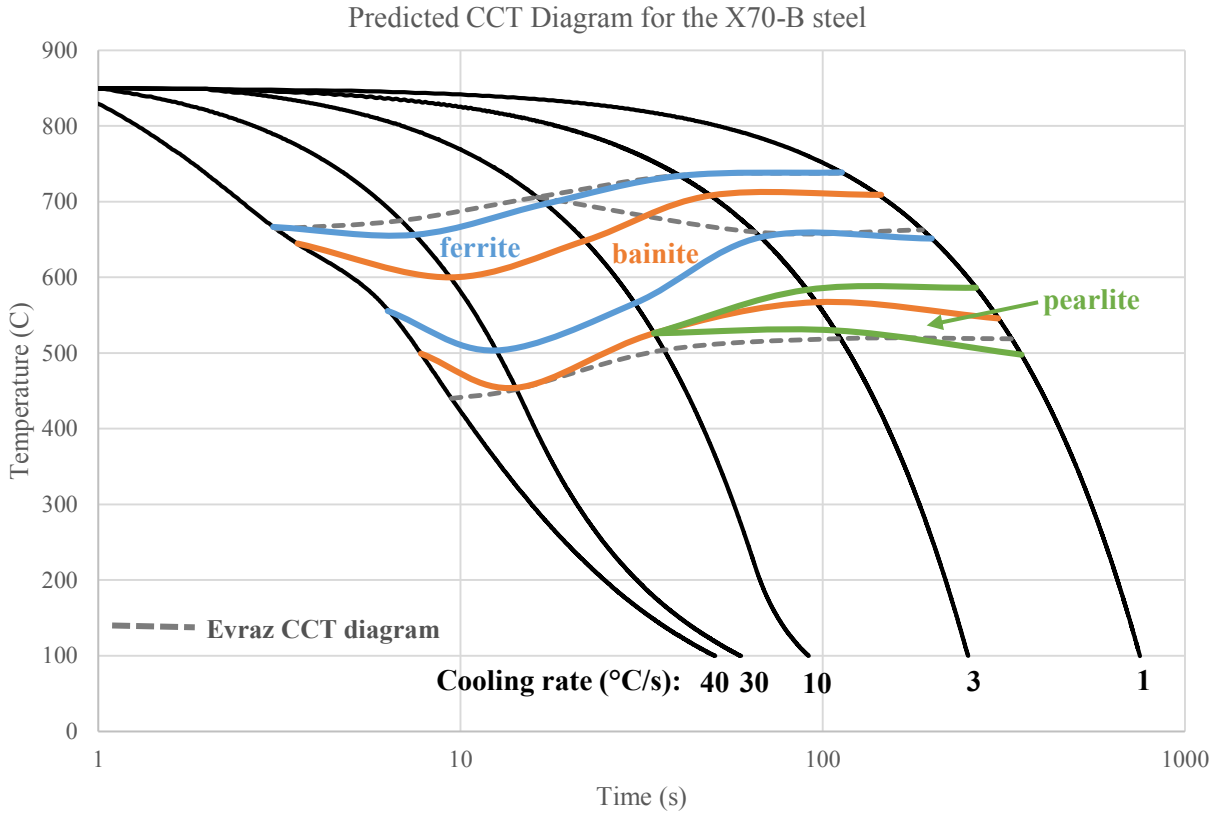


*Figure 5- 20: CCT diagram predicted by the model using the "three structures approach" for the Evraz X70-B steel.*

The experimental and predicted volume fractions for the X70-B steel are compared in Figure 5-21. This comparison can be made since the composition of the Evraz X70-B steel is close to the one used in the ROT. The amount of ferrite predicted by the model is very close from the experimental one. Looking at the evolution of ferrite in Figure 5-19 it looks like the volume fraction of ferrite has reached a steady state and will not increase much more. Thus, the undetermined volume fraction can be assumed to be bainite, which will result in a good prediction of the model compared to the experimental volume fractions.

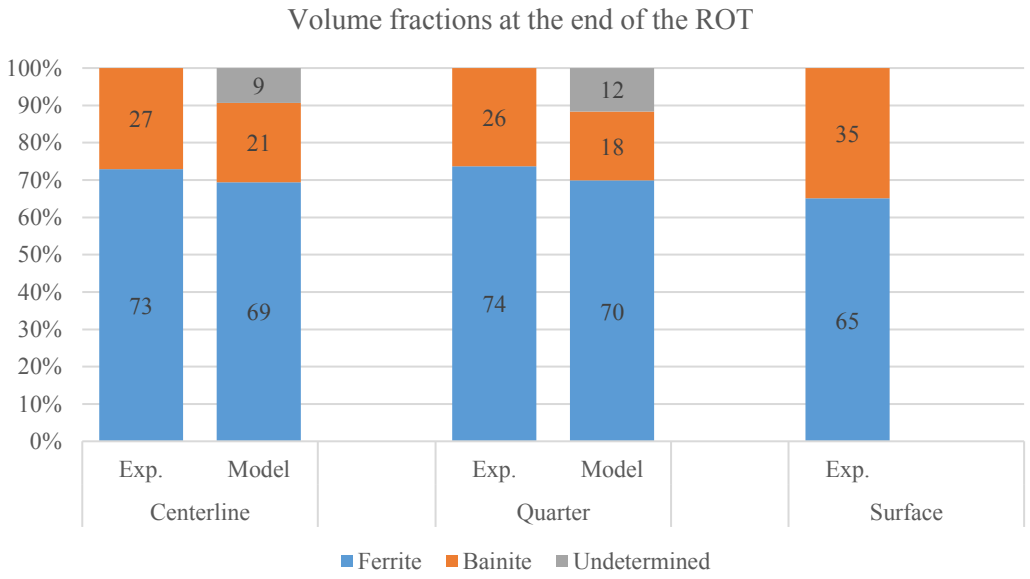


*Figure 5- 21: Comparison between the experimental and predicted volume fractions at different locations for the Evraz X70-B steel.*

For the X70-B steel, the cooling rate of the ROT can be approximated more accurately than with the previous dilation dataset, from the Evraz X70-A steel. However, for this composition the transformation of austenite starts at a lower temperature. This impacts the model, which is unable to predict the nature of 10% of the transformed austenite. This issue can be overcome with a more accurate study on the influence of the deformation on the starting transformation temperature or by using another ROT setup that will lead to a full transformation of the austenite (i.e. with a lower coiling interrupt temperature, and thus, a larger temperature range).

### 5.3.2. Canmet – X80 steel

The model will be tested on an X80 steel, which is described in Section 4.6.2. Even though the steel is different from the one used in the ROT, it is interesting to see how this steel composition will affect the model prediction.

The cooling rate of the ROT is approximated with the same approach as for the Evraz X70-B steel. The repartition of the cooling rates is presented in Figure 5-22.

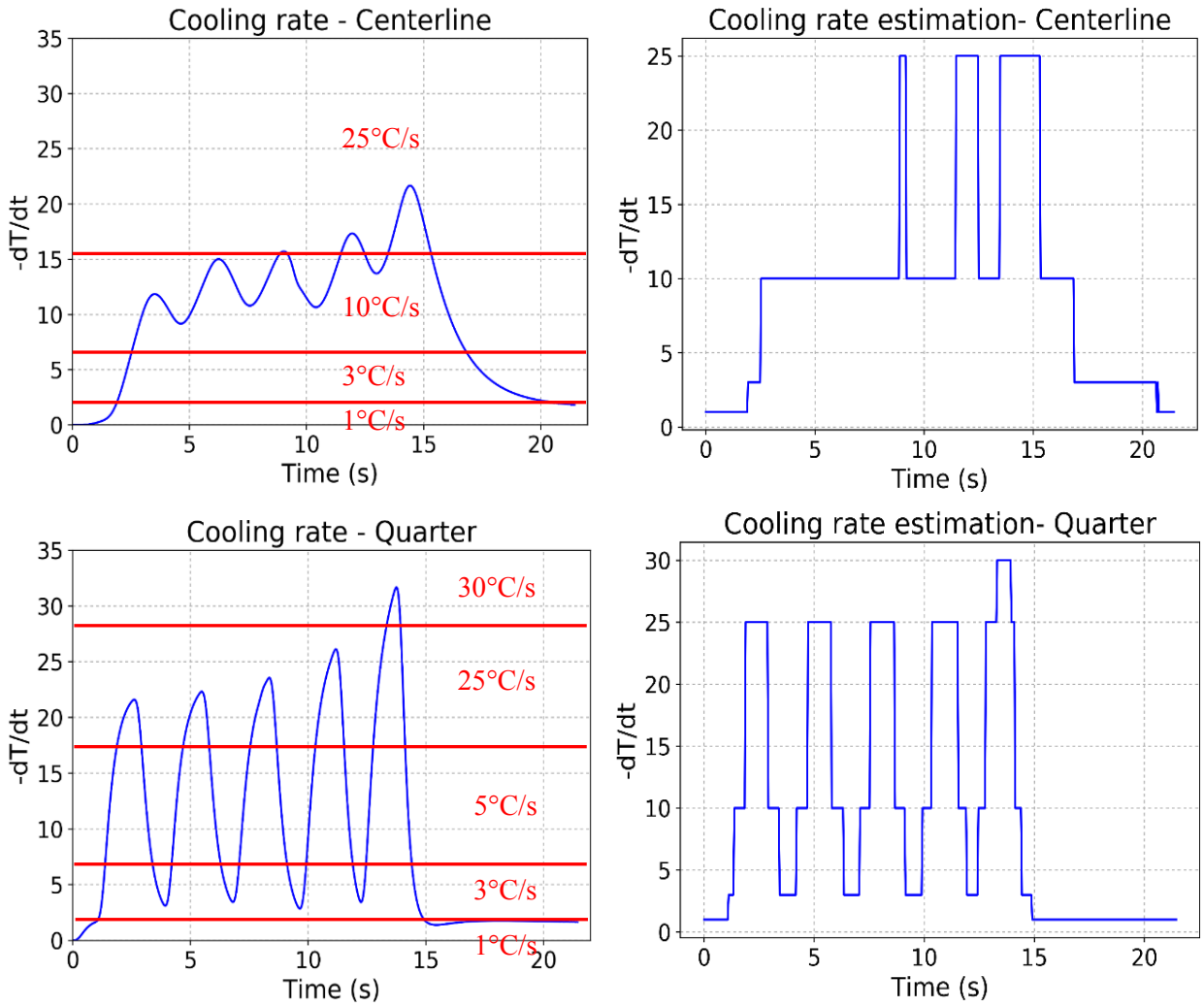


*Figure 5- 22: Cooling rate of ROT cooling at the centerline and quarter node (left) and their approximations for the X80 steel (right).*

The evolution of the volume fractions is presented in Figure 5-23. The transformation of austenite is not complete at both locations. Only 80% of the austenite has been transformed at the centerline and at the quarter of the pipe. In order to reach a fraction of austenite transformed similar to the X70 steels, the CCT diagram would need to be shifted by at least 100°C. It would mean that the deformation induced by the finish rolling has a great impact on the beginning of the transformation. This can only be confirmed by a further study of this effect. Another explanation could be that the configuration of the ROT does not suit this type of steel. In order to fully transform the austenite, this steel needs to be cooled down at a lower temperature than 575°C. According to the model, the transformation starts at 694°C and the temperature range, over which the transformation happens, is approximately 200°C. Thus, this steel needs to be cooled down at a temperature lower than 500°C, in order to transform most of the austenite.

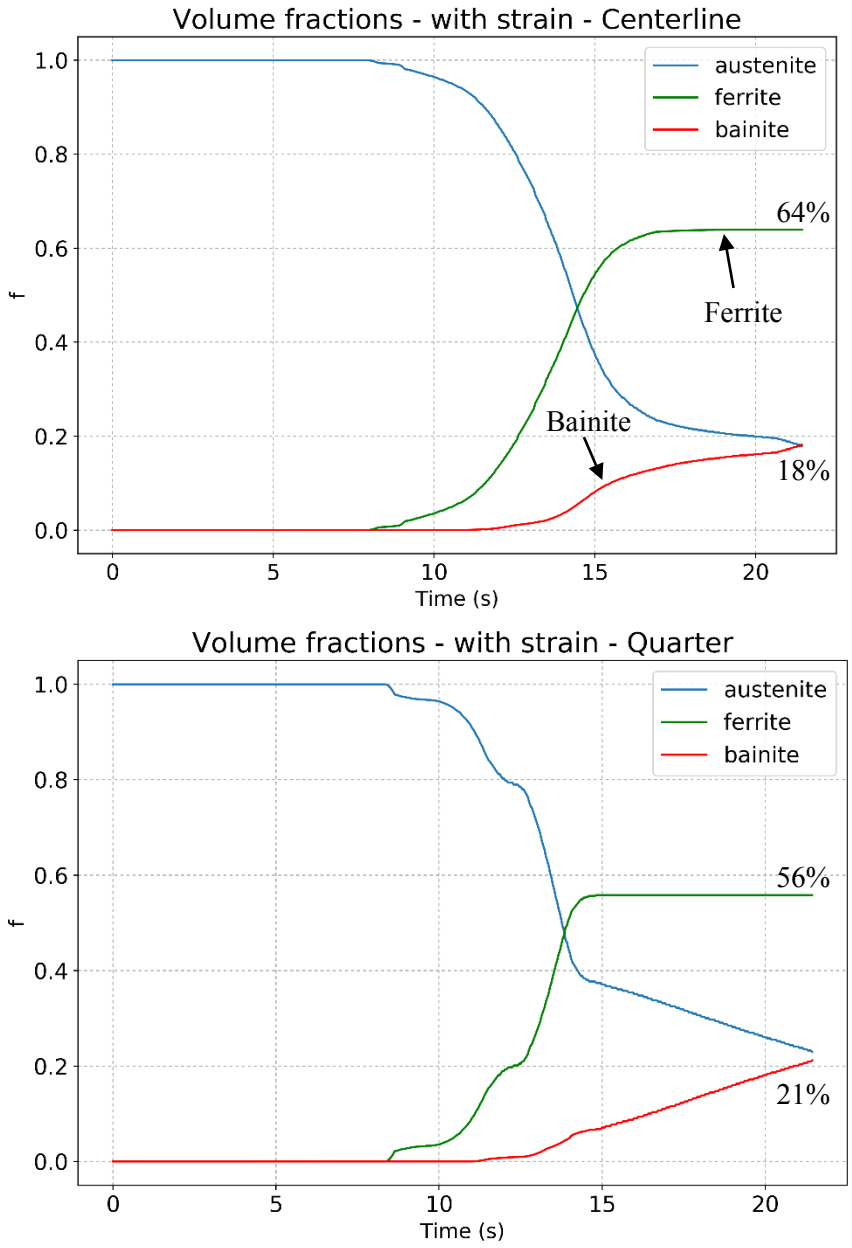


*Figure 5- 23: Evolution of the volume fractions during ROT cooling for the X80 steel at the centerline and quarter.*

The final volume fractions predicted by the model are presented in Figure 5-24. They are not compared to the experimental results since they do not concern the same steel.

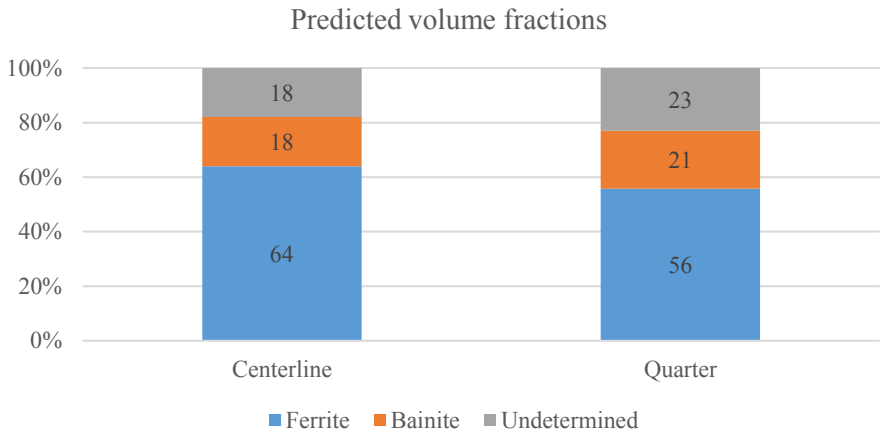


*Figure 5- 24: Volume fraction predicted for ROT cooling at the centerline and quarter of the X80 skelp.*

## 5.3. Application of the model

In this section, the model will be tested for two different positions (i.e. centerline and quarter) as well as with the three different steels presented previously, and on four other ROT configurations: late and early cooling, and high and low CIT.

### 5.3.1. Comparison of the model results at two different positions

The thermo-metallurgical model has been applied in Section 5.1 at two different positions of the skelp: at the centerline and quarter. The microstructure of these two positions will now be compared in order to determine if a difference of microstructure can be expected through the thickness of the skelp. This analysis will be done for the two X70 steels, because the results can be compared to the experimental measurements.

The results are presented in Table 5-3. The predicted volume fractions of the X70-A and X70-B steels are relatively similar between the centerline and quarter of the skelp. The experimental measurement tends to confirm this observation, it appears that the volume fractions are similar for these two positions. However, a slight difference can be noticed for the bainite volume fraction for the X70-A and X70-B steel.

This similarity between the centerline and the quarter of the skelp can be explained looking at the CCT diagrams. An important factor in the determination of the volume fractions, is the temperature range of phase transformations that can be observed on CCT diagram. The results will be discussed with the predicted CCT diagram for the Evraz X70-A steel but similar observations can be made on the other CCT diagrams.

*Table 5- 3: Comparison of the volume fractions between the centerline and quarter of the skelp for three steels.*

| | X70-A | | X70-B | | X70-ROT-measured | |
|---|---|---|---|---|---|---|
| | Centerline | Quarter | Centerline | Quarter | Centerline | Quarter |
| Ferrite | 69% | 69% | 69% | 70% | 73% | 74% |
| Bainite | 25% | 28% | 22% | 18% | 27% | 26% |
| Undetermined | 6% | 3% | 9% | 12% | 0% | 0% |

The structure domains determine the temperature range, over which the formation of ferrite, bainite and pearlite will occur. Looking at the ferrite domain in Figure 5-25, it appears that ferrite forms over the same range of temperature for 3, 5 and 10°C/s. The temperature range for 1°C/s is a bit smaller but, as shown previously, most of the transformation occurs at higher cooling rates. Since the temperature ranges over which ferrite is formed is similar for the three cooling rates, then even if the evolution of the volume fraction of ferrite is different, it will result in the same volume fraction at the end of the ROT. This explains why the ferrite fraction does not change between the centerline and the quarter of the skelp. The same observation can be made for bainite, except with the temperature range for 10°C/s, which is smaller and can explain the slight difference in bainite volume fraction between the centerline and the quarter position.

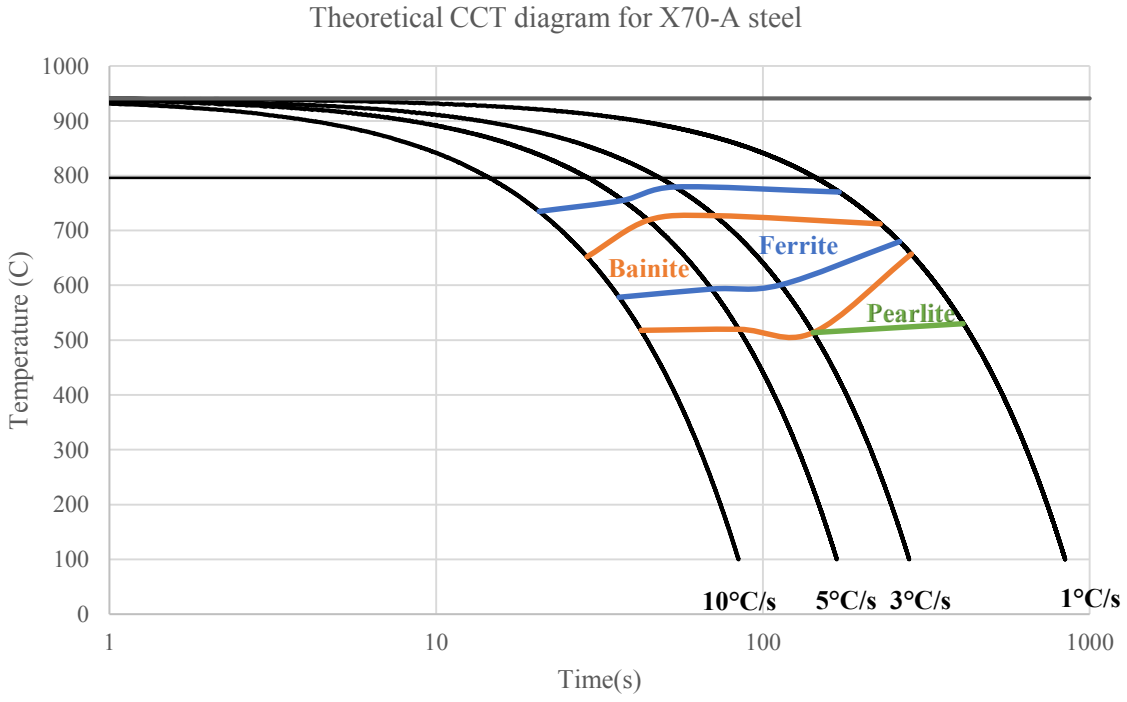


*Figure 5- 25: CCT diagram predicted by the model for the Evraz X70-A steel.*

These observations are also not surprising, since the temperature profile at the centerline and quarter are quite similar. However, as mentioned previously, the cooling rate at the surface is completely different and must affect the microstructure. This is confirmed in Table 5-4, where the experimental measurement of the X70 steel used in the ROT are presented. The volume fractions at the surface differs from the centerline and the quarter, which shows that cooling rate can have an impact on the microstructure.

*Table 5- 4: Volume fractions measured at the end of the ROT at three different positions.*

| | X70-ROT-measured | | |
|---|---|---|---|
| | Centerline | Quarter | Surface |
| Ferrite | 73% | 74% | 65% |
| Bainite | 27% | 26% | 35% |

### 5.3.2. Application of the model on three different steel compositions

The volume fractions at the end of the ROT have been determined previously for two X70 and one X80 steels and for the same ROT configuration. They are presented and also compared to the volume fractions measured experimentally on a pipe sample in Figure 5-26.

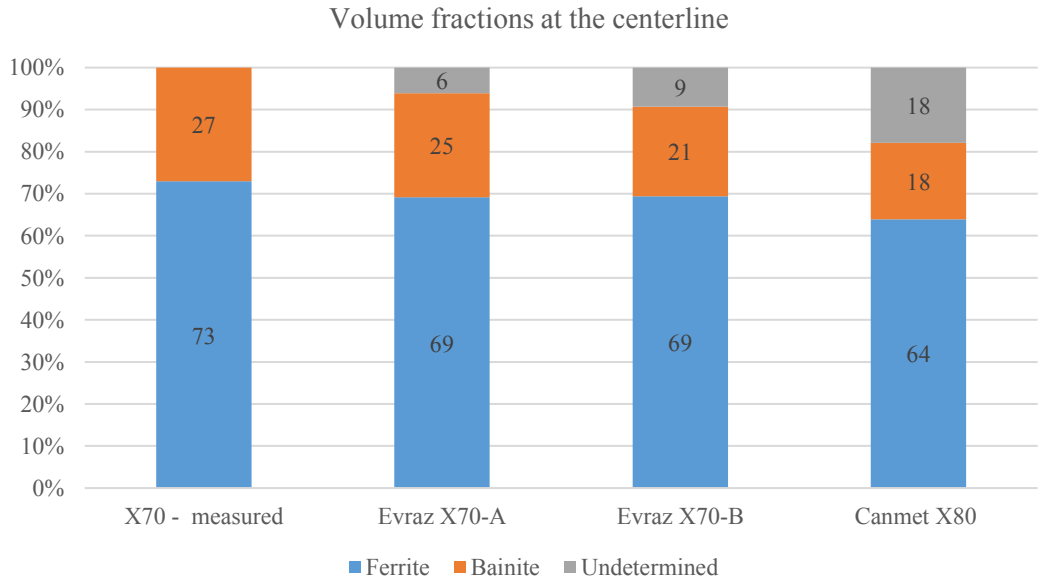


*Figure 5- 26: Volume fractions at the centerline measured experimentally and predicted for three different steels for ROT cooling.*

The volume fraction of ferrite and bainite is similar for the three X70 steels. It shows that the amount of ferrite predicted is consistent with the steel grade, and thus, it is not surprising to have different results for the X80 steel. The volume fraction of untransformed austenite is more important for the Evraz X70-B than for the Evraz X70-A steel. It is due to a lower starting transformation temperature for the X70-B steel. For the X80 steel, the important undetermined volume fraction is due to the same reason, but can also be explained by a poorer quality of the dilation curves.

### 5.3.3. Application of the model on different ROT configurations

In this section, the model will be run with four different ROT configurations that result in four different temperature profiles. First, the impact of an early and a late cooling will be tested. Then, the influence of a lower and a higher coiling interrupt temperature (CIT) will be compared to the results obtained with the ROT configuration described in the thermal model. The ROT configuration described previously in this thesis will be designated as "standard configuration".

#### *5.3.3.1. Early and late cooling*

The first two ROT configurations result in the same CIT as the standard configuration. The difference is that the first one corresponds to an early cooling and the second one to a late cooling, as presented in Figure 5-27.

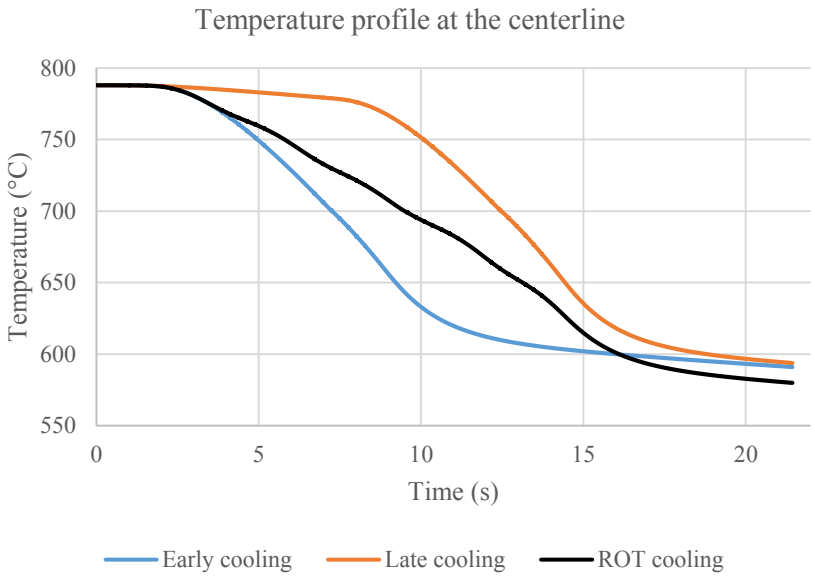


*Figure 5- 27: Temperature profiles at the centerline for three different ROT configurations with the Evraz X70 steel.*

For the early cooling, the steel is first cooled down at a higher cooling rate than with the standard configuration, followed by a low cooling stage. Conversely for the late cooling, the skelp undergoes a low cooling rate stage followed by a high cooling one. To achieve an early cooling, the ROT cools down the strip with only the first three water banks and without using the side sprays. The vapor film stays on top of the skelp between the water banks, which results in a more effective cooling. For the late cooling, the first two water banks are turned off and the three next are turned on. For this configuration the side sprays are also turned off between the water banks.

The results of the predicted volume fractions for the three configurations is presented in Figure 5-28. No noticeable difference can be observed for these three ROT configurations. It can be explained by the underestimation of the ROT cooling rate. For the Evraz X70-A steel, the dilation dataset with the highest cooling rate available is 10°C/s. Thus, the impact of the highest cooling rates induced by the early and late cooling cannot be observed in the model results. In order to see a difference in the predicted microstructure, the model requires dilation datasets with higher cooling rates, as it is the case with the Evraz X70-B steel.

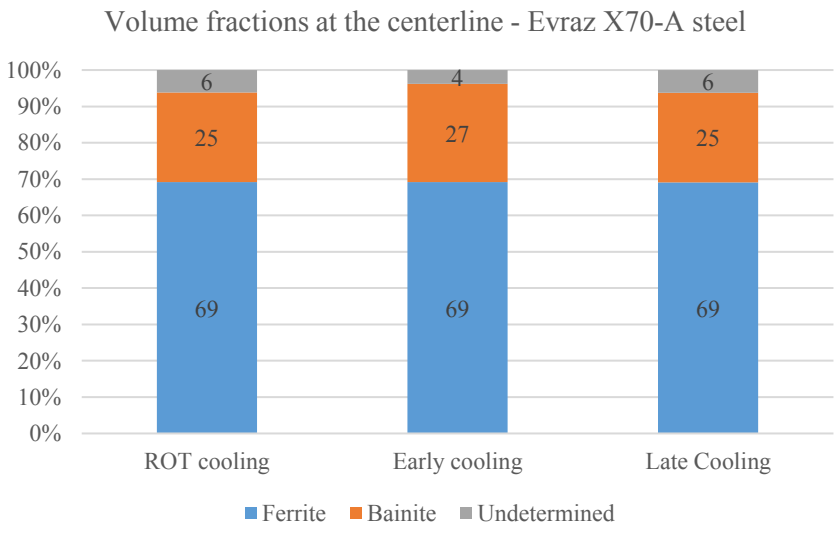


*Figure 5- 28: Volume fractions at the end of the ROT for the Evraz X70-A steel and for three different ROT configurations.*

The model has then been tested with these three configurations and the dataset from the Evraz X70-B steel. For this steel data for 30 and 40°C/s are available, which allows a better approximation of the cooling rate, and thus, the microstructure. The results are presented in Figure 5-29. Both the early cooling and late cooling result in almost the same volume fraction of ferrite as with the standard ROT

configuration. However, for these two configurations more untransformed austenite at the end of the ROT is predicted. On the fraction transformed curves in Figure 5-30, it appears that for both configurations, most of the transformation happens during the high cooling rate stage. Thus, a slow cooling leads to a slower transformation rate. It seems that for different configurations of the ROT the steadier the cooling rate is, the greater the transformation rate of austenite will be.

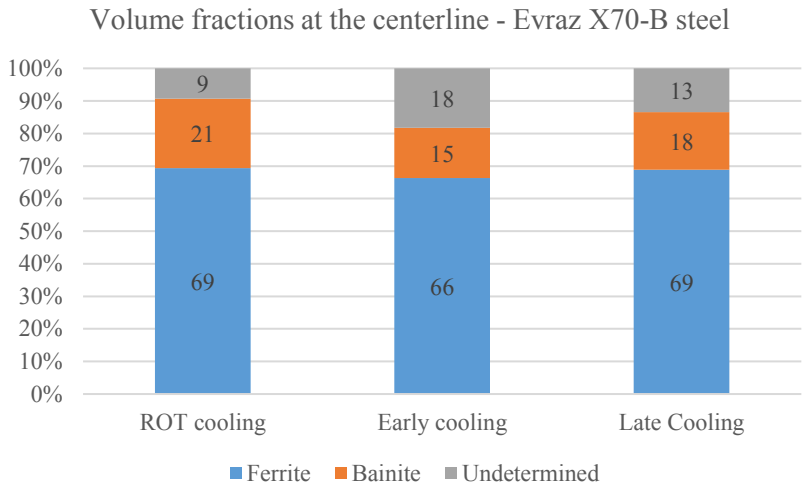


*Figure 5- 29: Volume fractions at the end of the ROT for the Evraz X70-B steel and for three different ROT configurations.*

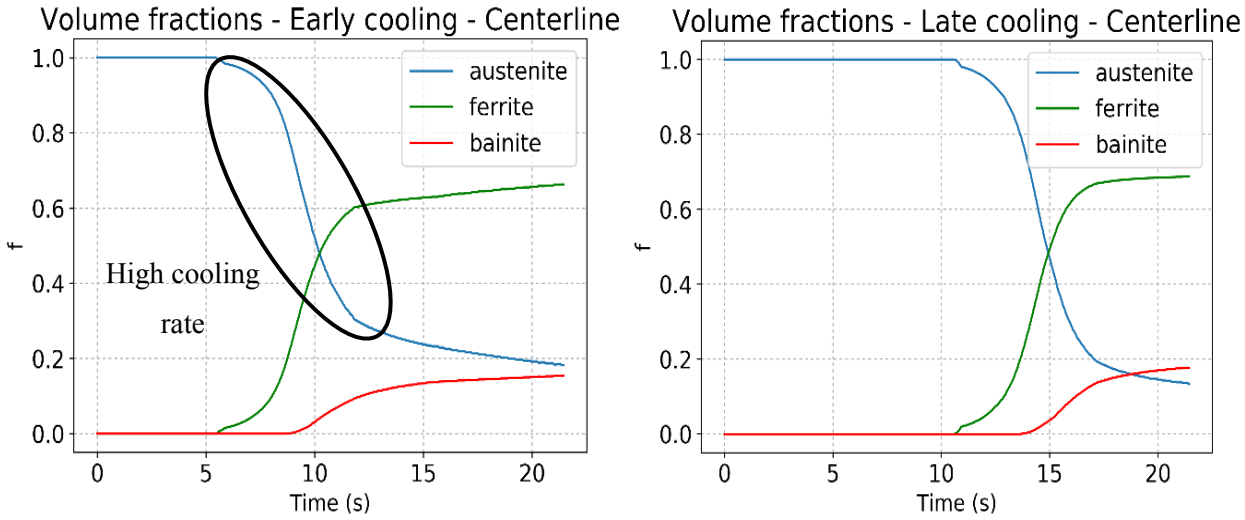


*Figure 5- 30: Evolution of the volume fractions at the centerline for an early and late cooling configuration for the Evraz X70-B steel.*

#### *5.3.3.2. High and low CIT*

The simulation has been run for two other ROT configurations with the Evraz X70-A steel, whose temperature profiles are presented in Figure 5-31. For the first one, only three water banks are turned on, as well as the side sprays in between. The temperature profile follows the beginning of the one obtained with the standard ROT configuration. The temperature of the skelp is then only driven by radiative cooling, which leads to a higher CIT. The overall cooling rate of this transformation is much lower than with the standard ROT configuration. For the second configuration, the first five water banks are turned on but the side sprays are turned off. The cooling of the skelp is more efficient than with the standard configuration, which leads to a lower CIT and a greater overall cooling rate.

The predicted volume fractions for the Evraz X70-A steel are presented in Figure 5-32. For the low CIT configuration, 98.8% of the austenite have been transformed and the ferrite volume fraction is similar to the one obtained with the standard configuration. For the high CIT configuration, approximately 60% of the austenite has been transformed and mostly into ferrite. According to the CCT diagram presented in Chapter 4, the transformation of austenite happens over a range of temperature of approximately 200°C. On one hand, the low CIT configuration results in a high transformation rate. On the other hand, the cooling of the high CIT configuration is too small for the austenite to fully transform into ferrite or bainite and results in a high volume fraction of untransformed austenite.

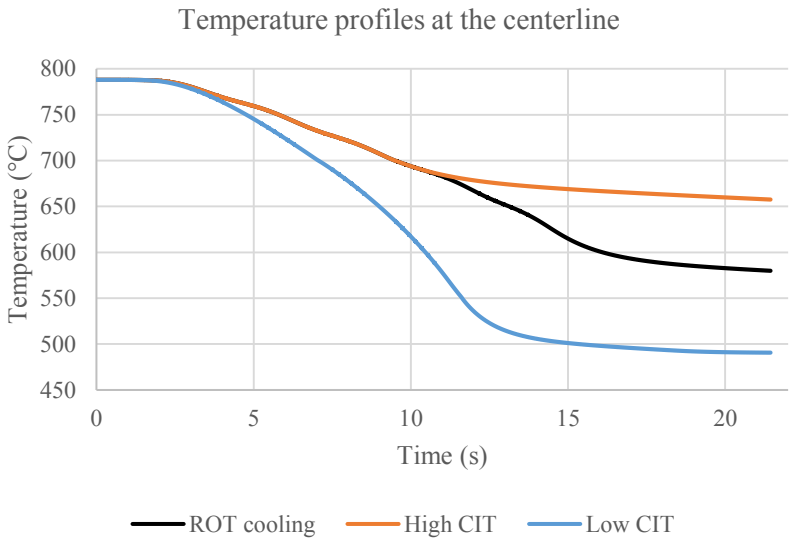


*Figure 5- 31: Temperature profile at the centerline for three different ROT configurations.*

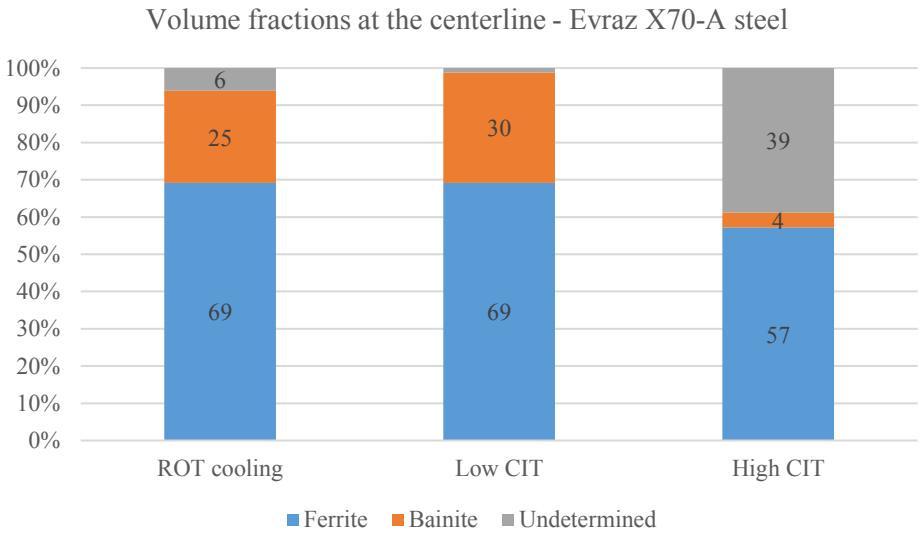


*Figure 5- 32: Volume fractions at the end of the ROT for the Evraz X70-A steel and for three different ROT configurations.*

These two configurations have then been tested for the X80 steel. The results are presented in Figure 5-33. As expected the transformation rate is higher for the low CIT configuration than with the standard one. The effect of the high CIT configuration on the transformation rate is enhanced compare to the standard configuration. It confirms the fact that in order to increase the transformation rate, the cooling has to cover a certain range of temperature dictated by the CCT diagram.

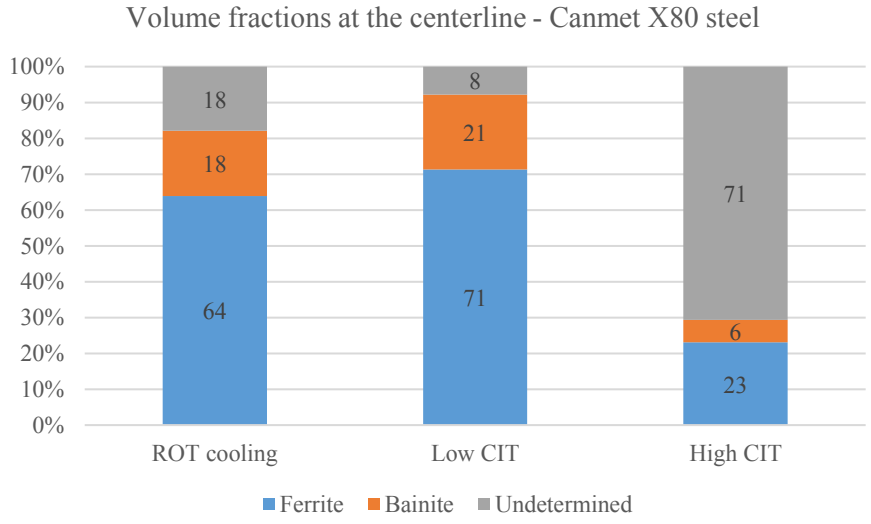


*Figure 5- 33: Volume fractions at the end of the ROT for the X80 steel and for three different ROT configurations.*

## 5.4. Thermo-metallurgical model summation

The thermo-metallurgical consists in combining the microstructure predictions from the metallurgical model with ROT cooling obtained with the thermal model, in order to predict the microstructure at the end of ROT cooling. The model:

1) Predicts the evolution of the fraction of austenite, ferrite and bainite during ROT cooling
2) Accurately calculates the volume fractions of austenite, ferrite and bainite at the end of ROT cooling
3) Shows that strain considerations leads to a more accurate prediction of the steel microstructure
4) Is able to predict the microstructure with different steels and ROT configurations

However, the thermo-metallurgical model has also shown some weaknesses:

1) The model is unable to predict the microstructure at the surface of the skelp due to high values of cooling rates
2) The Scheil's additivity rule impose that the model relies more on the temperature range of cooling than the cooling rate. Contrarily to the high and low CIT considerations, early and late cooling considerations have shown no difference in the microstructure at the end of ROT cooling

# Chapter 6: Conclusions & Future Work

## 6.1. Conclusions

The objective of this thesis was to predict the effect of ROT cooling on the microstructure of a thick walled X70 steel. To achieve this objective three different models have been developed. The thermal model predicts the temperature of the skelp, and the metallurgical model characterizes phase transformations during continuous cooling. These two models are then combined in order to predict the volume fractions of austenite, ferrite and bainite at the end of the ROT.

For the thermal model, the finite element thermal analysis developed by Wiskel et al. [10] has been modified to predict the temperature history of a thick walled (i.e. 17.3mm) X70 steel. The model seems to accurately predict the CIT at the end of the ROT. The model has been validated by measuring the CIT for two different ROT configurations. Additionally, the heat transfer model used in the FE analysis has been widely used in the literature. Thus, even without experimental validation, it seems that the thermal model can be confidently used to accurately predict the thermal history during ROT cooling.

In order to characterize the microstructure of the steel at the end of the ROT, a metallurgical model has been developed to predict the evolution of volume fractions during continuous cooling. This model is based on a modified form of the Avrami equation and a new approach that was developed to consider the simultaneous formation of different structures. The metallurgical model is able to predict the evolution of the fraction of austenite transformed as well as the volume fractions of austenite, ferrite and bainite at the end of continuous cooling. However, the formation of pearlite, which occurs after the simultaneous formation of ferrite and bainite, is not considered by the model. With this model, classical CCT diagrams found in the literature can be improved by considering the phase formations, no more sequentially but simultaneously.

The thermal and metallurgical model were then combined with Scheil's additivity rule in order to predict the evolution of the volume fractions during ROT cooling. This thermo-metallurgical shows promising results in predicting the volume fractions at the end of ROT cooling for different locations of the skelp, as well as for different steels and ROT configurations. It appears that a key point of the model is the temperature range, over which the phase transformation occurs. Thus, for different configurations with the same CIT, the model does not predict any difference in terms of volume fractions, whereas the larger the temperature range is, the higher the transformation rate will be. The model was able to predict the microstructure at different locations of the skelp, and is has been shown that there are no noticeable difference between the centerline and the quarter of the skelp. However, the microstructure at the surface of the strip cannot be predicted by the model due to a large range of cooling rates.

## 6.2. Future work

The three models developed in this thesis show good results, but need to be improved and further validated in order to be more accurate. The validation can be done by experimental measurements or by using the model with other steels (i.e. different composition or grade), ROT configuration, etc.

For the thermal model:

- Extend the model to other steel compositions and grades, skelp thicknesses and ROT configurations in order to be able to confidently use the thermal model in different situations.
- Perfect the model by adding consideration of the oxide layer that can form at the surface of the skelp as presented by Wiskel et al [10].
- Use the model to optimize ROT cooling in order to obtain a specific CIT and cooling rate. This will result in a better control of the steel microstructure at the end of the ROT. An optimization of ROT cooling has been done by Bineshmarvasti [35] and can be implemented in the model.

For the metallurgical model:

- Replicate the results with other steels, more dilation data and a more accurate microstructure analysis. This will validate the model and increase the accuracy of the model predictions.
- Perfect the model by including the formation of pearlite, characterized by a second rebound on the dilation curves.
- The two main assumptions of the metallurgical model were the simultaneous structure formation and the introduction of the parameter $\alpha$ to model the evolution of the ferrite and bainite volume fractions. These two assumptions are based on empirical observations, and thus, need to be confirmed analytically.

For the thermo-metallurgical model:

- The model needs to be improved with a more accurate estimation of the ROT cooling rate. Thus it requires to have more dilation data for various continuous cooling conditions.
- Develop the model with cooling and heating dilation curves to predict the microstructure at the surface of the skelp.
- Investigate different ROT configurations in order to optimize the steel microstructure at the end of ROT.

# References


[1]: T.Gladman. *The physical metallurgy of microalloyed steels.* The Institute of Materials, 1997.

[2]: A.Carboni, A.Pigani, G.Megahed & S.K.Paul. *Casting and rolling of API X70 grades for arctic applications in a thin slab rolling plant*, Millenium Steel, pages 131-136, 2008.

[3]: G.Krauss. *Steels. Processing, structure, and performance*. ASM International, 2015.

[4]: F.Xu. *Finite* element *simulation of water cooling process of steel strips on runout table,* PhD thesis in University of British Columbia, 2006.

[5]: S-X.Chen, J.Zou & X.Fu. *Coupled models of heat transfer and phase transformation for the run-out table in hot rolling*. Journal of Zhejiang University SCIENCE A, pages 932-939, 2008.

[6]: A.Mukhopadhyay & S.Sikdar. *Implementation of an on-line run-out table model in a hot strip mill*. Journal of Materials Processing Technology, pages 164-172, 2005.

[7]: A.Suebsomran & S.Butdee. *The Study of Cooling Process on Runout Table by Simulation Method*. IRSN Industrial Engineering, 2013.

[8]: A.Suebsomran & S.Butdee. *Cooling process on a run-out table by the simulation method*. Case Studies in Thermal Engineering, pages 51-56, 2013.

[9]: T.Myint-U & L.Debnath. *Linear partial differential equations for scientists and engineers.* Birkhauser, 2007.

[10]: J.B.Wiskel, J.Prescott & H.Henein. *Finite Element Thermal Analysis of Surface Cold Spots Observed during Infrared Video Imaging of a Moving Hot Steel Strip.* Conference paper, Quantitative InfraRed Thermography, 2014.

[11]: B.L.Bramfitt. *Metals handbook desk edition*. ASM International, second edition, 1998.

[12]: H-G.Hillenbrand, M.Graf & C.Kalwa. *Development and production of high strength pipeline steels*. Europipe, Niobium 2001, Orlando, USA.

[13]: J-C.Zhao & M.R.Notis. *Continuous cooling transformation kinetics versus isothermal transformation kinetics of steels: a phenomenological rationalization of experimental observations.* Materials Science and Engineering, pages 135-208, 1995.

[14]: K.Jonsson. *Modification of the stress-strain curve for high-strength line pipe steel.* MSc thesis in University of Alberta, 2013.

[15]: T.A.Kop, J.Sietsma & S.van der Zwaag. *Dilatometric analysis of phase transformations in hypo-eutectoid steels.* Journal of Materials Science, pages 519-526, 2001.

[16]: C.Liu, X.Di, C.Chen, X.Guo & Z.Xue. *A bainite transformation kinetics model and its application to X70 pipeline steel*. Journal of Materials Science, pages 5079-5090, 2015.

[17]: M.Avrami. *Kinetics of phase change. I General Theory*. The Journal of Chemical Physics, pages 1103-1112, 1939.

[18]: M.Avrami. *Granulation, Phase change, and microstructure kinetics of phase change.* The Journal of Chemical Physics, pages 177-184, 1941.

[19]: M.Umemoto, N.Komatsubara, I.Tamura, *Prediction of hardenability effects from isothermal transformation kinetics*. J. Heat Treating, Volume I, number 3, pages 57-64, 1980.

[20]: S.Serajzadeh. *Prediction of temperature distribution and phase transformation on the run-out table in the process of hot strip rolling*. Applied Mathematical Modelling, pages 861-875, 2003.

[21]: Y.Zhang, C.Mo, D.Li & Y.Li. *Modelling of phase transformation of plain carbon steels during continuous cooling*. J. Mater. Sci. Techno., Vol.19 No.3, pages 262-264, 2003.

[22]: M.Venkatraman, O.N.Mohanty & R.N.Ghosh. *Modelling of transformation kinetics in HSLA 100 steel during continuous cooling*. Scandinavian journal of metallurgy, pages 8-13, 2001.

[23]: S.Denis, D.Farias & A.Simon. *Mathematical model coupling phase transformations and temperature evolutions in steels.* ISIJ International, Vol.32, No.3, pages 316-325, 1992.

[24]: R.Wendelstorf, K-H.Spitzer, J.Wendelstorf. *Effect of oxide layers on spray water cooling heat transfer at high surface temperatures*. International Journal of Heat and Mass Transfer 51, pages 4892-4901, 2008.

[25]: J.B.Wiskel, H.Deng, C.Jefferies & H.Henein. *Infrared thermography of TMCP microalloyed steel skelp at upcoiler and its application in quantifying laminar jet/skelp interaction.* Ironmaking and steelmaking, Vol.38, No.1, pages 35-44, 2011.

[26]: M.Kang, M-X.Zhang, F.Liu & M.Zhu. *Kinetics and Morphology of Isothermal Transformations at Intermediate Temperature in 15CrMnMoV Steel*. Materials Transactions, Vol.50, No.1, pages 123-129, 2009.

[27]: B.Efron, R.J.Tibshirani. *An introduction to the Bootstrap*. Chapman & Hall/CRC, 1993.

[28]: N.Khodaie, D.G.Ivey & H.Henein. *Extending an empirical and a fundamental bainite start model to a continuously cooled microalloyed steel*. Materials Science & Engineering A, Vol.650, pages 510-522, 2016.

[29]: F.S.LePera. *Improved Etching Technique for the Determination of Percent Martensite in High-Strength Dual-Phase Steels*. Metallography 12, pages 263-268, 1979.

[30]: H.Yang. *Continuous cooling transformation behavior of X70 pipeline steel*. Advanced Materials Research, Vols.690-693, pages 2205-2209, 2013.

[31]: R.Pandi. Modelling of austenite-to-ferrite transformation behavior in low carbon steels during run-out table cooling. PhD thesis in University of British Columbia, 1998.

[32]: S.Vervynckt, K.Verbeken, B.Lopez & J.J.Jonas. *Modern HSLA steels and role of nonrecrystallisation temperature*. International Materials Reviews, 57:4, pages 187-207, 2012.

[33]: M.Militzer, E.B.Hawbolt & T.R.Meadowcroft. *Microstructural Model for Hot Strip Rolling of High Strength Low-Alloy Steels.* Metallurgical and materials transactions A, Vol.31A, pages 1247-1259, 2000.

[34]: N.Khodaie. (Private communications 2015)

[35]: B.Bineshmarvasti. *Optimization of steel microstructure during laminar cooling*. MSc thesis at University of Alberta, 2011.

[36]: M.I.Onsoien, M.M'Hamdi & A.Mo. *A CCT Diagram for an Offshore Pipeline Steel of X70 Type*. Supplement to the Welding Journal, Vol. 88, pages 1-6, 2009.

# Appendix

## Appendix A: Heat transfer equations

The objective of the thermal model is to predict the temperature profile of the steel skelp. The theory behind the heat transfer is well established and has been used in several studies [6-7-8]. The 3D heat equation is based on the conservation of energy and expressed as follow:

$$\begin{matrix} Rate\ of\ heat \\ accumulated \end{matrix} = \begin{matrix} Rate\ of\ heat \\ accross\ the\ boudaries \end{matrix} + \begin{matrix} Rate\ of\ heat \\ generated \end{matrix} \tag{29}$$

The rate of heat accumulated correspond to the amount of heat created or lost during the transformation. A 3D region V with the boundary S is considered. T(**X**,t) is the temperature of the material at the position **X**=(x,y,z) (in Cartesian coordinates) and the time t. The properties of the material are ρ the density, c the specific heat and λ the thermal conductivity. The rate of heat accumulated can then be written:

$$\begin{matrix} Rate\ of\ heat \\ accumulated \end{matrix} = \frac{d}{dt}\iiint_V \rho c T dV \tag{30}$$

The rate of heat across the boundaries correspond to the rate of heat that comes in the system minus the rate of heat that comes out. The rate of heat is obtained combining the divergence theorem of Gauss with Fourier's law [9]:

$$\begin{matrix} Rate\ of\ heat \\ accross\ the\ boudaries \end{matrix} = \iiint_V \lambda \nabla^2 \mathrm{T} \mathrm{dV} \tag{31}$$

The rate of heat generated is due to the phase transformations that occurs in the material with the temperature variations. It is characterized by the latent heat of transformation $Q_V$. The latent heat is the amount of energy absorbed or released during a phase transformation of a material.

$$\begin{matrix} Rate\ of\ heat \\ generated \end{matrix} = \iiint_V Q_V dV \tag{32}$$

Combining Equations 2, 3 and 4, and considering that the system V is independent of time, the heat transfer equation becomes:

$$\iiint_V \left(\lambda \nabla^2 \mathrm{T} + Q_V - c\rho \frac{\partial T}{\partial t}\right) dV = 0 \tag{33}$$

We are using the Cartesian coordinates so the Laplace operator can be written as:

$$\nabla^2 \mathrm{T} = \frac{\partial^2 T}{\partial x^2} + \frac{\partial^2 T}{\partial y^2} + \frac{\partial^2 T}{\partial z^2} \tag{34}$$

Since the system V is arbitrary then the integrand has to be equal to zero for every position. So the 3D heat transfer equation for the temperature T(x,y,z,t) is:

$$\lambda\left(\frac{\partial^2 T}{\partial x^2} + \frac{\partial^2 T}{\partial y^2} + \frac{\partial^2 T}{\partial z^2}\right) + \mathrm{Q}_V - c\rho\frac{\partial T}{\partial t} = 0 \tag{35}$$

**Boundary conditions:**

To solve the heat transfer equation, boundary conditions are needed. As mentioned previously, three different phenomena can occur at the surface of the skelp [5]. Whenever there is water at the surface of the strip, the heat exchange between the material and the surrounding can be summed up with a convection equation [5]. However, the liquid water and the vapor have to be differentiate because different heat transfer coefficients are involved: $h_{water}$ and $h_{vapor}$. The heat fluxes through the surface are called: $\phi_{water}$ and $\phi_{vapor}$, and characterize the exchange of heat between the surface at the temperature T and the surrounding at the temperature $T_{water}$ and $T_{vapor}$ respectively:

$$\begin{cases} \phi_{water} = -\lambda\nabla\mathrm{T} = h_{water}(T - T_{water}) \\ \phi_{vapor} = -\lambda\nabla\mathrm{T} = h_{vapor}(T - T_{vapor}) \end{cases} \tag{36}$$

In the ROT, the role of the side sprays is to remove the water from the surface of the steel. Cooling is mainly due to two different mechanisms: the convection between the material and the surrounding and the radiation of the material. In Equation 9, the radiative part is characterized by the Stefan-Boltzman constant σ and the emissivity factor ε:

$$\phi_{air} = -\lambda\nabla\mathrm{T} = \sigma\varepsilon\left(T^4 - {T_\infty}^4\right) \tag{37}$$

# Appendix B: Description of the run-out table

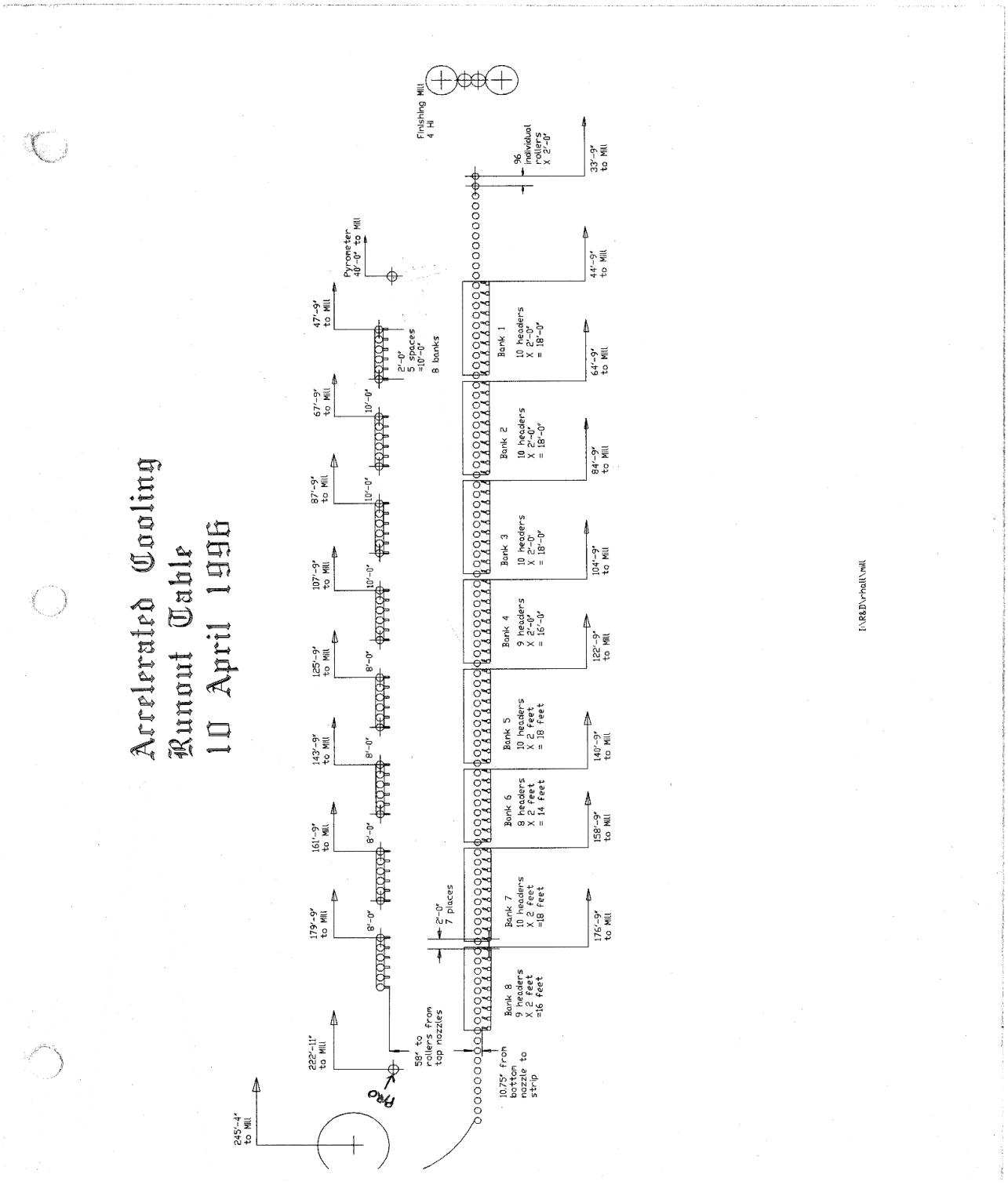


*Figure B- 1: Layout of the run-out table*

ROT description:

The ROT comprises eight water banks on each side of the skelp. For the scope of this study and to match with the industrial setup, only the first five out of the eight are used (Figure 3-1). The top part the first four water banks are placed 3.05m (10 ft) away from each other and the last one is positioned 2.44m after the fourth one. Each water bank consists of the series of six lines of 40 evenly spaced nozzles (Figure 3-2) that deliver a laminar flow stream of water onto the surface of the steel strip. The distance between each line is 0.61m (2ft). All the nozzles are assumed to be identical and pour the same water stream onto the surface of the skelp. Each nozzle has a diameter of 10mm and discharges water at a flow rate of approximately 1.21 $m^3$/min (320gpm) at a temperature of 21°C. All the water banks are immediately followed by side sprays to remove the remaining water on the top surface of the skelp. The bottom part the surface is cooled down by a series of 50 water sprays (10 headers per water bank) evenly spaced all along the length of the strip. The distance between every spray is 0.61m (2ft).

## Appendix C: Steel compositions

*Table C- 1: Composition of the steel used in the ROT*

| **Identification: X70-17.3mm (Run-out table)** | | | | | | | |
|---|---|---|---|---|---|---|---|
| **C** | **Mn** | **S** | **P** | **Si** | **Cu** | **Ni** | **Cr** |
| 0.043 | 1.67 | 0.001 | 0.012 | 0.26 | 0.28 | 0.08 | 0.09 |
| **V** | **Nb** | **Mo** | **Sn** | **Al** | **N** | **Ti** | **Ca** |
| 0.003 | 0.067 | 0.192 | 0.013 | 0.046 | 0.009 | 0.016 | 0.003 |

*Table C- 2: Composition of the X70 steel used to obtain the dilation curves*

| **Identification: Evraz X70-A** | | | | | | | |
|---|---|---|---|---|---|---|---|
| **C** | **Mn** | **S** | **P** | **Si** | **Cu** | **Ni** | **Cr** |
| 0.049 | 1.63 | 0.001 | 0.012 | 0.17 | 0.20 | 0.09 | 0.1 |
| **V** | **Nb** | **Mo** | **Sn** | **Al** | **N** | **Ti** | **Ca** |
| 0.001 | 0.075 | 0.244 | 0.010 | 0.038 | 0.010 | 0.017 | 0.004 |

## Appendix D: Thermal history of the Gleeble X70-A samples

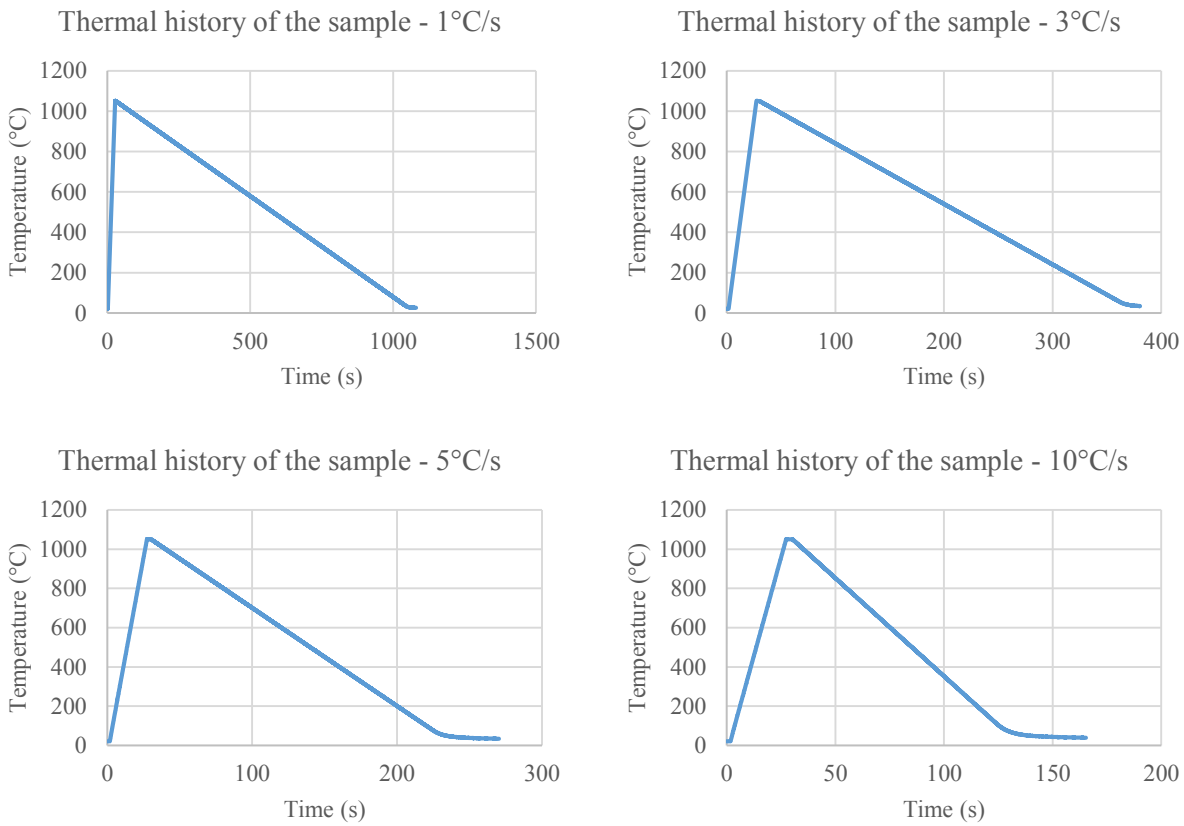


*Figure D- 1: Thermal history of the dilation samples for different cooling rates*

## Appendix E: Modification of the Avrami equation

$f^{-1}$ is plotted with $ln\left(\frac{T-T_0}{CR}\right)$:

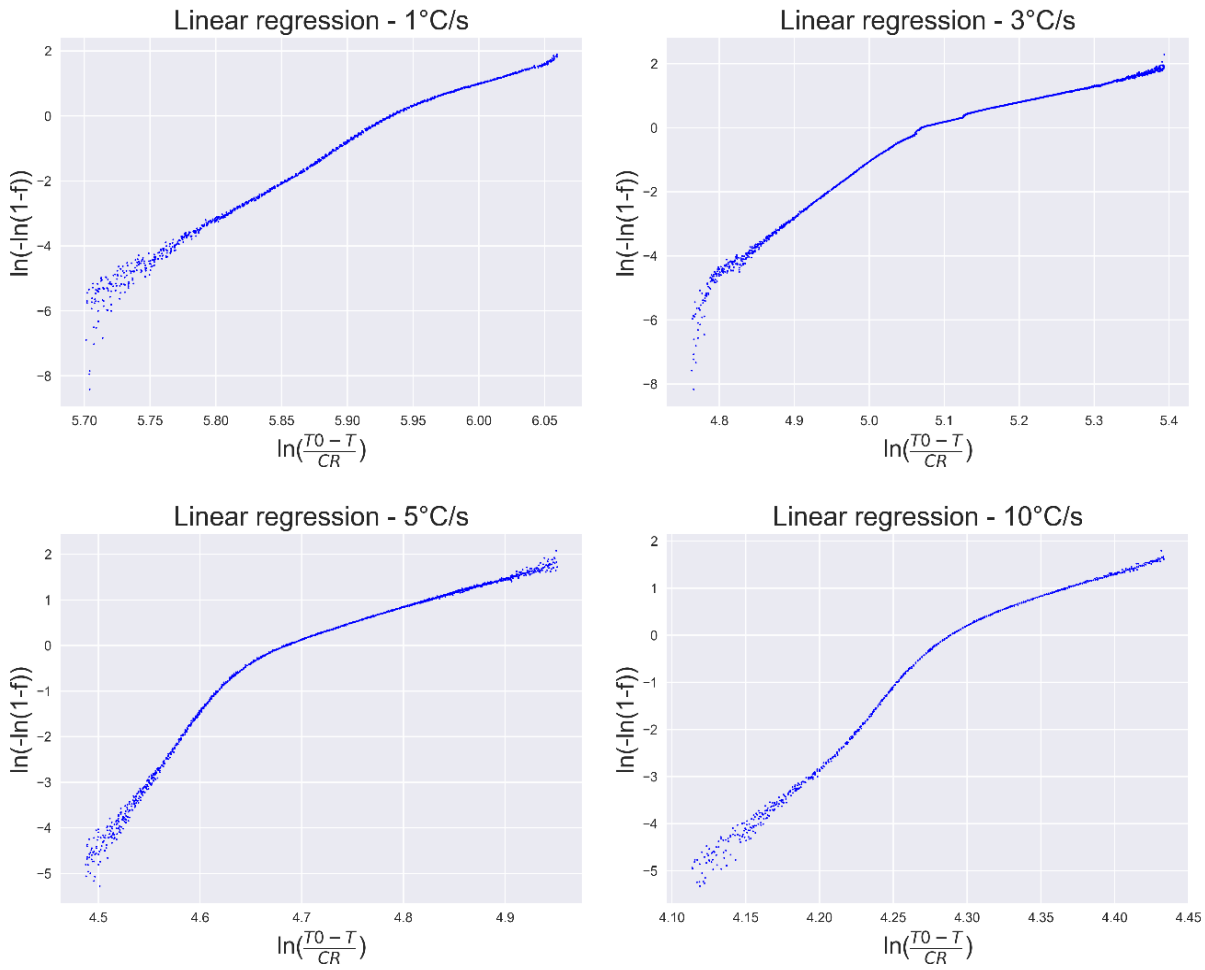


*Figure E- 1: Linear regression of the Avrami equation plotted with* $ln\left(\frac{T_0-T}{CR}\right)$ *for different cooling rates*

Now $f^{-1}$ is plotted with $\frac{1}{RT}$ :

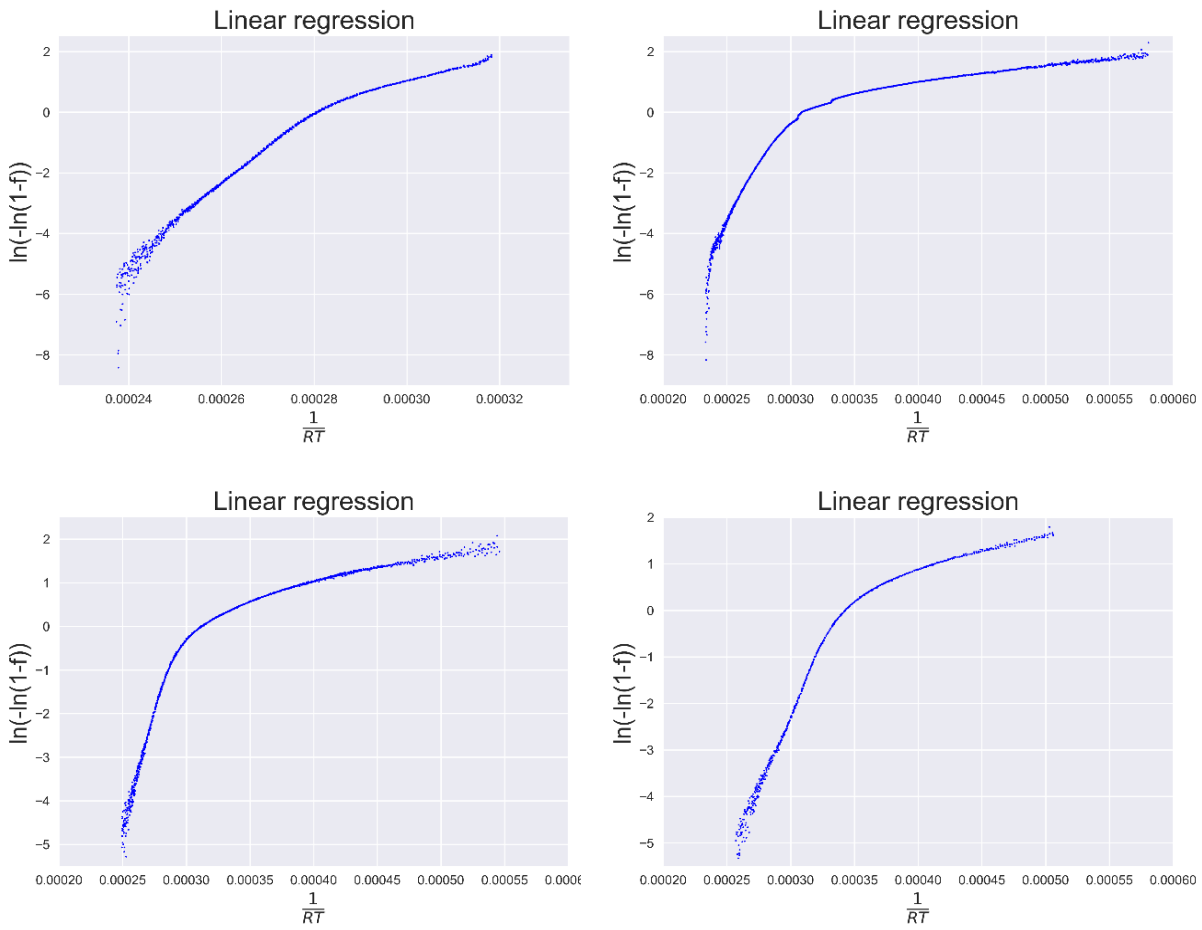


*Figure E- 2: Linear regression of the Avrami equation plotted with $\frac{1}{RT}$ for different cooling rates*

## Appendix F: Analytical solution of the Avrami parameters

We wish to optimize the following least-squares problem:

$$\min_{n,Q,\tau_0}\left\{\frac{1}{m}\sum_{i=1}^{m}L\left(y_i,\hat{y}_i(n,Q,\tau_0)\right)\right\} \tag{38}$$

Where $L(y_i,\hat{y}_i)$ is the squared loss function given by:

$$\begin{aligned}L(y_i,\hat{y}_i) &= [y_i-\hat{y}_i(n,Q,\tau_0)]^2\\ &= [y_i-n(x_i-ln(\tau_0)+Qz_i)]^2\end{aligned} \tag{39}$$

With:

$$\begin{cases}y_i = ln\left(-ln(1-f)\right)\\ x_i = ln\left(\dfrac{T_0-T_i}{CR}\right)\\ z_i = \dfrac{1}{RT_i}\end{cases} \tag{40}$$

Taking the derivative with respect to all parameters, we obtain:

$$\begin{cases}\dfrac{\partial L}{\partial n} = -\dfrac{2}{m}\displaystyle\sum_{i=1}^{m}[y_i-n(x_i-ln(\tau_0)+Qz_i)](x_i-ln(\tau_0)+Qz_i)\\ \dfrac{\partial L}{\partial Q} = -\dfrac{2n}{m}\displaystyle\sum_{i=1}^{m}[y_i-n(x_i-ln(\tau_0)+Qz_i)](z_i)\\ \dfrac{\partial L}{\partial \tau_0} = \dfrac{2n}{m\tau_0}\displaystyle\sum_{i=1}^{m}[y_i-n(x_i-ln(\tau_0)+Qz_i)]\end{cases} \tag{41}$$

Simplifying we obtain:

$$\begin{cases}\dfrac{\partial L}{\partial n} = -2\left[\overline{yx}-ln(\tau_0)\bar{y}+Q\overline{yz}-n\left(\overline{x^2}+ln(\tau_0)^2+Q^2\overline{z^2}-2ln(\tau_0)\bar{x}+2Q\overline{xz}-2Qln(\tau_0)\bar{z}\right)\right]\\ \dfrac{\partial L}{\partial Q} = -2n\left[\overline{yz}-n\left(\overline{xz}-ln(\tau_0)\bar{z}+Q\overline{z^2}\right)\right]\\ \dfrac{\partial L}{\partial \tau_0} = \dfrac{2n}{\tau_0}[\bar{y}-n(\bar{x}-ln(\tau_0)+Q\bar{z})]\end{cases} \tag{42}$$

With $\bar{x}$ the mean value of x (same with y, z and the products):

$$\bar{x} = \frac{1}{m}\sum_{i=1}^{m}x_i \tag{43}$$

We want to minimize the squared loss function, so we need:

$$\begin{cases} \dfrac{\partial L}{\partial n} = 0 \\ \dfrac{\partial L}{\partial Q} = 0 \\ \dfrac{\partial L}{\partial \tau_0} = 0 \end{cases} \tag{44}$$

Solving for $\tau_0$ in the last equation, we have:

$$\tau_0 = exp\left(Q\bar{z} + \bar{x} - \frac{\bar{y}}{n}\right) \tag{45}$$

Subbing this result into the first equation, we obtain:

$$\begin{aligned} 0 = \overline{yx} - \left(Q\bar{z} + \bar{x} - \frac{\bar{y}}{n}\right)\bar{y} + Q\overline{yz} \\ - n\left(\overline{x^2} + \left(Q\bar{z} + \bar{x} - \frac{\bar{y}}{n}\right)^2 + Q^2\overline{z^2} - 2\left(Q\bar{z} + \bar{x} - \frac{\bar{y}}{n}\right)\bar{x} + 2Q\overline{xz}\right. \\ \left. - 2Q\left(Q\bar{z} + \bar{x} - \frac{\bar{y}}{n}\right)\bar{z}\right) \end{aligned} \tag{46}$$

Then:

$$\begin{aligned} 0 = (\overline{yx} - \bar{x}\bar{y}) + Q(\overline{yz} - \bar{y}\bar{z}) - \frac{\bar{y}^2}{n} \\ - n\left(\overline{x^2} + \left(Q\bar{z} + \bar{x} - \frac{\bar{y}}{n}\right)^2 + Q^2\overline{z^2} - 2l\left(Q\bar{z} + \bar{x} - \frac{\bar{y}}{n}\right)\bar{x} + 2Q\overline{xz}\right. \\ \left. - 2Q\left(Q\bar{z} + \bar{x} - \frac{\bar{y}}{n}\right)\bar{z}\right) \end{aligned} \tag{47}$$

After much simplification, we obtain:

$$0 = cov(y,x) + Qcov(y,z) - n[var(x) + Q^2 var(z) + 2Qcov(x,z)] \tag{48}$$

Where:

$$\begin{aligned} cov(x,y) &= \frac{1}{m}\sum_{i=1}^{m}(x_i - \bar{x})(y_i - \bar{y}) = \overline{xy} - \bar{x}\bar{y} \\ var(x) &= cov(x,x) = \overline{x^2} - \bar{x}^2 \end{aligned} \tag{49}$$

Solving for n in (10):

$$n = \frac{cov(y,x) + Qcov(y,z)}{var(x) + Q^2 var(z) + 2Qcov(x,z)} \tag{50}$$

Then:

$$n = \frac{cov(y, Qz + x)}{var(Qz + x)} \tag{51}$$

Subbing the equation for $\tau_0$ result in the gradient equation for Q, we obtain:

$$\begin{aligned} 0 &= \overline{yz} - n\left(\overline{xz} - ln(\tau_0)\bar{z} + Q\overline{z^2}\right) \\ &= \overline{yz} - \bar{y}\bar{z} - n\left(\overline{xz} - \bar{x}\bar{z} + Q\left(\overline{z^2} - \bar{z}^2\right)\right) \\ &= cov(y, z) - n\left(cov(x, z) + Qvar(z)\right) \end{aligned} \tag{52}$$

Then subbing with the equation for n result we obtain:

$$\begin{aligned} 0 &= cov(y, z) - \frac{cov(y, x) + Qcov(y, z)}{var(x) + Q^2 var(z) + 2Qcov(x, z)}\left(cov(x, z) + Qvar(z)\right) \\ 0 &= cov(y, z) - \frac{cov(y, x)cov(x, z) + Qcov(y, x)var(z) + Qcov(y, z)cov(x, z) + Q^2 cov(y, z)var(z)}{var(x) + Q^2 var(z) + 2Qcov(x, z)} \end{aligned} \tag{53}$$

Cross-multiplying, we obtain:

$$\begin{aligned} 0 = {} & cov(y, z)var(z)Q^2 + 2ov(y, z)cov(x, z)Q + cov(y, z)var(x) \\ & - \left(cov(y, x)cov(x, z) + Qcov(y, x)var(z) + Qcov(y, z)cov(x, z)\right. \\ & \left. + Q^2 cov(y, z)var(z)\right) \\ 0 = {} & \left(cov(y, z) - cov(y, x)\right)var(z)Q^2 + (cov(x, z)cov(y, z) - cov(y, x)var(z))Q \\ & + (cov(y, z)var(x) - cov(y, x)cov(x, z)) \end{aligned} \tag{54}$$

Q must verify this second-degree polynomial.

So, to sum up we have:

$$\begin{cases} \tau_0 = exp\left(Q\bar{z} + \bar{x} - \dfrac{\bar{y}}{n}\right) \\ n = \dfrac{cov(y, Qz + x)}{var(Qz + x)} \\ \left(cov(y, z) - cov(y, x)\right)var(z)Q^2 + \left(cov(x, z)cov(y, z) - cov(y, x)var(z)\right)Q + \\ (cov(y, z)var(x) - cov(y, x)cov(x, z)) = 0 \end{cases} \tag{55}$$

## Appendix G: Comparison between the Avrami parameters for the three steels studied

The Avrami parameters have been found for the X70-A, X70-B and X80 steels, studied in this thesis. The modification of the fraction transformed curves obtained with the lever rule has shown for the three steels two separate branches. Thus, the Avrami parameters n and $\tau_0$ have been calculated for the two branches of each steel. The comparison of these parameters is presented as follow:

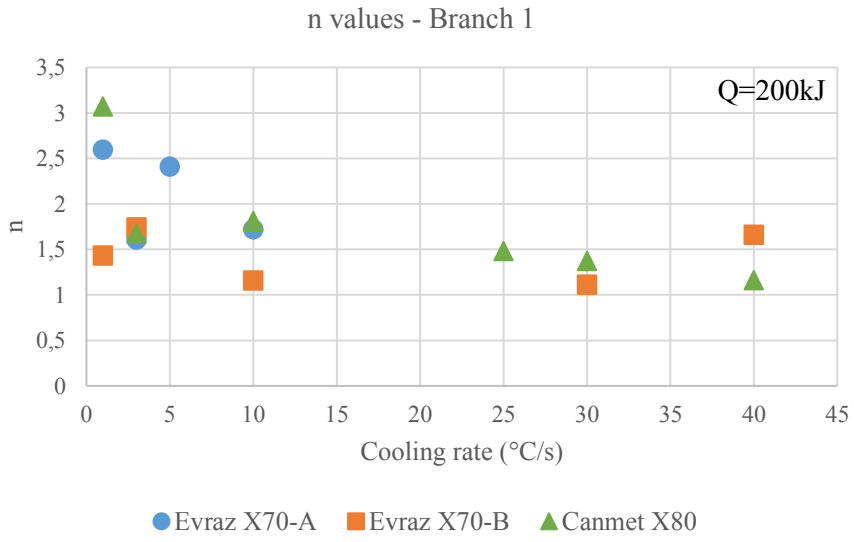


*Figure G- 1: Parameter n found for branch 1 of the modified curve for the three steels.*

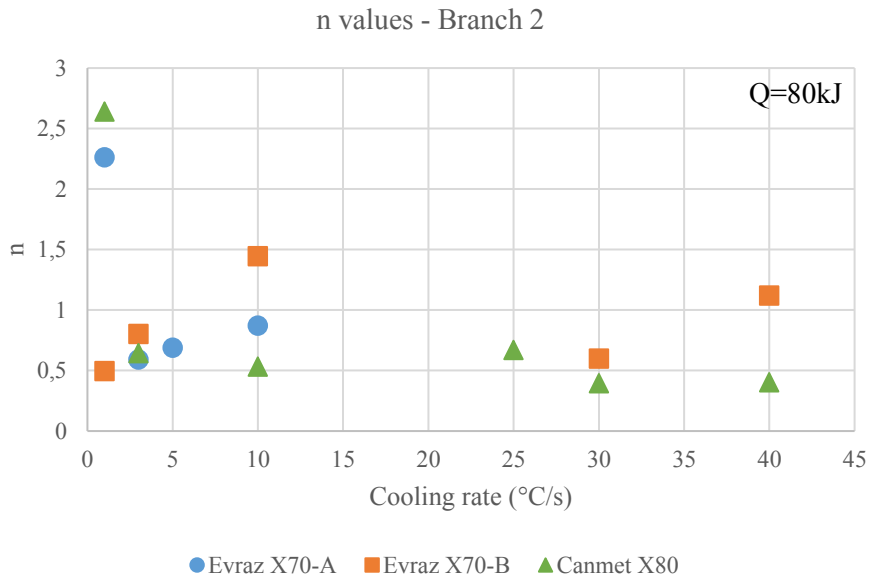


*Figure G- 2: Parameter n found for branch 2 of the modified curve for the three steels.*

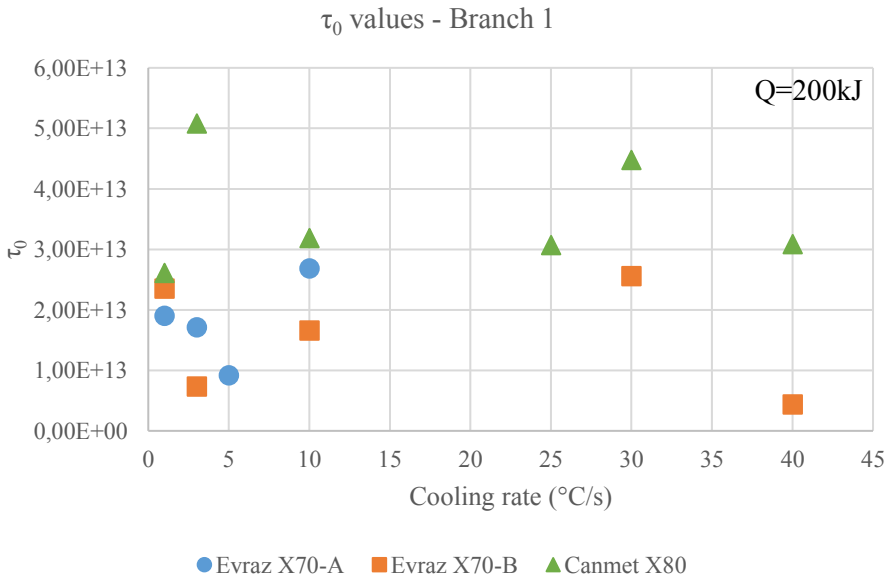


*Figure G- 3: Parameter $\tau_0$ found for branch 1 of the modified curve for the three steels.*

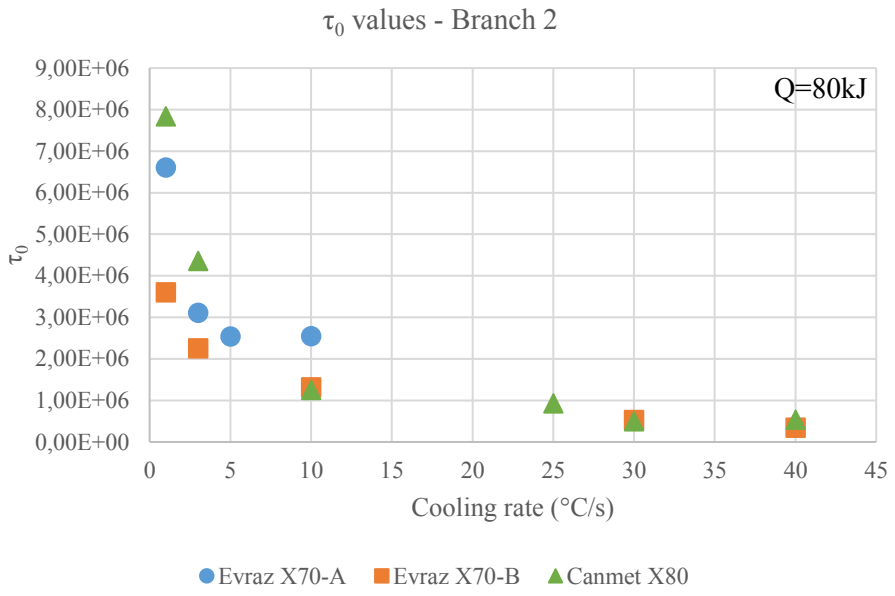


*Figure G- 4: Parameter τ0 found for branch 2 of the modified curve for the three steels.*

## Appendix H: Derivation of the modified curves

The slope of the modified fraction transformed curve varies a lot over the range of temperature, as shown in Figure 1. Even if the modified curve has been smoothed, the large number of data points and its scattered aspect result in this behavior of the experimental slope. Looking at Figure 1, the experimental curve drifts from one branch to the other. Thus, the only relevant temperature range in Figure 1, is where the experimental slope varies from the slope of branch 1 to the slope of branch 2, as presented in Figure 1, because it is where the two phases are formed simultaneously. Thus, outside the region where the two structures are formed simultaneously the experimental slope will be considered equal to either the slope of branch 1 or branch 2, as shown in Figure 2.

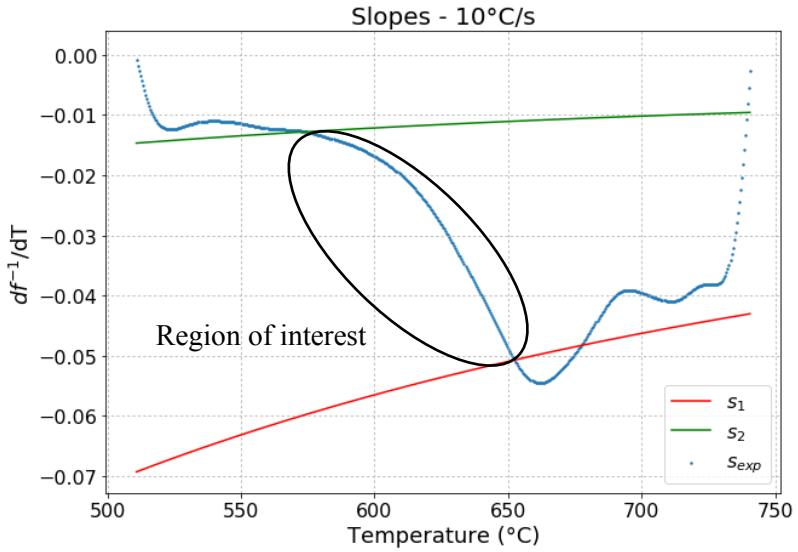


*Figure H- 1: Slopes of the modified curve and the two branches for 10°C/s.*

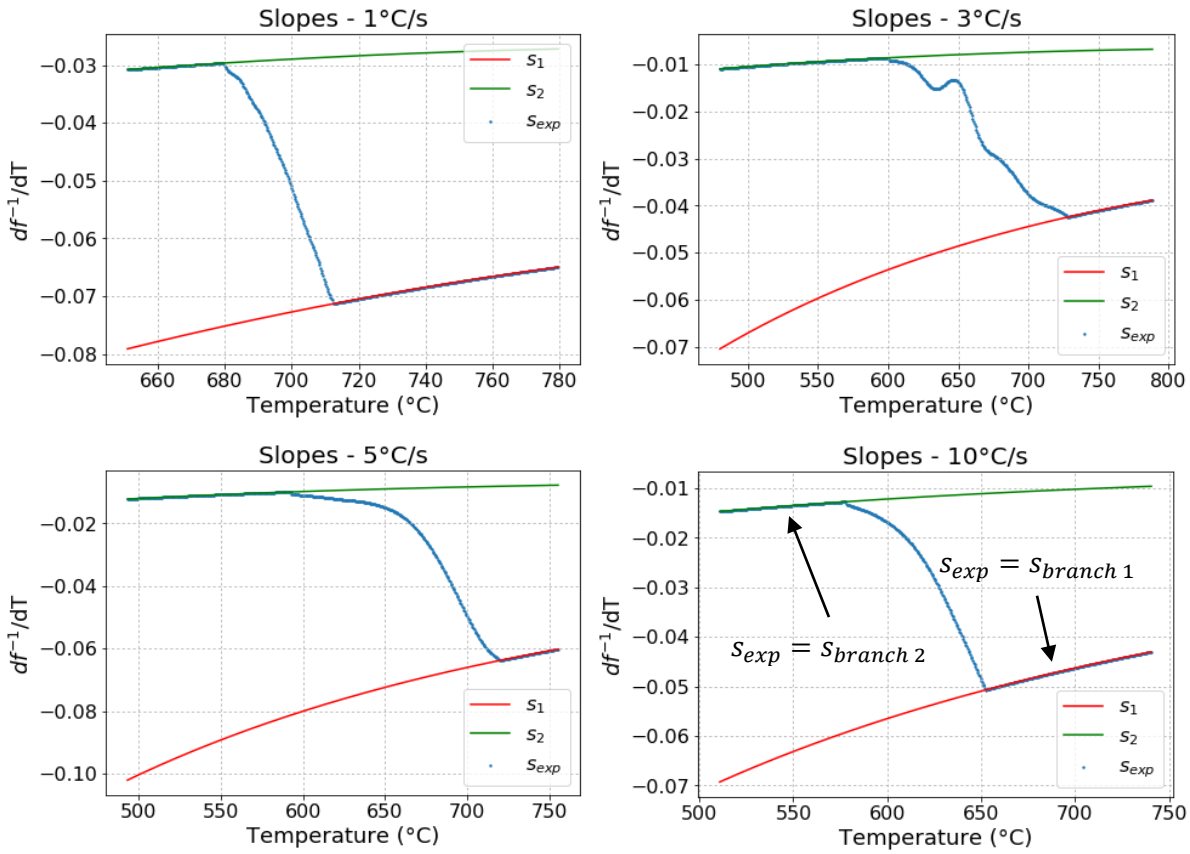


*Figure H- 2: Modified slopes of the modified curves for different cooling rates.*

## Appendix I: Intermediary results of the metallurgical model for the X70-B and X80 steels

The values of the slopes and the parameter α are presented in Figures 1 and 2 for the X70-B steel and in Figure 3 and 4 for the X80 steel:

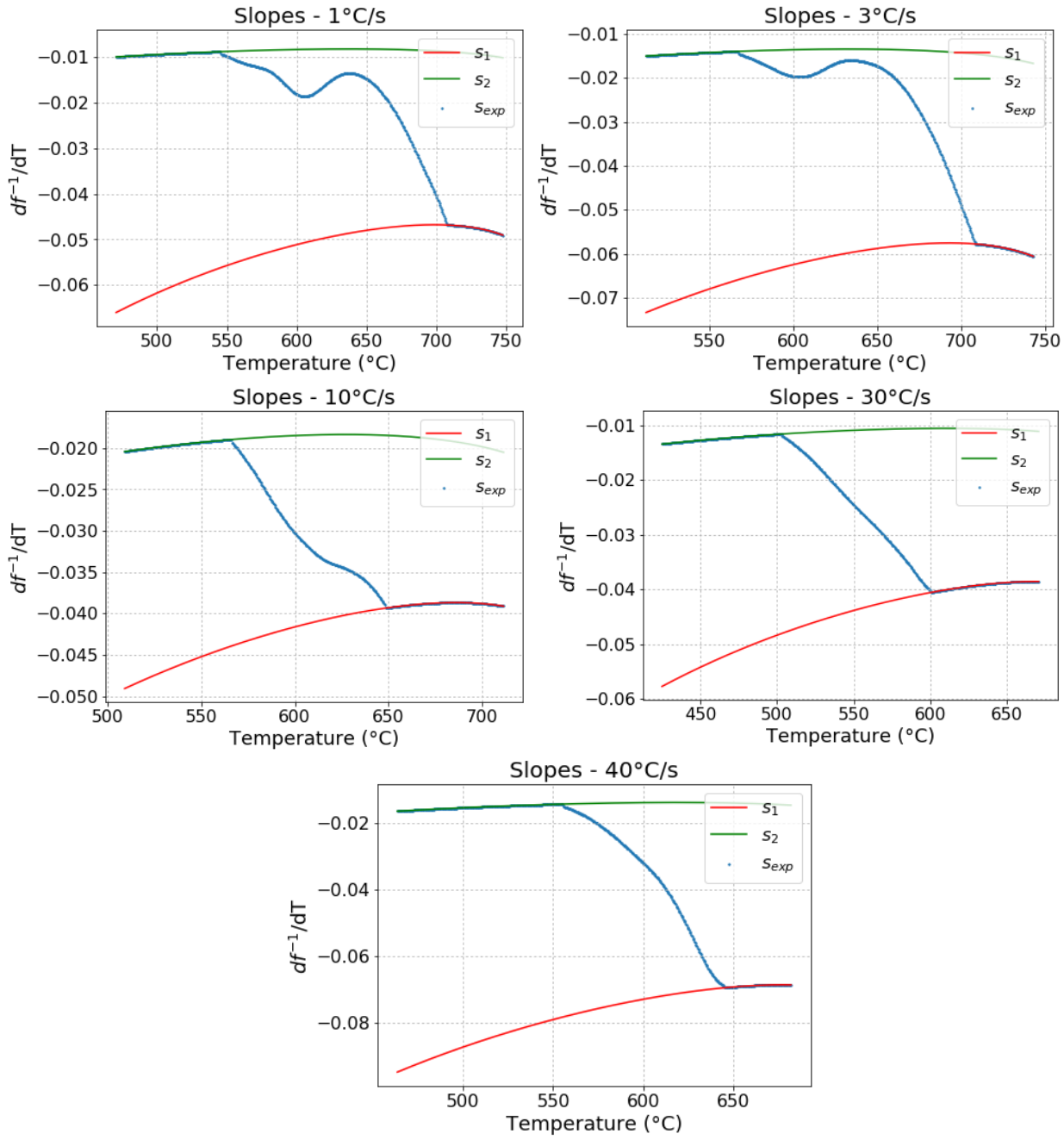


*Figure I- 1: Slopes of the modified curves for the X70-B steel.*

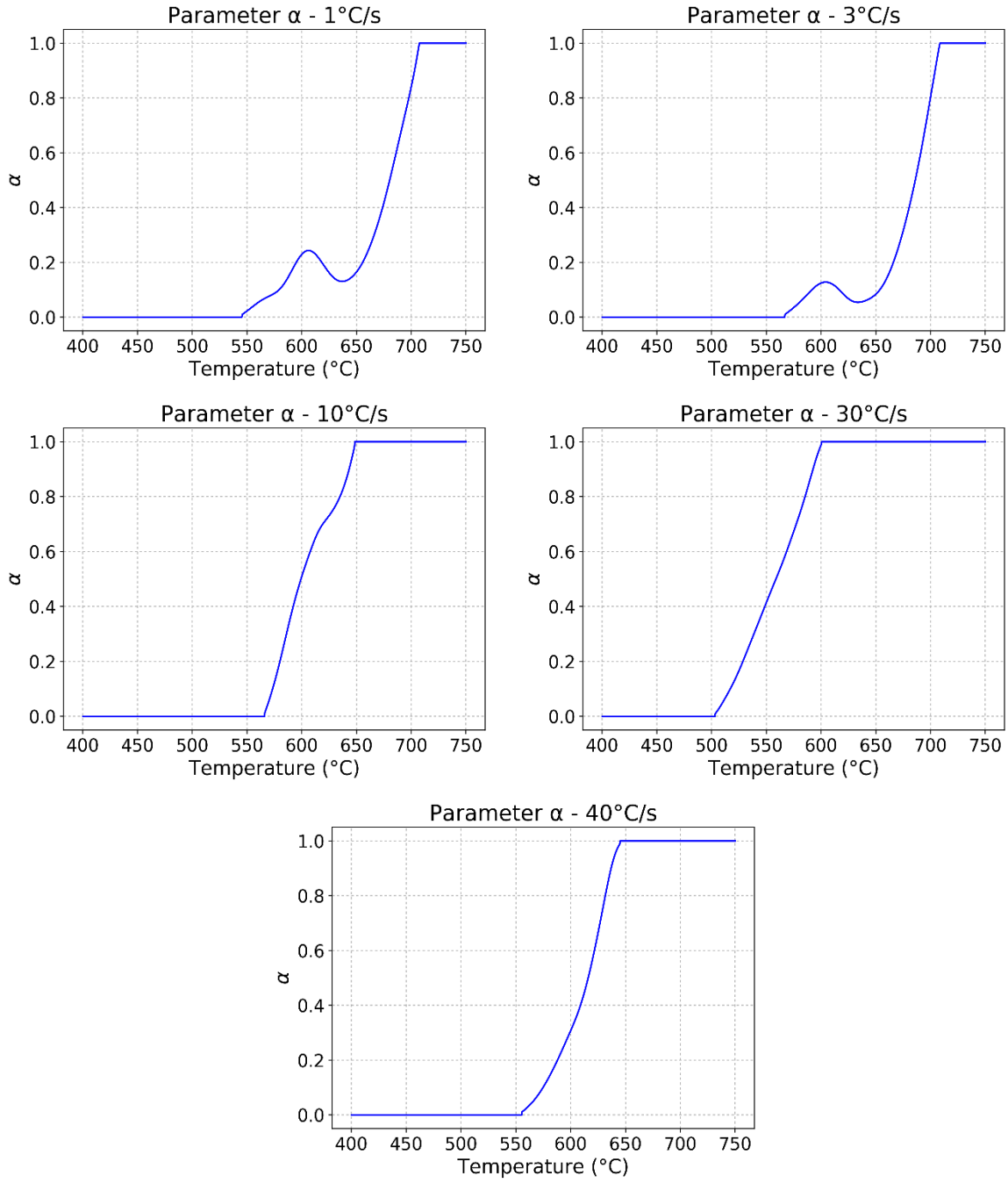


*Figure I- 2: Evolution of the parameter α with temperature for the X70-B steel.*

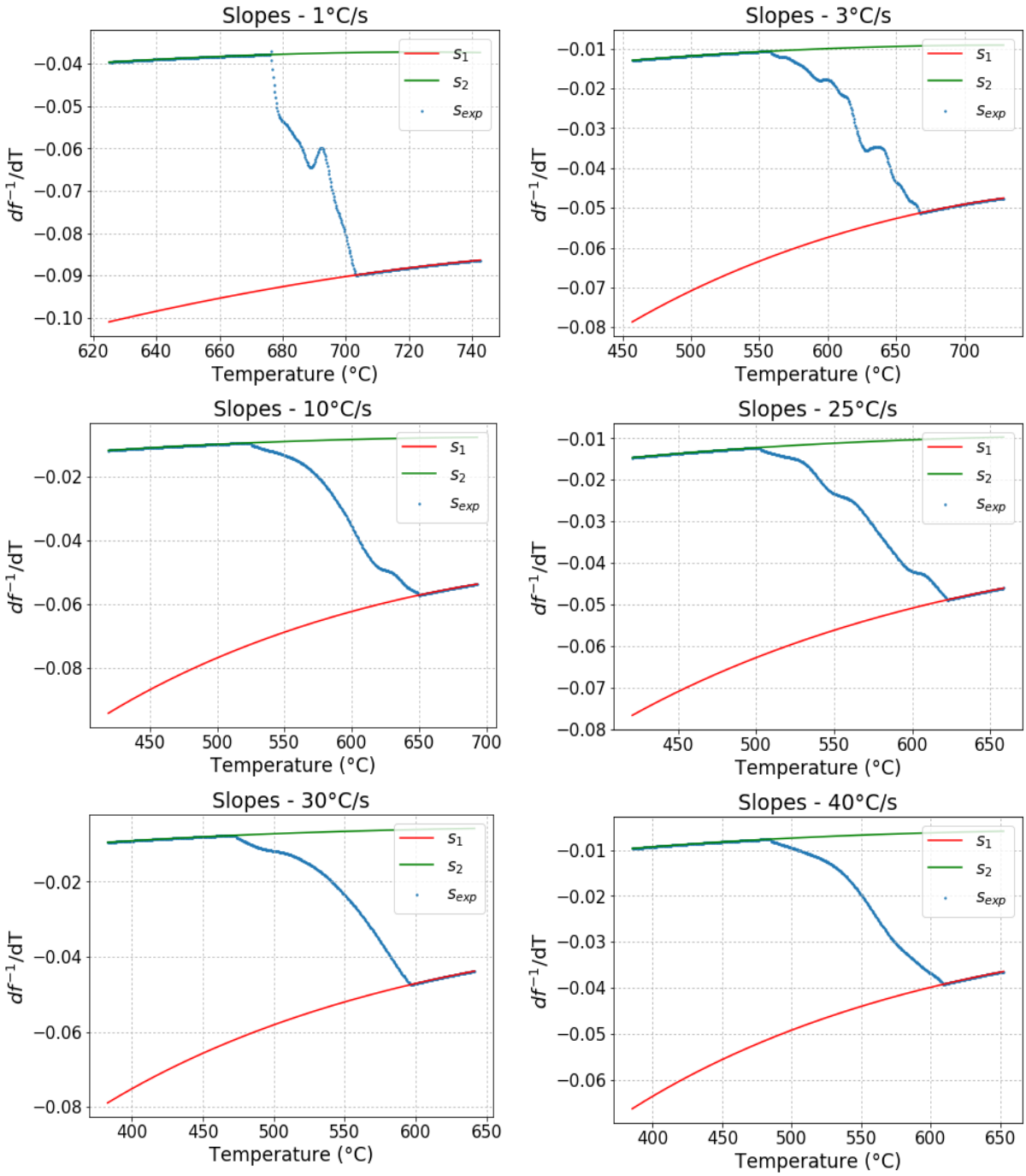


*Figure I- 3: Slopes of the modified curves for the X80 steel.*

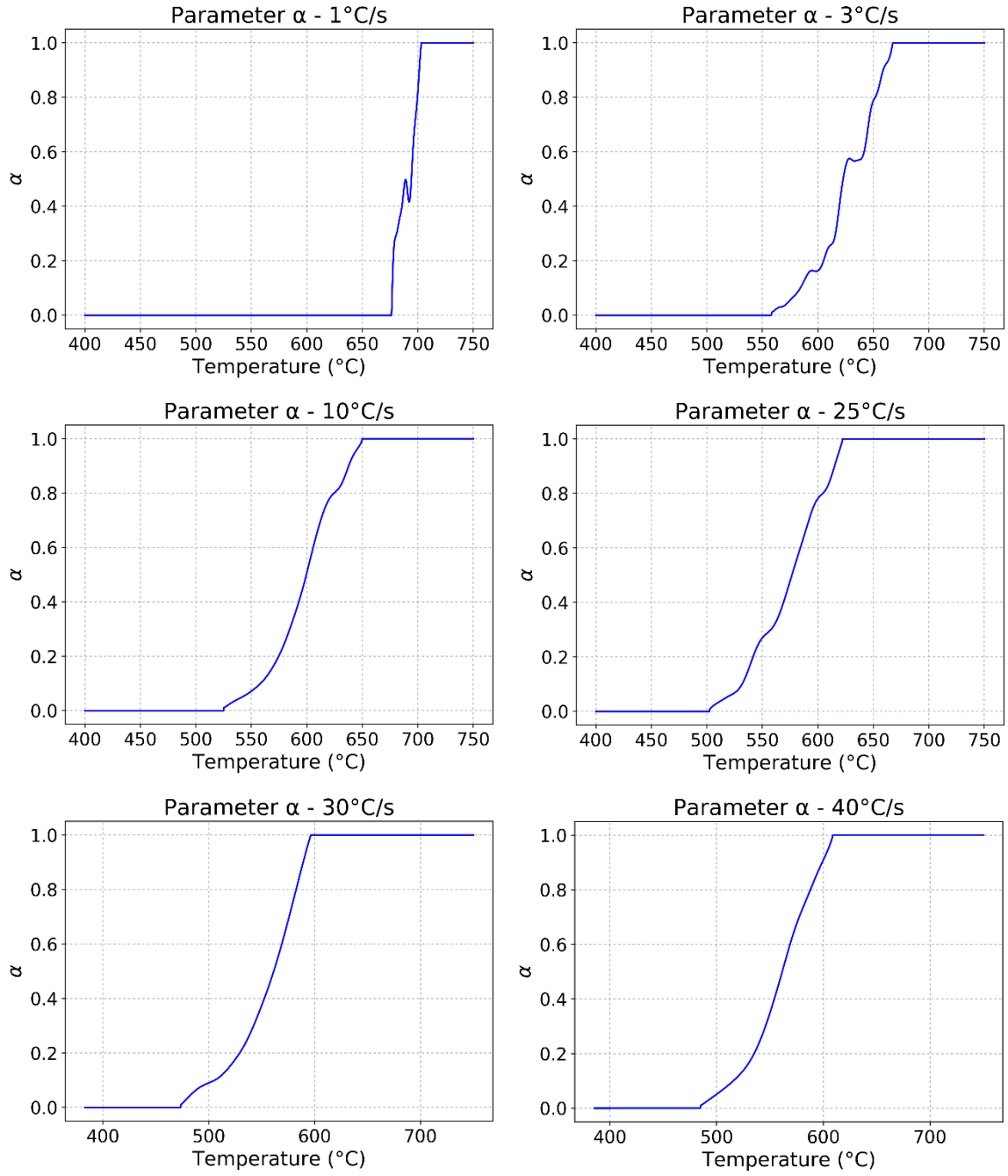


*Figure I- 4: Evolution of the parameter α with temperature for the X80 steel.*